

# Oxidation of Palladium Surfaces

Submitted by  
Dipl.-Phys.  
Mira Todorova

in the Faculty II-Mathematics and Natural Sciences  
at the Technical University Berlin  
to obtain the degree

DOCTOR RERUM NATURALIUM

Thesis accepted

Committee:

Head of the Committee: Prof. Dr. Wolfgang Richter

Referee: Prof. Dr. Ekehard Schöll

Referee: Prof. Dr. Matthias Scheffler

Exam date: 15 March 2004

Berlin 2004

D 83



# Oxidation von Palladium-Oberflächen

Vorgelegt von  
Diplom-Physikerin  
Mira Todorova

Von der Fakultät II-Mathematik und Naturwissenschaften  
der Technischen Universität Berlin  
zur Erlangung des akademischen Grades  
DOCTOR RERUM NATURALIUM  
genehmigte Dissertation

Promotionsausschuss:

Vorsitzender: Prof. Dr. Wolfgang Richter

Berichter: Prof. Dr. Eckehard Schöll

Berichter: Prof. Dr. Matthias Scheffler

Tag der wissenschaftlichen Aussprache: 15. März 2004

Berlin 2004

D 83





# Preface

The interactions of oxygen atoms with transition metal surfaces play an important role for technologically relevant processes such as corrosion or heterogeneous catalysis. Gaining a deeper insight into the behaviour of oxygen on these metal surfaces appears therefore desirable.

In the present work the oxygen interactions with the (111) and (100) surfaces of palladium are investigated using density-functional theory. The concept of *ab-initio atomistic thermodynamics* is employed to determine the stability of various O-phases subject to the chemical potential of oxygen. Furthermore, the behaviour of O-atoms on Pd is compared to experiments and existing theoretical findings for Ru, Rh and Ag, the neighbouring 4*d* transition metals in the periodic table.

Regarding Pd(111) it was found, that sub-surface oxygen incorporation is initially always less favourable than on-surface chemisorption due to the additional lattice deformation cost in the former case. Penetration into the crystal begins after a critical O-atom coverage,  $\theta_c$ , lying in the range between 0.50 ML and 0.75 ML, is reached. A comparison with similar data for Ru, Rh and Ag shows that  $\theta_c$  decreases progressively from Ru to Ag. It is, furthermore, quite similar to the critical coverage at which oxide phases become thermodynamically more stable than the chemisorbed adlayers. This points towards the incorporation of sub-surface oxygen being a limiting step for the oxide formation on transition metal surfaces.

On the Pd(100) surface the  $(\sqrt{5} \times \sqrt{5})R27^\circ$  surface oxide was identified to be a strained, but commensurable thin PdO(101) layer, which is largely stabilised through a strong coupling to the underlying substrate. A comparison of calculated and measured core-level shifts (including final-state effects) shows that this assignment is compatible with high-resolution core-level spectroscopy data. A STM-simulation program was incorporated into the program-package used for the calculations, thus making the comparison to scanning tunneling microscopy data possible as well.

An analysis of the stability of different oxygen phases on Pd(111) and Pd(100) with regard to the surrounding oxygen gas phase shows, that the surface oxides on these surfaces represent the most stable phases over a wide range of environmental conditions far exceeding the stability range of bulk PdO. Comparison with

corresponding experimental data in the pressure range between  $10^{-9}$  and 1 bar and temperatures up to 1000 K discerns kinetic hindrances to the formation of both the surface and the bulk oxide even at temperatures as high as 600 K and atmospheric pressures.

# Zusammenfassung

Die Wechselwirkung von Sauerstoffatomen mit Übergangsmetalloberflächen spielt eine wichtige Rolle in technologisch relevanten Prozessen wie Korrosion oder Katalyse. Es erscheint daher wünschenswert, einen tieferen Einblick in das Sauerstoffverhalten auf Übergangsmetalloberflächen zu gewinnen.

In der vorliegenden Arbeit werden mittels Dichtefunktional-Theorie Sauerstoff-Wechselwirkungen mit den (111) und (100) Oberflächen von Palladium untersucht. Mit Hilfe der *ab-initio, atomistic thermodynamics* Methode wird des Weiteren die Stabilität der verschiedenen O-Phasen in Abhängigkeit des chemischen Potentials von Sauerstoff bestimmt. Das Verhalten von O auf Pd wird mit Experimenten und vorhandenen theoretischen Ergebnissen für Ru, Rh und Ag, den benachbarten *4d* Übergangsmetallen im Periodensystem, verglichen.

Bezüglich Pd(111) wurde gefunden, dass die Besetzung von Plätzen unterhalb der Oberfläche stets mit einer starken Verzerrung des Metallgitters verbunden ist, wodurch Sauerstoffeinbau anfangs weniger günstig als die Chemisorption auf der Oberfläche ist. Das Eindringen in den Kristall beginnt erst ab einer kritischen O Bedeckung,  $\theta_c$ , welche im Bereich zwischen 0.50 ML und 0.75 ML liegt. Ein Vergleich mit ähnlichen Daten für Ru, Rh und Ag zeigt, dass  $\theta_c$  von Ru bis Ag stetig kleiner wird und zudem sehr ähnlich ist zu der kritischen Bedeckung, ab der bereits die Oxidphasen thermodynamisch stabiler als die chemisorbierte Adsorbatlage werden. Dies deutet darauf hin, dass das Eindringen des Sauerstoffs ein limitierender Schritt für die Oxidbildung auf Übergangsmetalloberflächen ist. Auf der Pd(100) Oberfläche wurde das  $(\sqrt{5} \times \sqrt{5})R27^\circ$  Oberflächenoxid als eine verspannte, dünne PdO(101) Schicht identifiziert, welche wesentlich durch eine starke Kopplung zu dem unterliegenden Substrat stabilisiert wird. Diese Zuordnung ist kompatibel mit Daten aus Hochaufgelöste Rumpfelektronen Spektroskopie, wie der Vergleich von berechneten mit gemessenen Rumpf-Niveau Verschiebungen zeigt. Um einen Vergleich mit entsprechenden Rastertunnelmikroskop Daten zu ermöglichen, wurde ein STM-Simulationsprogramm in das benutzte Programmpaket eingebaut.

Eine Untersuchung der Stabilität von verschiedenen Sauerstoffphasen auf Pd(111) und Pd(100) in Abhängigkeit von der umgebenden Sauerstoffgasphase zeigt, dass die Oberflächenoxide auf diesen Oberflächen über einen grösseren Bereich stabil sind als das bekannte Volumenoxid PdO. Ein Vergleich mit entsprechenden

experimentellen Daten im Druckbereich zwischen  $10^{-9}$  bis 1 bar und Temperaturen bis 1000 K identifizierte deutlich kinetische Limitierungen bei der Bildung des Oberflächen- und des Volumenoxides selbst noch bei Temperaturen bis 600 K und atmosphärischen Drücken.

# Contents

<b>1</b>	<b>Introduction</b>	<b>1</b>
<b>2</b>	<b>Theoretical approach</b>	<b>5</b>
2.1	The many-body problem . . . . .	5
2.2	Born-Oppenheimer Approximation . . . . .	7
2.3	Density-functional theory . . . . .	8
2.3.1	The Hohenberg-Kohn theorems . . . . .	8
2.3.2	Kohn-Sham equations . . . . .	10
2.3.3	Exchange-correlation energy functionals . . . . .	13
2.4	The FP-LAPW method . . . . .	14
2.4.1	The APW- and LAPW-Methods . . . . .	15
2.4.2	The FP-LAPW method . . . . .	17
2.4.3	The supercell method . . . . .	18
2.4.4	Integration over the Brillouin zone . . . . .	19
2.4.5	Forces in the FP-LAPW method . . . . .	19
2.4.6	The Program WIEN 97 . . . . .	20
<b>3</b>	<b>Properties of the bulk and clean surface</b>	<b>23</b>
3.1	Properties of the bulk . . . . .	23
3.2	Clean surface . . . . .	25
<b>4</b>	<b>Oxygen adlayers on Pd(111)</b>	<b>31</b>
4.1	Energetics . . . . .	32
4.1.0.1	Oxygen induced surface relaxations . . . . .	35
4.1.0.2	Electronic structure . . . . .	39
<b>5</b>	<b>Oxygen incorporation into the Pd(111) surface</b>	<b>45</b>
5.1	Thermodynamic model . . . . .	46
5.2	Initial oxygen incorporation . . . . .	47
5.3	The mixed $O_{\text{fcc}}/O_{\text{tetra-I}}$ structures . . . . .	51
5.4	Stability of sub-surface oxygen . . . . .	56
5.5	Bulk dissolved oxygen . . . . .	61

<b>6</b>	<b>The <math>(\sqrt{5} \times \sqrt{5})R27^\circ</math> surface oxide on the Pd(100) surface</b>	<b>65</b>
6.1	HRCLS data . . . . .	67
6.2	The LEED model . . . . .	69
6.3	Searching for a new model . . . . .	71
6.4	The new model: PdO(101)/Pd(100) . . . . .	74
6.4.1	Geometric consideration . . . . .	74
6.4.2	Compatibility with the STM data . . . . .	75
6.4.3	Surface core-level shifts . . . . .	78
6.5	Strained PdO(101)/Pd(100) . . . . .	80
<b>7</b>	<b>Thermodynamic stability/Phase diagrams</b>	<b>87</b>
7.1	Ab-initio atomistic thermodynamics . . . . .	87
7.2	Stability Range on Pd(111) . . . . .	90
7.3	Stability Range on Pd(100) . . . . .	93
<b>8</b>	<b>Conclusions and outlook</b>	<b>101</b>
<b>A</b>	<b>Basis set tests</b>	<b>103</b>
A.0.1	The bulk calculations . . . . .	104
A.0.2	The surface calculations . . . . .	106
<b>B</b>	<b>STM simulations</b>	<b>113</b>
B.1	LAPW5 . . . . .	113
	<b>Referenzen</b>	<b>117</b>

# List of Figures

2.1	Partitioning of the unit cell . . . . .	15
2.2	The supercell approach . . . . .	18
2.3	Flow chart of the WIEN program . . . . .	21
3.1	Equilibrium lattice constant for Pd . . . . .	24
3.2	Fcc crystal with 111 and 100 facets . . . . .	26
3.3	DOS for the Pd bulk and the Pd(111) surface. . . . .	29
4.1	Adsorption sites on the Pd(111) surface . . . . .	31
4.2	Oxygen binding energies for on-surface adsorption on Pd(111) . . . . .	33
4.3	Binding energies for chemisorbed O on the basal plane of the late 4 <i>d</i> transition metals at different coverages . . . . .	34
4.4	Illustration of the <i>d</i> -Band Model . . . . .	35
4.5	Relaxed O (2 × 2)/Pd(111) structure . . . . .	36
4.6	Relaxed O(2 × 1) and 3O(2 × 2) geometries . . . . .	37
4.7	Calculated change in the mean layer spacing $d_{12}$ with O coverage for Ru(0001), Ru(111), Pd(111) and Ag(111). . . . .	38
4.8	Workfunction and dipole moment dependence on the O coverage for Pd(111). . . . .	39
4.9	Difference electron density for 0.25ML and 1.00 ML O on Pd(111)	40
4.11	Surface Brillouin zone . . . . .	41
4.10	Density of states for the clean Pd(111) surface, (2x2)-O/Pd(111) and (1x1)-O/Pd(111) structures. Surface band structure for (1x1)- O/Pd(111). . . . .	42
5.1	High-symmetry sub-surface adsorption sites . . . . .	45
5.2	Structures with mixed on-surface/sub-surface site occupation . . . . .	48
5.3	Relaxed geometries for the most stable structures with mixed site- occupation at $\theta_{tot} = 1$ ML and $\theta_{tot} = 0.75$ ML . . . . .	52
5.4	Workfunction and dipole moment for structures with mixed fcc/tetra- I site occupation . . . . .	53
5.5	Difference electron density for (2 × 2) – (2 O <sub>fcc</sub> + O <sub>tetra-I</sub> )/Pd(111)	55
5.6	Average binding energy as a function of $(\theta, N_{sub}/N_{tot})$ . . . . .	57

5.7	Binding energies for sub-surface O incorporation into the tetra-I sites . . . . .	58
5.8	Electron density of relaxed and unrelaxed $(1 \times 1) - \text{O}_{\text{tetra-I}}/\text{Pd}(111)$ structures . . . . .	60
5.9	Binding energies for sub-surface O incorporation into the tetra-I sites, with removed deformation costs . . . . .	61
6.1	Adsorption sites on the Pd(100) surface . . . . .	65
6.2	Experimental HRCL spectra for structures forming on Pd(100) with increasing oxygen coverage . . . . .	68
6.3	Comparison of experimental HRCL spectra for the O 1s and the Pd $3d_{5/2}$ levels and calculated final-state shifts for the models considered for the Pd(100)- $(\sqrt{5} \times \sqrt{5})R27^\circ\text{-O}$ phase . . . . .	70
6.4	Structural models using the low index PdO surfaces considered for the Pd(100)- $(\sqrt{5} \times \sqrt{5})R27^\circ\text{-O}$ phase . . . . .	72
6.5	STM image of the Pd(100)- $(\sqrt{5} \times \sqrt{5})R27^\circ\text{-O}$ phase . . . . .	73
6.6	Several structural models considered for the Pd(100)- $(\sqrt{5} \times \sqrt{5})R27^\circ\text{-O}$ phase . . . . .	74
6.7	Total energy landscape of different PdO(101) registries over the Pd(100) substrate . . . . .	75
6.8	Simulated STM images . . . . .	77
6.9	PdO(101)/Pd(100) geometric structure . . . . .	81
6.10	Comparison between the SCLS of PdO(101)/Pd(100) and PdO(101) . . . . .	83
7.1	Surface oxide on the Pd(111) surface . . . . .	90
7.2	Stability plot for O/Pd phases on the Pd(111) surface . . . . .	92
7.3	Stability plot for O/Pd phases on the Pd(100) surface . . . . .	95
7.4	Comparison of the experimental and theoretical $(p, T)$ -phase diagram for the O/Pd(100) system . . . . .	96
7.5	$(4 \times 4)$ surface oxide on Ag(111) . . . . .	97
7.6	Stability plot for O/Ag phases on the Ag(111) surface . . . . .	98
A.1	Cohesive energy of palladium as a function of k-points/coverage. . . . .	105
A.2	Surface energy of palladium as a function of k-points/coverage. . . . .	107
A.3	Binding energy for O $(1 \times 1)$ /Pd(111) as a function of k-points/coverage. . . . .	108
A.4	Binding energy difference for O $(1 \times 1)$ /Pd(111) as a function of k-points/coverage. . . . .	109



# List of Tables

4.1	Binding energies for on-surface adsorption . . . . .	32
4.2	Structural parameters for 0.25 ML oxygen adsorbed in fcc-hollow . . . . .	35
4.3	Workfunction and dipole moment dependence on the O coverage for Pd(111). . . . .	41
5.1	Binding energies for sub-surface adsorption . . . . .	46
5.2	Critical thermodynamic coverage, $\theta_c^{\text{thd}}$ , for oxide formation . . . . .	47
5.3	Binding energies for sub-surface adsorption . . . . .	50
5.4	Coverage dependence of the binding energy for fcc/tetra-I site occupation. . . . .	51
5.5	Bondlength O-Pd for $(2 \times 2) - (2 \text{O}_{\text{fcc}} + \text{O}_{\text{tetra-I}})/\text{Pd}(111)$ structure . . . . .	53
5.6	Change in workfunction and dipole moment of the $(0.50 \text{O}_{\text{fcc}}/0.25 \text{O}_{\text{tetra-I}})$ geometry with O coverage. . . . .	54
5.7	Critical thermodynamic coverage, $\theta_c^{\text{thd}}$ , for oxide formation . . . . .	58
5.8	Material properties of Ru, Rh, Pd and Ag . . . . .	59
6.1	Binding energies, workfunctions and structural parameters for O adsorbate structures on the Pd(100) surface . . . . .	66
6.2	Calculated and measured Pd 3d SCLS for the PdO(101)/Pd(100) model . . . . .	79
6.3	Calculated O 1s SCLS for the PdO(101)/Pd(100) model . . . . .	80
7.1	$\mu_{\text{O}}(T, p^0)$ . . . . .	89
7.2	Stability of different oxygen phases on the Pd(111) surface . . . . .	91
7.3	Stability of different oxygen phases on the Pd(100) surface . . . . .	94
A.1	Parameter combinations used for the lattice constant determination	104
A.2	Basis set parameters used for the surface calculations . . . . .	106
A.3	Convergence tests for the surface oxides on the Pd(100) surface . . . . .	110
B.1	The new <b>case.in5</b> file . . . . .	114



# Chapter 1

## Introduction

The interactions of oxygen atoms with transition metal surfaces play an important role in applications ranging from catalysis to corrosion. In the context of heterogeneous catalysis, one of the key reactions studied, is the catalytic oxidation of CO on transition metals. This is due not only to its technological importance (e.g. in car exhaust catalytic converters, where the active component are transition metals such as Pt, Pd and Rh) but also to its "simplicity".

Catalysis clearly involves a number of complex processes, namely the dissociation of molecules and the creation of chemically active species, the subsequent interaction and reaction between the particles to form a product, which then desorbs from the surface. Furthermore, it is possible (maybe likely) that the catalyst material is modified by some fragment of the reactant molecules (e.g. O) and thereby create an active species.

In recent years, the question has been raised, whether the metals are really the ones which further the CO to CO<sub>2</sub> conversion. The technical reactions proceed at rather oxidising condition with atmospheric pressures and elevated temperatures. It is therefore feasible, that the transition metal surfaces do not remain unaffected. Oxides, which only come into being in such an environment, may actually be the reactive centers, as has been indicated by experiments addressing the CO oxidation over Ru(0001) and Pt(110) surfaces [1, 2]. This change of emphasis from the metallic substrate to oxide surfaces has also led to the identification of oxide or "surface oxide" structures which appear on the (111) surfaces of Pd [3] and silver [4, 5]. Furthermore, the formation of a palladium oxide on the Pd(100) surface has been connected to a significant increase in the CO oxidation rate [2].

These findings call for a deeper, atomistic understanding of the oxidation of transition metal surfaces, in particular an investigation of the ease (or resistance) of oxide formation that could then become relevant in the catalytic applications. To this end the interactions of the palladium (111) and (100) surfaces with oxygen atoms are studied in the present work with density-functional theory [6, 7] (DFT). To account for temperature and pressure effects, the stability of different surface

phases is then assessed using the concept of *ab-initio*, atomistic thermodynamics [8, 9, 10, 11, 12, 13, 14, 15].

The oxidation sequence can be roughly divided into pure on-surface (dissociative) adsorption, surface-oxide formation, and oxide film growth. As the oxygen chemisorption at single-crystal metal surfaces is often perceived to represent the initial step in the oxidation process, numerous studies aiming to understand the elementary processes involved in the oxidation reactions on Pd exist. The range of the employed experimental techniques is wide. For the O/Pd(111) system the following picture arises from this work. Above 200 K dissociative adsorption of oxygen [16] leads to a  $(2 \times 2)$  ordered overlayer, attributed to 1/4 ML [17] O sitting in the threefold hollow sites [18]. Higher oxygen coverages have been achieved at higher O<sub>2</sub> pressures and elevated temperatures, or by using stronger oxidants, such as NO [17] or NO<sub>2</sub> [19]. At higher coverages on-surface adsorption seems to compete with (surface) oxide formation, and depending on the oxygen dosage, oxidant gas and substrate temperature either a  $(\sqrt{3} \times \sqrt{3})R30^\circ$  [17], a complex [3, 17] or a  $(1 \times 1)$  [20, 21] low-energy electron diffraction (LEED) pattern have been reported. In joint experimental and DFT studies, the detailed atomic structure causing the complex LEED pattern has been recently identified as a surface oxide containing about 0.7 ML of oxygen atoms [3] and the 0.25 ML O  $(2 \times 2)$  structure has been analysed in detail [22].

On the theory side, there are few calculations devoted to the O/Pd(111) system. The molecular and dissociative chemisorption of NO on the unrelaxed Pd (100) and (111) surfaces has been studied with DFT [23]. The effect of cluster size on the properties of the oxygen atom on Pd(111) has been looked at [24]. The experimentally observed [18] molecular precursor states populated during the dissociative adsorption of O<sub>2</sub> on the basal surface of palladium have been confirmed theoretically [25].

The oxidation of the Pd(111) and the Pd(100) surfaces is qualitatively similar [26, 27]. The major difference between the two is that the (100) surface is far more reactive towards O<sub>2</sub> [27]. The adsorption of oxygen atoms on the Pd(100) surface leads to the formation of at least four ordered surface structures, as revealed by LEED investigations [28, 29, 30, 31]. The initially forming *p*  $(2 \times 2)$  and *c*  $(2 \times 2)$  structures, have been attributed to simple atomic oxygen overlayers at coverages 0.25 ML and 0.50 ML. At higher coverages, either a  $(5 \times 5)$  or a  $(\sqrt{5} \times \sqrt{5})R27^\circ$  structure is observed, depending on the exposure temperature and pressure. It has been suggested that the former corresponds to a PdO(110) plane [28]. The latter has been assigned to a rumpled PdO(001) plane on top of a distorted Pd(100) surface [32, 33]. The incompatibility of this assignment with either HRCLS, STM or DFT, triggered the search for a new structure. Consequently, it is suggested in this work that the  $(\sqrt{5} \times \sqrt{5})R27^\circ$  surface oxide is a strained, but commensurable PdO(101) film on top of Pd(100).

A further point of interest is the ease of oxide formation at the Pd(111) and Pd(100) surfaces. Since all the calculations in this work are performed on the

basis of density-functional theory, a parameter free characterisation of their oxidation behaviour can be made on an atomistic scale. The study of oxygen-metal interactions on the palladium (111) surface gives insight into the differences between the adsorption of oxygen on the surface and in the sub-surface region. While the first is governed by the extent of the  $d$ -band filling, the second depends also on the ease with which the surface can be deformed. A comparison to similar studies available for ruthenium, rhodium and silver [4, 34, 35] makes it possible to identify the ease of oxygen incorporation as the crucial step, which determines the on-set of oxide formation on these elements. This is linked to the material properties of the late  $4d$  transition metals, which have a decisive influence on the point when O starts to penetrate into the surface. In view of this (the initial incorporation of O into a transition metal surface) it can be expected that oxide formation on the more open (100) surface proceeds much easier, compared to the basal one. Indeed, one finds that from a thermodynamic point of view, the formation of the surface oxide on the Pd(100) surface sets in immediately after the stability of phases containing oxygen, exceeds the stability of the clean surface. For comparison, on the Pd(111) surface the  $(2 \times 2)$  adlayer structure is also found to be thermodynamically stable. What makes such a conclusion possible, is the knowledge of the varied oxygen structures studied on the (100) and the (111) surfaces and the use of the *ab-initio*, atomistic thermodynamics approach. In this context, the identification of the  $(\sqrt{5} \times \sqrt{5})R27^\circ$  structure as a strained, but commensurable PdO(101) film on Pd(100) plays an important role. It was a collaboration between theory and experiment, which made this identification possible. Comparing an experimentally measured "phase diagram" to the theoretical one, leads to the assessment of regions in  $(T, p)$  space, in which kinetic hindrances to the oxide formation play a role. They point towards limitations of both the thermodynamic theory and experiment.

This work is organised as follows. The theoretical background, i.e the many-body hamiltonian and the basics of DFT are described in the next chapter. The program package used for the calculations and the way to model surfaces are presented, as well. Chapter 3 proceeds with a study of the bulk and clean surface properties, before turning to the investigation of the oxygen atom interactions with the palladium surfaces. The chemisorption of O on the Pd(111) surface and the ensuing ordered structures are the subject of chapter 4. Hereby the relaxation behaviour upon oxygen atom adsorption on the basal surface of palladium is compared to the relaxation behaviour of Ru, Rh and Ag, its  $4d$  neighbours. Already here one finds indications for the importance the material properties of these elements have for the ease of oxide formation on them. This is then discussed in detail in the following chapter 5, in which structures with mixed on-/sub-surface oxygen site occupation are studied. The arguments leading to the rejection of an existing model for the  $(\sqrt{5} \times \sqrt{5})R27^\circ$  structure and its identification as a PdO(101) thin film, are presented in chapter 6. There a short introduction to STM simulations is given, as they were implemented into the WIEN97 program,

using the Tersoff-Hamann approximation, as part of this work. How to determine surface core-level shifts is described, as well. Finally, in chapter 6, the tools necessary to construct a stability plot of different phases, using the concept of *ab-initio*, atomistic thermodynamics are presented. The accumulated data on the O/Pd(111) and O/Pd(100) systems is used to construct such plots for them and the limitations of this method are discussed.

# Chapter 2

## Theoretical approach

Advances in computer power in recent years and the development of efficient first-principles electronic structure methods have given the theoretical treatment of surface structures and processes an enormous boost. The two main approaches to determine the total energy of a particular systems, which is a prerequisite for the theoretical description of surfaces, are either wave-function or electron-density based methods, originating from quantum-chemistry and solid-state physics, respectively. Each of them has the same footing, namely the quantum mechanical description of atoms and electrons. Electronic structure calculations of solids are dominated by density functional theory (DFT), which is also the method used in the present work.

### 2.1 The many-body problem

In order to analyse the physical and chemical properties of a system, it is necessary to know and diagonalise its Hamiltonian. Considering, however, that the systems of interest in solid state physics, typically consist of many particles of the order of Avogadro's constant  $N_A = 6.022 \times 10^{23} \text{mol}^{-1}$ , not the knowledge, but the diagonalisation of the Hamiltonian presents a problem. In fact, it is straightforward to write the many-body Hamiltonian down, as the only fundamental interactions of concern (in solid state physics) are the electrostatic ones. In principle, relativistic effects should be included, but for simplicity only the *non-relativistic* case is discussed in the following. Magnetic effects are neglected, as not being relevant for the present work. Therefore, a system of  $N_n$  nuclei with coordinates  $\{\mathbf{R}_I\}$  and  $N_e$  electrons at positions  $\{\mathbf{r}_i\}$  can be described by the non-relativistic Schrödinger equation with the Hamiltonian

$$H = T_{nucl} + T_{el} + V_{nucl-nucl} + V_{el-nucl} + V_{el-el} . \quad (2.1)$$

Here  $T_{nucl}$  and  $T_{el}$  represent the kinetic energy of nuclei and electrons, respectively, and are given by the following expressions

$$T_{nucl} = - \sum_{I=1}^{N_n} \frac{\hbar^2}{2M_I} \nabla_{\mathbf{R}_I}^2, \quad T_{el} = - \sum_{i=1}^{N_e} \frac{\hbar^2}{2m_i} \nabla_{\mathbf{r}_i}^2. \quad (2.2)$$

The Laplacian operators  $\nabla_{\mathbf{R}_I}^2$  and  $\nabla_{\mathbf{r}_i}^2$  involve differentiation with respect to the  $I$ -th nuclei, at position  $\mathbf{R}_I$  and the  $i$ -th electron, at position  $\mathbf{r}_i$ , while  $M_I$  and  $m_i$  denote their respective masses. The repulsive Coulomb interactions between the nuclei are represented by

$$V_{nucl-nucl} = \frac{1}{2} \sum_{\substack{I,J=1 \\ I \neq J}}^{N_n} \frac{Z_I Z_J e^2}{4\pi\epsilon_0 |\mathbf{R}_I - \mathbf{R}_J|}, \quad (2.3)$$

where  $Z_I$  and  $Z_J$  are the atomic numbers of nuclei I and J. Magnetic interactions due to the spin of the electrons and the spins of the nuclei could be considered in eq. (2.3) and in the equations representing the electrostatic potential energy due to the interactions between electrons and nuclei and the repulsion between the electrons,

$$V_{el-nucl} = - \sum_{i=1}^{N_e} \sum_{I=1}^{N_n} \frac{Z_I e^2}{4\pi\epsilon_0 |\mathbf{R}_I - \mathbf{r}_i|}, \quad V_{el-el} = \frac{1}{2} \sum_{\substack{i,j=1 \\ i \neq j}}^{N_e} \frac{e^2}{4\pi\epsilon_0 |\mathbf{r}_i - \mathbf{r}_j|}, \quad (2.4)$$

as well. The factor 1/2 in the expressions for  $V_{nucl-nucl}$  and  $V_{el-el}$  ensures that the interactions between the same pair of particles are not counted twice.

Now one has the means to describe any physical and chemical property of a system by solving the many-body Schrödinger equation

$$H\Psi(\mathbf{R}, \mathbf{r}) = E\Psi(\mathbf{R}, \mathbf{r}). \quad (2.5)$$

The whole physical information except for the symmetry of the wave functions,  $\Psi(\mathbf{R}, \mathbf{r})$ , is contained in the Hamiltonian. The only thing that has to be considered when solving this equation are the appropriate quantum statistics and, especially for heavier elements with very localised wave functions for the core electrons, relativistic effects are important, since the localisation leads to high kinetic energies of these electrons.

Unfortunately, a closed form solution of the Schrödinger equation is not possible, except for one particular case (the hydrogen atom) or for academic problems. To make a solution, at least within reasonable accuracy feasible, approximations have to be made. Still, even approximate solutions are far from being trivial.



## 2.2 Born-Oppenheimer Approximation

The first approximation in a hierarchy of such, is the *Born-Oppenheimer* [36] (BO) or also called *adiabatic* approximation. It is based on the observation that the electrons are much lighter (ca.  $10^4$  to  $10^5$  times) than the nuclei<sup>1</sup>. Hence it is supposed that electrons would instantaneously follow the motion of the nuclei, as they are much faster. The reaction time of electrons to a perturbation of the system is on a femto-second ( $10^{-15}$  s) scale, while atom cores react on a pico-second ( $10^{-12}$  s) scale. Therefore, it is assumed that as a first approximation the motions of the two systems ( $N_e$  electrons and  $N_n$  nuclei) are decoupled, i.e. the electrons stay in their ground state for any configuration of the nuclei. The nuclei distribution determines then the potential in which the electrons move. It should be kept in mind, however, that electron-phonon coupling is neglected, since only the current nuclei configuration is important. This means, that phenomena like conventional superconductivity or structural instabilities in some low-dimensional systems, such as the Jahn-Teller effect, cannot be described by the adiabatic approximation.

In practice, the full Hamiltonian is split. An electronic Hamiltonian  $H_{el}$  for fixed nuclear coordinates  $\{\mathbf{R}\}$  is defined as

$$H_{el}(\{\mathbf{R}\}) = T_{el} + V_{el-nucl} + V_{el-el}, \quad (2.6)$$

and the Schrödinger equation for the electrons for a given fixed configuration of the nuclei is

$$H_{el}(\{\mathbf{R}\})\Phi(\mathbf{r}, \{\mathbf{R}\}) = E_{el}(\{\mathbf{R}\})\Phi(\mathbf{r}, \{\mathbf{R}\}). \quad (2.7)$$

In both equations, the nuclear coordinates  $\{\mathbf{R}\}$  are not meant to be variables, but parameters. The nuclei, in turn, are assumed to move according to the atomic Schrödinger equation

$$(T_{nucl} + V_{nucl-nucl} + E_{el})\Lambda(\mathbf{R}) = E_{nucl}\Lambda(\mathbf{R}). \quad (2.8)$$

The potential energy surface (PES) or Born-Oppenheimer energy surface,  $V^{BO} = V_{nucl-nucl} + E_{el}$ , is taken to be the potential energy for the nuclear motion. Strictly speaking, this motion should be treated quantum mechanically. In practice, it is sufficient to solve a classical equation of motion for the nuclei, as quantum-mechanic effects, such as zero point vibrations or tunneling, are not really important. The only notable exception is hydrogen [37].

The properties of the systems and phenomena discussed in the present work can all be understood on the basis of the Born-Oppenheimer approximation. It has been also successfully applied in the theoretical description of different processes at surfaces. Still, the BO approximation is only justified, when there is no crossing of potential curves for different electronic states. But even then, in the case of states which have different symmetry, it might be a good approximation.

---

<sup>1</sup>Exceptions are hydrogen and helium, for which this approximation may be problematic.

## 2.3 Density-functional theory

The separation of nuclear and electron motion does unfortunately not reduce the order of the many-body problem. Such a reduction can be achieved if the many-electron problem is reformulated in terms of an effective one-electron picture.

In one of the earliest wave function based approximations, the *Hartree-Fock* (HF) method [38, 39], the many-electron wave function,  $\Phi(\mathbf{r}, \{\mathbf{R}\})$ , for a system of  $N_e$  electrons, is represented as a Slater determinant<sup>2</sup> of one-electron wave functions. This wave function is then used as a trial wave function, and the ground state of  $H_{el}$  is determined from a variational principle.

The representation of the wave function by a single determinant function includes Fermi statistics ("exchange" effects), but does not account for all correlation effects. Suffice it to say, that electronic screening is not described properly. In a somewhat unhappy definition, any effects not considered in HF are termed "correlation effects", i.e. the correlation energy is then the difference between the exact and the HF energy of a system ( $E_c = E_{tot} - E_{tot}^{HF}$ ). Electron correlation effects are commonly included in post HF methods, such as *Møller-Plesset* perturbation theory, *Configuration-Interaction* (CI) method or *Coupled-Cluster* (CC) theory. Such methods are, however, computationally very demanding and are currently limited to rather small number of atoms, typically about 10-20 [40].

The limitaion to systems with rather small number of atoms are encountered also by *quantum Monte Carlo* [41] (QMC) methods. QMC techniques are based on random sampling and can provide very accurate results.

In contrast, density-functional theory [6, 7, 42, 43] (DFT), has proven to be quite efficient for solving the many-body problem also for extended systems. DFT is a method based not on representation of the many-body wave function, but on the electron density. Its origins can be traced back to the works of Thomas and Fermi in the 1920s [44, 45].

### 2.3.1 The Hohenberg-Kohn theorems

The rigorous foundation of density-functional theory is put forward by a landmark paper by Hohenberg and Kohn(1964)<sup>3</sup>, in which they prove the following two theorems.

---

<sup>2</sup>The many electron wave function written in the form of a determinant, i.e.

$$\Phi(\mathbf{r}, \{\mathbf{R}\}) = \frac{1}{\sqrt{N_e!}} \begin{vmatrix} \phi_1(\mathbf{r}_1) & \phi_2(\mathbf{r}_1) & \cdots & \phi_{N_e}(\mathbf{r}_1) \\ \phi_1(\mathbf{r}_2) & \phi_2(\mathbf{r}_2) & \cdots & \phi_{N_e}(\mathbf{r}_2) \\ \vdots & \vdots & \ddots & \vdots \\ \phi_1(\mathbf{r}_{N_e}) & \phi_2(\mathbf{r}_{N_e}) & \cdots & \phi_{N_e}(\mathbf{r}_{N_e}) \end{vmatrix}. \quad (2.9)$$

<sup>3</sup>Walter Kohn was awarded the Nobel Prize in chemistry (1998) "for his development of the density-functional theory".

**Theorem1** states that the ground-state density  $n_0(\mathbf{r})$  of a system of interacting electrons in an external potential,  $V_{el-nucl}$  (potential of the atom-cores), uniquely determines this potential, within an additive constant. This means that any observable of this system, i.e. also the ground-state energy, can be written as a functional of the density,

$$E_v[n] = \int n(\mathbf{r})V_{el-nucl}(\mathbf{r})d\mathbf{r} + F_{HK}[n]. \quad (2.10)$$

The Hohenberg-Kohn functional,  $F_{HK}[n]$ , does not depend on the external potential and is therefore *universal*. It comprises the kinetic-energy functional for interacting electrons  $T_{el}$  and the electron-electron interaction potential

$$F_{HK}[n] = T_{el}[n] + V_{el-el}[n]. \quad (2.11)$$

**Theorem2** states that upon variation the energy functional  $E_v[n]$  assumes its minimum value for the ground-state electron density  $n_0(\mathbf{r})$ ,

$$E_0 = E_v[n_0] \leq E_v[n], \quad (2.12)$$

if the admissible functions are restricted by the condition

$$\int n(\mathbf{r})d\mathbf{r} = N_e, \quad n(\mathbf{r}) \geq 0. \quad (2.13)$$

Here the integral over the electron density gives the number of the electrons,  $N_e$ . The minimisation of the total energy is carried out under the constraint of electron number conservation, using the Lagrange method of undetermined multipliers. In this method the constraint is represented in such a way, that it is exactly zero when satisfied, i.e.  $\int n(\mathbf{r})d(\mathbf{r}) - N_e = 0$ . The constrained is then multiplied by the undetermined constant (the Lagrange multiplier) and added to the functional. Then the minimum of this expression requires that its differential is equal to zero, which means that a necessary condition for the minimum is given by

$$\delta\{E_v[n] - \mu[\int n(\mathbf{r})d(\mathbf{r}) - N_e]\} = 0. \quad (2.14)$$

This leads to the Euler-Lagrange equation:

$$\mu = \frac{\delta E_v[n]}{\delta n(\mathbf{r})} = V_{el-nucl}(\mathbf{r}) - \frac{\delta F_{HK}[n]}{\delta n(\mathbf{r})}. \quad (2.15)$$

Thus, the Lagrange multiplier  $\mu$  is the chemical potential of the electrons. Eq. (2.15) is the basic working equation of DFT.

A subtle aspect of the close association of electron density with ground state in the Hohenber-Kohn theorems is the existence of a one to one mapping between

ground-state wave functions and  $v$ -representable electron densities<sup>4</sup>. In other words, the ground-state properties are functionals of the electron density, only if the density is  $v$ -representable. The  $v$ -representability condition may present a serious difficulty, since many "reasonable" densities have been shown to be non- $v$ -representable [46]. Fortunately, DFT can be formulated in a way that only requires the density both in functionals and in variational principle to satisfy the weaker  $N$ -representability<sup>5</sup> condition [43].

This formulation is, so far, still exact. The problem of using many-body quantum wave functions with  $10^{23}$  coordinates, has been reduced to the variation of a function of three coordinates. Unfortunately, the Hohenberg-Kohn theorems only assert the existence of an universal density functional, but do not tell how to construct it.

### 2.3.2 Kohn-Sham equations

A crucial step towards turning density-functional theory into a practical tool for calculations is provided by a scheme for the treatment of the variational problem, proposed by Kohn and Sham [7] (KS). They invented an indirect approach to the kinetic-energy functional  $T_{el}[n]$  by introducing orbitals in such a way, that the kinetic energy is computed to good accuracy, leaving a small residual correction, which is handled separately.

The essence of the KS scheme is the existence of an auxiliary system of *non-interacting* particles, with kinetic-energy  $T_s$  and local single-particle potential  $v_s$ , such that the ground-state density,  $n_0(\mathbf{r})$ , of the interacting systems equals the ground-state density,  $n_{s,0}(\mathbf{r})$ , of the auxiliary system. This means, that from the "auxiliary" one-particle Schrödinger equation  $[-(\hbar^2/2m)\nabla^2 + v_s(\mathbf{r})]\phi_{s,i}(\mathbf{r}) = \epsilon_i\phi_{s,i}(\mathbf{r})$  one gets the representation of  $n_0(\mathbf{r})$  in terms of the lowest  $N_e$  single-particle orbitals as

$$n_0(\mathbf{r}) = \sum_{i=1}^{N_e} |\phi_{s,i}(\mathbf{r})|^2 . \quad (2.16)$$

Assuming that a potential,  $v_s(\mathbf{r})$ , generating the density, as given by the above equation, exists, uniqueness of this potential follows from the Hohenberg-Kohn theorem. Thus the single particle orbitals  $\phi_{s,i}(\mathbf{r}) = \phi_{s,i}([n]; \mathbf{r})$  and the non-interacting kinetic-energy

$$T_s[n] = \sum_i^N \langle \phi_{s,i}(\mathbf{r}) | -\frac{\hbar^2}{2m} \nabla_i^2 | \phi_{s,i}(\mathbf{r}) \rangle, \quad (2.17)$$

---

<sup>4</sup>A density is  $v$ -representable, if it is associated with the antisymmetric ground-state wave function of a Hamiltonian of the form  $H_{el} = T_{el} + V_{el-el} + V_{el-nucl}$  with *some* external potential  $V_{el-nucl}(\mathbf{r})$ .

<sup>5</sup>A density is  $N$ -representable, if it can be obtained from some antisymmetric wave function. Any nonnegative, continuous and normalised density  $n$  is  $N$ -representable.

are unique functionals of the density, as well.

Although uniquely defined for any density, the quantity  $T_s[n]$  is not the exact kinetic-energy functional  $T_{el}[n]$ , as given in eq. (2.11). To set up a problem of interest in such a way that  $T_s[n]$  is exactly its kinetic-energy component, the functional of eq. (2.11) is rewritten as,  $F[n] = T_s[n] + V_H[n] + E_{xc}[n]$ , where, by definition,  $E_{xc}[n]$  is the exchange-correlation energy functional of the *interacting* system

$$E_{xc}[n] \equiv T_{el}[n] - T_s[n] + V_{el-el}[n] - V_H[n] . \quad (2.18)$$

Therefore, for a particular external potential  $v(\mathbf{r})$  leading to ground-state density  $n_0(\mathbf{r})$ , Eq. (2.10) can be written in the form

$$E_v[n] = T_s[n] + \int n(\mathbf{r})v(\mathbf{r})d\mathbf{r} + \frac{1}{2} \frac{e^2}{4\pi\epsilon_0} \int \int \frac{n(\mathbf{r}')n(\mathbf{r})}{|\mathbf{r} - \mathbf{r}'|} d\mathbf{r}d\mathbf{r}' + E_{xc}[n] . \quad (2.19)$$

The variational principle leads to the Euler-Lagrange equation (cf. eq. 2.15)

$$\mu = v_{eff}(\mathbf{r}) + \frac{\delta T_s[n]}{\delta n(\mathbf{r})} , \quad (2.20)$$

where the Kohn-Sham *effective potential* is defined as

$$v_{eff}([n]; \mathbf{r}) = v(\mathbf{r}) + \frac{1}{2} \frac{e^2}{4\pi\epsilon_0} \int \frac{n(\mathbf{r}')}{|\mathbf{r} - \mathbf{r}'|} d\mathbf{r}' + v_{xc}([n]; \mathbf{r}) , \quad (2.21)$$

and the *exchange-correlation potential* is the functional derivative of  $E_{xc}[n]$ ,

$$v_{xc}([n]; \mathbf{r}) = \frac{\delta E_{xc}([n]; \mathbf{r})}{\delta n(\mathbf{r})} . \quad (2.22)$$

Equation (2.20) with the constraint (2.14) is exactly the same one as obtained from conventional density-functional theory when it is applied to a system of *non-interacting* electrons moving in an external potential  $v_s(\mathbf{r}) = v_{eff}(\mathbf{r})$ . This means, that for a given  $v_{eff}(\mathbf{r})$ , the density  $n(\mathbf{r})$  that satisfies the Euler-Lagrange equation (2.20) is obtained by solving the  $N_e$  one-electron equations

$$\left\{ -\frac{\hbar^2}{2m} \nabla^2 + v_{eff}([n]; \mathbf{r}) \right\} \phi_{0,i} = \epsilon_{0,i} \phi_{0,i} , \quad (2.23)$$

where

$$n(\mathbf{r}) = \sum_{i=1}^{N_e} | \phi_{0,i}(\mathbf{r}) |^2 . \quad (2.24)$$

The equations (2.21), (2.23) and (2.24) are referred to as *Kohn-Sham equations*. Since the effective potential  $v_{eff}$  depends on the density through the exchange-correlation potential (cf. 2.22), it is evident that the Kohn-Sham equations have

to be solved *self-consistently*. One starts from some initial guessed density  $n^{[0]}(\mathbf{r})$  (quite often taken to be a superposition of atomic densities) and constructs  $v_{eff}(\mathbf{r})$  from (2.21). From (2.23) and (2.24) a new density  $n^{[1]}(\mathbf{r})$  is determined. In each new iteration a mix of old and new density is used. The cycle is repeated until a certain *convergence* criterion is fulfilled.

Once the self-consistent electron density is obtained it can be used to compute the ground state electronic total energy via (2.19) or from the expression

$$E_0 = \sum_i^N \epsilon_i - \frac{1}{2} \frac{e^2}{4\pi\epsilon_0} \int \int \frac{n_0(\mathbf{r}')n_0(\mathbf{r})}{|\mathbf{r} - \mathbf{r}'|} d\mathbf{r}d\mathbf{r}' + E_{xc}[n_0] - \int v_{xc}([n_0]; \mathbf{r})n_0(\mathbf{r})d(\mathbf{r}) , \quad (2.25)$$

where the sum  $i$  is only over the filled states.

Given the auxiliary nature of the KS orbitals it can be expected that they have no simple physical meaning. Strictly speaking, this is true. However, from the asymptotic behaviour of the density, derived once from DFT and once from the many-electron Hamiltonian, it has been possible to identify the highest occupied KS orbital as the ionisation potential [47], i.e.  $\delta E_v[n]/\delta n(\mathbf{r}) = -I = \mu$ . Furthermore, Janak [48] has proven that the derivative of a generalisation of the total energy with respect to orbital occupation is equal to the eigenvalue of the effective one-electron Hamiltonian for an orbital, regardless of the detailed form of  $E_{xc}[n]$ ,

$$\epsilon_i = \frac{\partial E_v[n]}{\partial n_i} . \quad (2.26)$$

The generalisation of DFT is constructed by introducing occupation numbers  $n_i$  for each single-particle state and defining the charge density as

$$n(\mathbf{r}) = \sum_i^\infty n_i |\phi_{0,i}|^2 . \quad (2.27)$$

With the above two equation, the transition from a state with  $N_{el}$  – to a state with  $(N_{el} - 1)$  – electrons plus one free electron with energy zero, for an extended system, can be written as:

$$E_i^{N_{el}-1} - E^{N_{el}} = - \int_0^1 \epsilon_i(n_i) dn_i , \quad (2.28)$$

where the unoccupied state is denoted by  $i$ . This integral can be approximated using the mean value theorem of integration by evaluating the function inside the integral only at midpoint  $n = 1/2$ , i.e.  $E_i^{N_{el}-1} - E^{N_{el}} \approx \epsilon_i(n_i = 1/2)$ , which is called the Slater-Janak "transition state."

By the introduction of  $N_{el}$  one-electron wave functions, the KS equations allow the *indirect* but *exact* handling of the dominant part ( $T_s[n]$ ) of the true kinetic energy  $T_{el}[n]$ . However, one is now required to solve a set of  $N_{el}$  equations, in

contrast to the one equation needed in the original formulation (cf. Chapter 2.3.1). The only remaining problem is the ignorance regarding the exchange-correlation functional,  $E_{xc}$ . An explicit form for  $E_{xc}[n]$  is needed to specify the KS equation, therefore a number of approximations have been (and still are) developed.

### 2.3.3 Exchange-correlation energy functionals

The simplest approximation for the exchange-correlation energy function, is the *local-density approximation* (LDA). The exchange-correlation energy of the homogeneous electron gas, i.e., a system with a constant electron density [49] is known. In LDA this exchange-correlation energy for the homogeneous electron gas is also used for non-homogeneous situations. In other words, the exchange-correlation energy of an inhomogeneous system can be obtained by using the density of the homogeneous electron gas to approximate the inhomogeneous density in any point locally,

$$E_{xc}^{LDA}[n] = \int n(\mathbf{r})\epsilon_{xc}^{LDA}(n(\mathbf{r}))d\mathbf{r}. \quad (2.29)$$

The LDA is a good approximation for systems with slowly varying electron density, but for strongly inhomogeneous systems like, e.g. atoms or molecules, or reactions at surfaces, LDA results may not be sufficiently accurate. Usually LDA shows *over-binding*, i.e. binding and cohesive energy turn out to be too large compared to experiment. This overbinding also leads to lattice constants and bond lengths that are smaller compared to the experimental values.

An improvement on LDA is the *generalised gradient approximation* (GGA),

$$E_{xc}^{GGA}[n] = \int n(\mathbf{r})\epsilon_{xc}^{GGA}(n(\mathbf{r}), \nabla n(\mathbf{r}))d\mathbf{r}, \quad (2.30)$$

in which also a gradient of the density is included in the exchange-correlation energy. There are a number of approaches representing the exchange-correlation functionals within the GGA, which differ basically only in the determination of the coefficients for the differential term. Often the functional is split in two parts, i.e., for the exchange,  $E_x^{GGA}$ , and for the correlation,  $E_c^{GGA}$ , which are then developed separately. Usually theoretical considerations regarding the known behaviour of the exact, but unknown functionals, play a role in the development, but sometimes empirical parameters are used.

There are a number of failures of DFT with present-day functionals, which include that van der Waals forces are not properly described, the Kohn-Sham potential falls off exponentially for large distances instead of  $\propto 1/r$ , band gaps of semiconductors are underestimated in both LDA and GGA by approximately 50%, cohesive energies are overestimated in LDA and underestimated in GGA, strongly correlated materials (such as NiO) are predicted as metals and not as

antiferromagnetic insulators. The problem in the development of a more accurate exchange-correlation functional is the reliable description of the non-locality of this functional.

In the present work both LDA and GGA, in the form proposed by Perdew *et al.* (PBE) [50], were used to determine the bulk properties of palladium. For the surface calculation only GGA results will be presented.

## 2.4 The FP-LAPW method

The primary computational task in DFT is the solution of the KS equations for a given crystalline structure and chemical composition. To make this solution feasible in a periodic potential, the wave functions,  $\phi$ , are inevitably expanded, by a set of basis functions  $\varphi$ :

$$\phi = \sum_i c_i \varphi_i \quad (2.31)$$

Still, in any practical implementation the computational effort increases significantly with the number of electrons that have to be taken into account. The observation that the chemical binding is determined almost entirely by the valence electrons, while the influence of the core electrons is negligible, has given rise to the idea to replace the core electrons by an effective potential, so that they do not have to be taken explicitly into account. This is done in *pseudopotential plane wave* methods (PPW) [51, 52] and the set of functions chosen as a basis are *plane waves*. However, the use of pseudopotentials represents an approximation. For some elements, there is a significant interaction between core and valence electrons, or one may be interested in properties due to the core electrons. Such cases make all-electron calculations desirable, e.g. the (full potential) *Korringa-Kohn-Rostocker* method (KKR) [53, 54], the *linear muffin-tin orbital* method (LMTO) [55, 56, 57], the *full-potential linear augmented plane waves* method (FP-LAPW) [58]. In the mentioned methods the unit cell is partitioned in two regions (cf. Fig. 2.1), each of which is described by a different potential. The KKR method is Greens-function based. The functions used in both LMTO and LAPW methods are hybrids, constituted by solutions suitable for the two kinds of potentials *and* joined continuously at the boundary of the two disjoint regions. In both methods atom-like functions are used as basis for the wave-function expansion inside the spheres. Outside, Henkel- and Bessel-functions are used in the LMTO method, while plane waves are used in the LAPW method. They are augmented inside the muffin-tin spheres. In the following the LAPW method will be described in some detail.



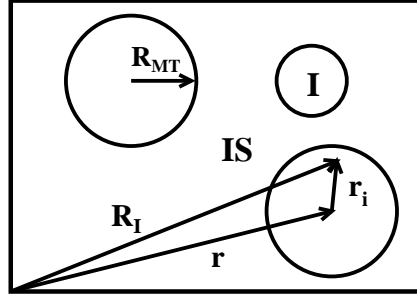


Figure 2.1: Partitioning of the unit cell into non-overlapping atomic spheres with radii  $R_{\text{MT}}^I$  and interstitial region (IS).

### 2.4.1 The APW- and LAPW-Methods

The idea to partition space into two disjoint regions was proposed by Slater already 1937 [59]. He noted that the potential, while being nearly spherical, varies strongly close to an atomic nucleus, but is much smoother between nuclei. Therefore, it seems reasonable to divide space into (i) non-overlapping spheres, centered at the atomic sites  $\mathbf{R}_I$  (cf. Fig.2.1) and (ii) interstitial (IS), which comprises all of the remaining space. The effective potential is approximated by a *muffin-tin* potential:  $V_{\text{eff}}$  is constant in the interstitial and radially symmetric within the spheres with muffin-tin (MT) radius,  $R_{\text{MT}}^I$ . Since plane waves are solutions of the Schrödinger equation for a constant potential, they are a good choice to describe a smoother potential region. The wave functions inside the spheres are solutions of the Schrödinger equation for a spherical potential,  $u_l(\mathbf{r}_i, \epsilon)Y_{lm}(\mathbf{r}_i)$ . The solutions,  $u_l(\mathbf{r}_i, \epsilon)$  of the radial Schrödinger equation

$$\left\{ -\frac{\hbar^2}{2m} \frac{d^2}{dr^2} + \frac{\hbar^2}{2m} \frac{l(l+1)}{r^2} + V_{00}(\mathbf{r}) - \epsilon \right\} r u_l(\mathbf{r}, \epsilon) = 0, \quad (2.32)$$

depend on the energy  $\epsilon$  as a parameter. The  $Y_{lm}(\mathbf{r}_i)$  are spherical harmonics, with  $Y_{l-m}(\mathbf{r}_i) = (-1)^m Y_{lm}^*(\mathbf{r}_i)$ . The spherical part,  $V_{00}$ , of the potential expansion is given by

$$V(\mathbf{r}) = \sum_{l=0}^{\infty} \sum_{m=-l}^l V_{lm}(\mathbf{r}) Y_{lm}(\mathbf{r}) \quad |\mathbf{r}_i| \leq R_{\text{MT}}. \quad (2.33)$$

The resulting *augmented plane wave* (APW) basis functions, introduced by Slater, are given by

$$\varphi_{\mathbf{k}+\mathbf{G}}^{\text{APW}}(\mathbf{r}) = \begin{cases} \frac{1}{\sqrt{\Omega}} e^{i(\mathbf{k}+\mathbf{G})\cdot\mathbf{r}} & \mathbf{r} \in \text{IS} \\ \sum_{lm} A_{lm} u_l(\mathbf{r}_i, \epsilon) Y_{lm}(\mathbf{r}_i) & |\mathbf{r}_i| \leq R_{\text{MT}} \end{cases} \quad (2.34)$$

where  $\mathbf{r}_i = \mathbf{r} - \mathbf{R}_I$  and  $A_{lm}$  are expansion parameters.

Augmented plane waves can be defined for any wave vector  $\mathbf{k}$  and any energy  $\epsilon$ ,

there is no constraint relating the two quantities. The augmented plane waves have, however, to be defined in such a way that they are continuous at the sphere boundary, for the kinetic energy to be well defined. This requirement defines then the expansion coefficients  $A_{lm}$  for any given combination of  $\mathbf{k}$  and  $\epsilon$ . There is no matching of derivatives at the sphere boundary, so that the APW basis functions have in general a kink at  $R_{\text{MT}}$  and their derivatives are discontinuous at the boundary<sup>6</sup>. A further drawback is the energy dependence of the functions  $u_l(\mathbf{r}_i, \epsilon)$ , leading to a non-linear eigenvalue problem, which is computationally quite demanding.

This problem is solved in the *linearised augmented plane waves* method (LAPW). In it both the basis functions *and* their first derivative are required to be continuous at the boundary between core and interstitial region. The additional matching in slope will yield smooth basis functions<sup>7</sup>. Since the matching criteria are strictly mathematical, the shape of the resulting linear combination will differ in general from the shape of the physical solution  $u_l(\mathbf{r}_i, \epsilon)$ . Only an approximate solution of the Schrödinger equation is possible, but the associated error is rather small [55]. The more important change is, that the radial functions  $u_l(\mathbf{r}_i, \epsilon)$  are expanded around a fixed energy

$$u_l(\mathbf{r}, \epsilon) = u_l(\mathbf{r}, \epsilon_l) + \dot{u}(\epsilon - \epsilon_l) + O((\epsilon - \epsilon_l)^2), \quad (2.35)$$

where  $\dot{u}$  is the energy derivative  $\dot{u} = (du_l(\mathbf{r}, \epsilon)/d\epsilon) |_{\epsilon=\epsilon_l}$ . The fixed energy  $\epsilon_l$  should be in the middle of the corresponding energy band. The additional term  $O((\epsilon - \epsilon_l)^2)$  leads to a 2<sup>nd</sup> order error in the wave functions and a 4<sup>th</sup> order error in the bandenergy.

All this makes the LAPW functions

$$\varphi_{\mathbf{k}+\mathbf{G}}^{\text{LAPW}}(\mathbf{r}) = \begin{cases} \frac{1}{\sqrt{\Omega}} e^{i(\mathbf{k}+\mathbf{G})\cdot\mathbf{r}} & \mathbf{r} \in IS \\ \sum_{lm} [A_{lm} u_l(\mathbf{r}_i, \epsilon_l) + B_{lm} \dot{u}_l(\mathbf{r}_i, \epsilon_l)] Y_{lm}(\mathbf{r}_i) & |\mathbf{r}_i| \leq R_{\text{MT}} \end{cases} \quad (2.36)$$

more flexible. Due to the small error the LAPWs are a good basis set choice for a relatively large energy region, making it often possible to treat all valence band by just one linearisation energy,  $\epsilon_l$ .

---

<sup>6</sup>The kinetic energy can be computed by either of the two integrals,  $\int \phi_i^* (-\nabla^2) \phi_j d\mathbf{r}$  or  $\int (\nabla \phi_i^*) (\nabla \phi_j) d\mathbf{r}$ . Ordinarily, it can be shown by integration by parts that the two integrals are equal, but if a function has anywhere a discontinuous slope, they differ by a surface integral over the surface of discontinuity. The first representation of the kinetic energy is more common, but the second integral is the more fundamental form, as it is the one which directly enters the variational principle from which the Schrödinger equation is derived. In the case of the APW basis functions the second integral is the correct one to use [59]. It should be stressed, that the surface contribution is not due to the kinks in the APW basis functions, but enters naturally from the variational expression.

<sup>7</sup>There will be no surface contribution to the kinetic energy.

Now the Kohn-Sham wave functions can be expanded in this basis

$$\phi_{\mathbf{k}} = \sum_{\mathbf{G}} c_{\mathbf{G}} \varphi_{\mathbf{k}+\mathbf{G}} . \quad (2.37)$$

A problem is encountered when states with the same  $l$  quantum number, but significantly different energies have to be treated. That are states with a different main quantum number  $n$ , since for each  $l$  there is only one energy parameter  $\epsilon_l$ . An attempt to describe both states by just one  $\epsilon_l$ , would lead to a poor description of one or both of them, depending on the choice of the linearisation parameter. This problem is solved by treating states which are not in the valence region, but too delocalised to be treated as core (which is the case for transition metals), as semi-core states described by *local orbitals*. The idea is to simply add a further function  $u_l(\mathbf{r}_i, \tilde{\epsilon}_l)$  to the expansion within the MT-spheres, with a second linearisation energy  $\tilde{\epsilon}_l$

$$\varphi_{lm}^{\text{lo}}(\mathbf{r}) = \begin{cases} 0 & \mathbf{r} \in IS \\ \sum_{lm} [A_{lm} u_l(\mathbf{r}_i, \epsilon_l) + B_{lm} \dot{u}_l(\mathbf{r}_i, \epsilon_l) + C_{lm} u_l(\mathbf{r}_i, \tilde{\epsilon}_l)] Y_{lm}(\mathbf{r}_i) & |\mathbf{r}_i| \leq R_{\text{MT}} . \end{cases} \quad (2.38)$$

The coefficients  $A_{lm}$ ,  $B_{lm}$  and  $C_{lm}$  are determined by the requirement that  $\varphi^{\text{lo}}(\mathbf{r})$  should be normalised and have zero value and slope at the sphere boundary. A local orbital is independent of  $\mathbf{k}$  and  $\mathbf{G}$ , it has a specific  $l$ -character and belongs to only one atom. The local orbitals are "local" in the sense that they are confined exclusively to the MT-region and are identically zero outside the muffin-tin sphere.

### 2.4.2 The FP-LAPW method

The restriction to spherical symmetric potentials in the core region and constant potential in the interstitial region can be lifted, further improving the LAPW method. Analogous to the wave function the potential is represented by

$$V(\mathbf{r}) = \begin{cases} \sum_{\mathbf{G}} V_{\mathbf{G}}^{\text{eff}} e^{i\mathbf{G}\cdot\mathbf{r}} & \mathbf{r} \in IS \\ \sum_{lm} V_{lm}^{\text{eff}}(\mathbf{r}_i) Y_{lm}(\mathbf{r}_i) & |\mathbf{r}_i| \leq R_{\text{MT}} \end{cases} \quad (2.39)$$

A lot of computational time can be saved by using the symmetry of the system to determine the relevant  $l, m$  coefficients for the expansion in spherical harmonics,  $Y_{lm}$ . This would mean that a smaller number of terms in the electron density expansion have to be considered.

There is a maximum  $l$  quantum number,  $l_{\text{max}}$ , which determines the size of the  $(l, m)$  representation for both wavefunction and potential inside the MT-spheres,

but it is different for  $\phi$  and  $V$ . Furthermore,  $|\mathbf{G}| \leq \mathbf{G}^{pot}$  determines the highest reciprocal lattice vector in the sum used to describe the potential in the interstitial region. By increasing these values the quality of the full-potential description can be improved systematically. These are values, which should be carefully tested, to determine an optimal basis set for a calculation.

The program used in this work, WIEN 97 [60] is based on the FP-LAPW method and will be described in the following.

### 2.4.3 The supercell method

A consequence of using periodic boundary conditions is, that a unit cell is repeated an infinite amount of times in either of the three directions in space  $x, y, z$ . This simplifies calculations for a bulk solid, as one has only to care about setting up the appropriate unit cell and using the whole symmetry of the system.

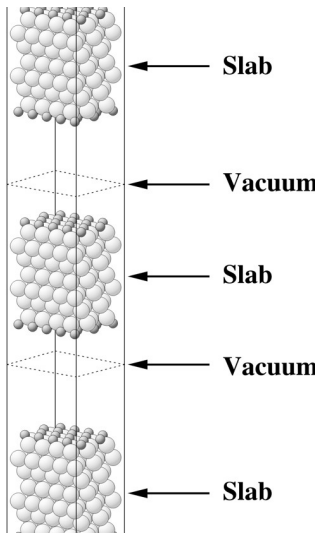


Figure 2.2: Illustration of the supercell approach. Shown is the supercell used to perform calculations for the adsorption of a full monolayer of oxygen atoms on the Pd(111) surface.

Going from bulk to a surface means a break in symmetry. A surface calculation can be set up by introducing a vacuum region into the unit cell. There are two ways to do this. If a vacuum region is introduced in every direction in space one ends up with a *cluster*, which should then represent the solid with the according surface. However, in this approach the properties of the surface depend very much on the size of the cluster. To be able to give a good description of the surface huge clusters, consisting of many atoms in one unit cell have to be used, which would make such a calculation computationally very expensive.

A different way to describe the surface is given by the *supercell* approach, which is used in the present work. In this approach a vacuum region is introduced just in one direction, e.g.  $z$ . This partitions the unit cell in regions where there is a solid (slab) and regions with vacuum. The periodic boundary conditions ensure, that the slab is infinite in  $x, y$  direction, but also, that the slab is repeated an infinite amount of times in  $z$  direction. To avoid spurious effects due to an interaction between consequent slabs, one has to make sure, that the vacuum region between them is big enough. As can be seen in Fig. 2.2 a slab has two surfaces. A slab should be thick enough, so that surface-surface interaction is negligible for the quantities of interest. Ideally, a slab would be so thick, that it is bulk-like in the middle. Both vacuum- and slab-thickness have to be tested, to ensure a good description of the surface properties.

Atoms or molecules are usually adsorbed on both surfaces simultaneously. This ensures, that at least inversion symmetry is retained, if possible. The presence of inversion symmetry reduces the computational effort by a factor of four, since the performed calculations are in real (and not in imaginary) space. The adsorption of atoms or molecules on just one side of a slab can also give rise to a huge dipole moment. The correction for this is simple [61] but not implemented in the WIEN code. Consequently in the present work the oxygen atoms are always adsorbed on both sides of the slab.

#### 2.4.4 Integration over the Brillouin zone

To determine the electron density a summation over all occupied states has to be performed. For a solid this means that an integration over the Brillouin zone (BZ) or its irreducible part, when symmetry is accounted for, has to be performed. Numerically an integration is solved by transforming an integral into a sum over a finite number of  $\mathbf{k}$ -points:

$$\int_{BZ} \frac{1}{\Omega_{BZ}} d\mathbf{k} \longrightarrow \sum_{\mathbf{k}} w_{\mathbf{k}} . \quad (2.40)$$

The two predominant methods used to choose the  $\mathbf{k}$ -points in the Brillouin zone are the *tetrahedron* method [62] and the *special points* method [63].

In the WIEN 97 program the special points method after Monkhorst and Pack is used, in which the integrations are performed as weighted sums over a grid of representative  $\mathbf{k}$ -points. Initially a grid is constructed in the full Brillouin zone using given divisions of the reciprocal lattice vectors; the grid is chosen so that it is offset from  $\Gamma$  by 1/2 division in each direction. Sets of symmetry related  $\mathbf{k}$ -points are identified by sequentially applying the symmetry operations. One representative  $\mathbf{k}$ -point is then chosen from each set of equivalent points, and assigned a weight,  $w(\mathbf{k})$ , equal to the number of points in the set divided by the total number of points in the grid. These are the special points and associated weights.

For metals, where bands cross the Fermi energy,  $E_F$ , there is a discontinuity in the occupation and consequently also in the integration over the Fermi surface. The result is a bad convergence behaviour. For this reason the temperature is raised artificially and the determined free energy is interpolated back to  $T = 0$  K, after the integration.

#### 2.4.5 Forces in the FP-LAPW method

The determination of forces acting on the atoms, i.e. the change in energy due to a displacement of the atoms, opens up a good possibility to determine the ground-state geometry. Assuming that the external potential depends parametrically on

the position of the nuclei,  $v(\mathbf{r}; \{\mathbf{R}_i\})$ , it follows from eq. (2.19) that the gradient of the ground-state energy is given by [64, 65]:

$$-\frac{\partial E_v}{\partial \mathbf{R}_I} = - \int \frac{\partial v(\mathbf{r}, \{\mathbf{R}_I\})}{\partial \mathbf{R}_I} n(\mathbf{r}, \{\mathbf{R}_I\}) d\mathbf{r} - \int \frac{\delta E_v}{\delta n} \frac{\partial n(\mathbf{r}, \{\mathbf{R}_I\})}{\partial \mathbf{R}_I} d\mathbf{r}. \quad (2.41)$$

The first term is the Hellmann-Feynman force, which describes the pure electrostatic interaction of the electron charge density  $n(\mathbf{r}, \{\mathbf{R}_I\})$  and the potential of the ions,  $v(\mathbf{r}, \{\mathbf{R}_I\})$ . The second term is due to the *incomplete* basis set, giving rise to inaccuracies in the calculated electron density. This term would disappear if the variational problem was solved exactly. Since the basis set functions in the LAPW method are discontinuous in their second derivative, this leads to a position dependent discontinuity in the kinetic energy, which requires a further correction to the Hellmann-Feynman forces [66]. Calculation of forces is possible in WIEN97 [67]. This is quite important for the determination of relaxations at surfaces.

## 2.4.6 The Program WIEN 97

The calculations presented in this work were performed with the program package WIEN97 [60]. It is based on the FP-LAPW method and developed for calculations of crystals, i.e., periodic boundary conditions are implemented. A flow chart of the program is shown in Fig. 2.3. The program is divided into two parts - initialisation and main program (self-consistent cycle). Each of them is divided in sub-programs, connected by scripts.

In the initialisation the geometric and electronic structure of the system of interest are set up. The symmetry of the system and the  $\mathbf{k}$ -points, which will be used, are determined. During the initialisation electron densities of free atoms are calculated and superposed to get an initial guess for the charge density used in the self-consistent cycle.

In the main part of the programm, as a first step a potential is generated from the input charge density. With the Hamiltonian determined by this potential the eigenvalue problem is solved for the valence electrons. From the calculated eigenfunctions a new valence electron density is obtained. The core electron energy and density are determined by a fully relativistic self-consistent calculation in the crystal potential. In the end, the new valence and core electron densities are mixed<sup>8</sup> with the *old* electron density, using a Broyden mixing scheme [58]. Ideally, convergence is reached, when old and new electron density do not differ. In practice, the convergence with respect to some convergence criteria is tested.

---

<sup>8</sup>The time required to perform a self-consistent calculation using the LAPW method is proportional to the number of iterations needed to reach self-consistency. It is, therefore, important to choose an efficient mixing of input and output electron densities. Problems like "charge sloshing" (oscillations of charge between two parts of a cell, characteristic especially for large unit cells) can be encountered otherwise.

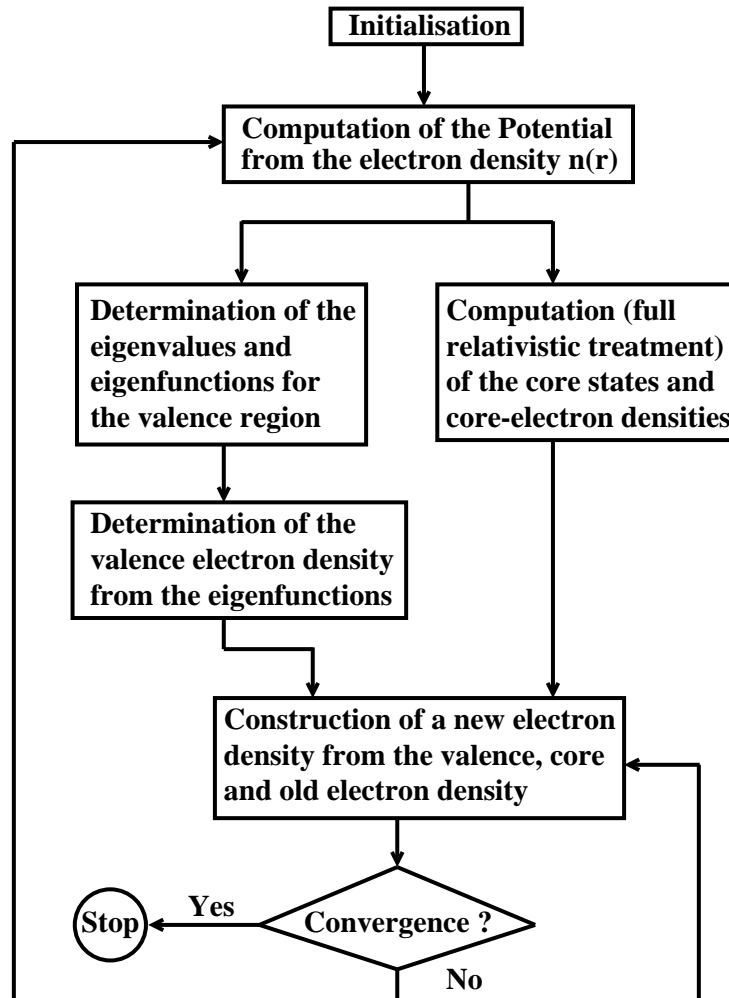


Figure 2.3: Flow chart of the WIEN program. The self-consistent part of the program is shown in detail.

If the convergence criteria is fulfilled, the ground-state has been found, otherwise the cycle is repeated.





# Chapter 3

## Properties of the bulk and clean surface

When dealing with surfaces it is important to remember that a surface is not an entity on its own, but connected to the bulk. This means that characteristic features of the bulk material will probably have a strong influence on the surface properties and behaviour. To mention but one example - the introduction of unwanted strain effects into a system may easily occur, if the equilibrium lattice constant is not determined in advance. Though this work will focus on surfaces, from the above it is clear that a study of the bulk and its features is crucial, if one wants to gain understanding of surfaces.

It should be further pointed out, that adsorption of atoms or molecules usually alters the structural and electronic properties of the surface they are adsorbed on. Effects due to the interaction of the adsorbed atoms/molecules can be identified by comparison to the clean surface, which is then taken as a reference.

Therefore, the properties of the palladium bulk and the clean (100) and (111) surfaces will be the focus of this chapter.

### 3.1 Properties of the bulk

Palladium is one of the late  $4d$  transition metals. It has 46 electrons and a nearly full  $4d$  shell. Its neighbours in the periodic table are ruthenium, rhodium (to the left) and silver (to the right). The equilibrium crystal phase of Pd has a face-centered cubic Bravais lattice, with one atom in the primitive unit cell [68]. Its measured lattice constant at room temperature is  $a_{exp} = 3.89 \text{ \AA}$  [69], which means that the distance between two Pd atoms in the bulk is  $2.75 \text{ \AA}$ . Consequently, the muffin-tin spheres in the calculation (which should not overlap) are chosen to be  $R_{MT}(\text{Pd}) = 2.37 \text{ bohr} = 1.25 \text{ \AA}$ <sup>1</sup>. Since the number of plane waves needed to

---

<sup>1</sup>Here and in the following atomic units are used:  $\hbar = m_e = e = 1$ ;  $4\pi\epsilon_0 = 1$ .  
1 bohr = 0.529177  $\text{ \AA}$

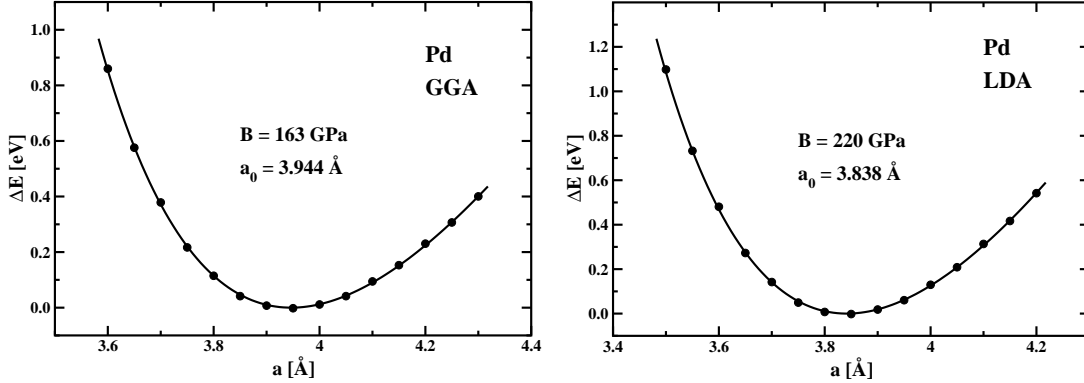


Figure 3.1: Calculated equilibrium lattice constant for palladium, determined with both GGA (left) and LDA (right).

describe the wavefunction decreases, as the interstitial region becomes smaller, one would typically like to make any muffin-tin radius as big as possible.

Some of the most important bulk cohesive properties are derived from the dependence of the total energy function on the volume of the primitive unit cell<sup>2</sup>. The equilibrium unit cell volume  $V = V_0$  (and hence the equilibrium lattice constant  $a_0$ ) is determined by minimisation of the total energy function,  $E(V)$ , with respect to  $V$ . The bulk modulus, on the other hand, is related to the curvature of the of the total energy function,  $E(V)$ , close to the equilibrium value. It defines the way a system reacts against isotropic compression and is given by

$$B(T, V) = V \left. \frac{\partial^2 E}{\partial V^2} \right|_T. \quad (3.1)$$

In practice, one evaluates the energy for different primitive unit cell volumes, i.e., different lattice constants, and then interpolates between them using the equation of state of the solid. In the present work the Murnaghan equation of state [70, 71],

$$E(V) = E(V_0) + \frac{B_0 V_0}{B'_0(B'_0 - 1)} \left[ B'_0 \left( 1 - \frac{V_0}{V} \right) \left( \frac{V_0}{V} \right)^{B'_0} - 1 \right], \quad (3.2)$$

is used<sup>3</sup>. Here,  $B'_0$  is the derivative of the bulk modulus with respect to pressure, evaluated at  $p = 0$ .

For the determination of the lattice constant several sets of parameters were used. These and further tests performed to determine the optimal basis sets used for

<sup>2</sup>The volume of the primitive unit cell is given by  $V = |\mathbf{a}_1 \cdot \mathbf{a}_2 \times \mathbf{a}_3| = \frac{1}{4} a^3$ , where  $\mathbf{a}_1$ ,  $\mathbf{a}_2$  and  $\mathbf{a}_3$ , are the primitive translation vectors of the face centered cubic Bravais lattice and  $a$  their length.

<sup>3</sup>This equation is based on the assumption, that the bulk modulus depends linearly on the applied uniform pressure,  $p$ , i.e.  $B(T, p) = B_0(T) + B'_0(T) p$ .

the different systems discussed in this work, are described in Appendix A<sup>4</sup>.

The equilibrium lattice constant for palladium is determined for both GGA,  $a_0 = 3.944 \text{ \AA}$  and LDA,  $a_0 = 3.838 \text{ \AA}$ . Comparison to the experimental lattice constant mentioned above shows that the DFT-GGA result slightly overestimates (by 1.3 %) and the LDA result underestimates (by 1.4 %) the experimental result. This behaviour has been noticed also for other metals [4, 34, 35]. The reason is the following: LDA typically causes an over-binding, which results in a smaller lattice constant. The opposite effect observed in GGA is a consequence of the correction, which GGA constitutes and which is too big. The determined bulk moduli are  $B_0 = 163 \text{ GPa}$  and  $B_0 = 220 \text{ GPa}$  for GGA and LDA, respectively. The experimental value is  $B_{exp} = 181 \text{ GPa}$  [69].

These results are in line with other FP-LAPW calculations. In Ref. [72] the equilibrium lattice constant and the bulk modulus are determined to be:  $a_0 = 3.95 \text{ \AA}$ ,  $B_0 = 1.63 \text{ GPa}$  for GGA and  $a_0 = 3.85 \text{ \AA}$ , and  $B_0 = 2.22 \text{ GPa}$  for LDA. In Ref. [73] the values for the lattice constant are  $a_0 = 3.95 \text{ \AA}$  (GGA) and  $a_0 = 3.85 \text{ \AA}$  (LDA). Previous pseudopotential DFT-GGA calculations find the lattice constant to be  $a_0 = 3.98 \text{ \AA}$  [25] and  $a_0 = 4.01 \text{ \AA}$  [22] overestimating the experimental value as well.

The cohesive energy is obtained by the following relation,

$$E_c = E_{\text{tot}}^{\text{bulk}}(a_0) - E_{\text{tot}}^{\text{atom}}, \quad (3.3)$$

with  $E_{\text{tot}}^{\text{bulk}}(a_0)$  being the ground state total energy per atom (calculated at the equilibrium lattice constant) and  $E_{\text{tot}}^{\text{atom}}$ , the energy of a free atom. The calculation for the Pd atom was performed in a cell with sides  $(13 \times 14 \times 15)$  bohr, to avoid spherical averaging. Dispersion does not play a role for a free atom, therefore it is sufficient to use one  $\mathbf{k}$ -point, i.e.  $(1/2; 1/2; 1/2)_{\frac{\pi}{a}}$  was used in the present work. It should be stressed that it is important to perform a *spin-polarised* calculation for the atom.

With this procedure the energy of palladium is determined as  $E_c = 3.64 \text{ eV/atom}$ . The experimental value is  $E_0 = 3.94 \text{ eV}$  [69].

During the course of this work, the necessity to perform calculations concerning the oxygen adsorption on Ag(111) arose. The equilibrium lattice constant determined for silver is  $a_0 = 4.15 \text{ \AA}$  and the bulk modulus is  $B_0 = 81 \text{ GPa}$ , obtained by using DFT-GGA.

## 3.2 Clean surface

Cleaving a bulk in any direction leads to the creation of a surface. A surface is called *ideal* or "truncated bulk" if it remains unchanged after the cleavage.

---

<sup>4</sup>Only deviations from the usually employed basis sets will be explicitly mentioned throughout the text.

However, it is obvious that the bonding situation of the atoms at the surface is different compared to the bulk. Some bonds have been severed and the resulting forces, which act on the atoms, lead to a displacement from their bulk-like positions. Basically, there are two kinds of rearrangements that may occur. Overall changes in the surface layer(s), with atoms moving in a way that changes the periodicity of the surface are called *reconstructions*. Motions involving whole layers of atoms, but no rearrangement of atoms within a layer, i.e. the lateral periodicity is retained, are called *relaxations* [74].

The two surfaces considered in this work are the (111) and the (100) (shown in Fig. 3.2). The (111) is close packed and has a sixfold symmetry axis. The (100) surface is more open and has a fourfold symmetry axis. All the unit vectors have a length equal to the next nearest neighbour distance:  $\sqrt{2}a_0/2$ , where  $a_0$  is the bulk lattice constant. On the (111) surface they form an angle of  $120^\circ$  and they are perpendicular to each other on the (100) surface.

The cleaving of a crystal, results in the formation of two surfaces of area  $A$ . This is not a spontaneous process and requires a certain amount of energy. As a consequence, the internal energy,  $E$ , which defines the properties of any system with  $N$  particles and entropy  $S$  increases by an amount proportional to  $A$ . The internal energy for one half of the crystal is then

$$E = TS - pV + \mu N + \gamma A, \quad (3.4)$$

where the proportionality constant  $\gamma$  is called *surface energy*. It is the energy needed to create a surface and its unit is energy per area. The surface energy is an important quantity, which plays a key role for the determination of the equilibrium shape of a crystal. A general expression for the surface energy can be obtained by identifying the Gibbs free energy ( $G = E - TS + pV$ ) in the equation above:

$$\gamma = \frac{1}{A} [G - N\mu]. \quad (3.5)$$

For the simple case of an fcc crystal without a basis, which is the case for both Pd(111) and Pd(100), this formula can be further simplified:

$$\gamma = \frac{1}{2A} (E_{tot}^{slab}(N_{Pd}) - N_{Pd} \cdot E_{tot}^{bulk}). \quad (3.6)$$

$E_{tot}^{slab}$  and  $E_{tot}^{bulk}$  are the ground state total energies of a slab (with  $N_{Pd}$  palladium atoms) and of the bulk, determined by DFT. The factor  $\frac{1}{2}$  takes into account,

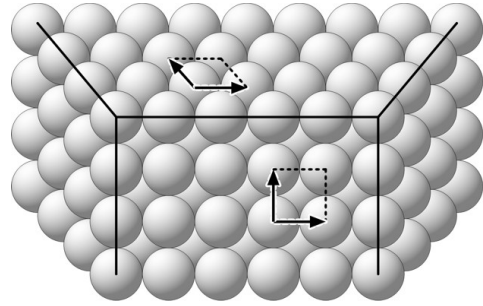


Figure 3.2: View of an fcc crystal with 111 facets and one 100 face (to the front). The primitive vectors of each surface, spanning a (1x1) cell are shown as well.

that the slab has two (equivalent) surfaces. Should the surfaces not be equivalent, the above formula (3.6) cannot be applied. At the absolute zero ( $T = 0$  K), in vacuum ( $p = 0$  atm) and neglecting zero point vibrations, the calculated surface energy for Pd(111) is  $\gamma = 0.56$  eV/atom and for Pd(100),  $\gamma = 0.88$  eV/atom.

Both the Pd(111) [75, 76] and Pd(100) [28] surface do not reconstruct, so one only has to be concerned with relaxations. When a surface relaxes, the topmost layer moves either inward or outward, diminishing or increasing the distance between the surface layers. Subsequent layers can be affected as well, though often their displacement is less pronounced. Depending on the character of the atomic bonds in the bulk (if they are more ionic or more covalent), there are different models which try to explain the relaxations on a microscopic level. For an ionic solid, held together by coulomb forces, rather than local bonds, the surface configuration is determined by a balance between those and the core repulsion. Due to the predominant long-range attraction between the atoms in the crystal, the lattice is compressed. Creation of a surface, releases the compression, so that the surface of the crystal should expand. For covalent compounds without long-range core attractions a contraction is often observed. It is explained in terms of reinforcement of the bond to lower laying layers through the unsaturated bonds of the surface atoms.

For the surface relaxation of metals, various models have been proposed. The model by Finnis and Heine [77], to mention but one of them, is based on the concept of Smoluhowski smoothing [78]: if a perfect crystal is cut along the boundaries of Wigner-Seitz cells, an artificial surface is created. Due to the symmetry and neutrality of each Wigner-Seitz cell, there will be no electrostatic force acting on a nucleus, if the charge density is not allowed to relax. After relaxation, however, the density smoothens out and the charge redistribution gives rise to an inward electrostatic force on the top-layer nuclei.

When a metal surface forms, the atoms of the top layer often move towards the bulk<sup>5</sup>, diminishing the interlayer spacing,  $d_{ij}$ . The next layer relaxes in the opposite direction, i.e. outwards, expanding the distance to the following layer. The displacement in the atomic positions is smaller and is further damped toward the inside of the bulk. For the  $\{111\}$  direction in a fcc crystal the distance between subsequent layers in the bulk (or unrelaxed clean surface), is  $d_b = \sqrt{3}a_0/3$ , where  $a_0$  is the equilibrium lattice constant. The change in interlayer spacing is then (in %):

$$\Delta d_{ij} = [(d_{ij} - d_b) \times 100]/d_b. \quad (3.7)$$

For the clean Pd(111) surface an almost negligible contraction of  $d_{12} = 0.03\%$  with respect to the bulk value  $d_b = 2.277$  Å is found for the topmost Pd-Pd interlayer spacing. The distance between the second and third layer shows a similarly insignificant expansion of  $d_{23} = 0.08\%$ .

---

<sup>5</sup>There are cases in which the top layer relaxes outwards, e.g. Beryllium.

The atomic arrangement of atoms at solid surfaces can be determined experimentally with high accuracy using low energy electron diffraction (LEED) measurements. Several studies are available for the clean Pd(111) surface, with which the calculations are in good agreement. In Ref. [75, 76, 79] only a slight expansion (ca. 1%) of the first interlayer spacing  $d_{12}$  is found, which (according to the authors) might also be due to the presence of some residual hydrogen. In Ref. [22, 80, 81] no indication of surface relaxations is found. In the last reference this is further supplemented by similar DFT findings. The value mentioned for the bulk interlayer spacing is 2.25 Å [75, 76, 79].

In its almost nonexistent surface relaxation, clean palladium (111) differs from its left-hand neighbours in the periodic table, which both show an appreciable first interlayer contraction: -3.9% at Ru(0001) [82] and -1.8% at Rh(111) [35]. This behaviour reflects the variation of the metal bond strength with increasing  $d$ -band occupation as discussed by Methfessel *et al.* [83]. The magnitude of the relaxation exhibited over the transition metal series shows a parabolic dependence on the  $d$ -band filling. It mirrors the bonding-antibonding parabola and is therefore largest for a half-full  $d$ -band. As the  $d$ -band is subsequently filled from Ru to Pd, being almost fully occupied in the case of the latter, the very small contraction for the Pd(111) clean surface is to be expected. For Ag, as the right-hand noble neighbour of Pd in the periodic system, the increase in  $sp$ -charge leads even to a 0.5% expansion.

The workfunction  $\Phi$  of a crystal surface is defined as the minimum energy required to remove an electron from the crystal to any point outside the surface, at a distance small compared to the surface dimensions, but large compared to the lattice constant  $a_0$ . Therefore, the workfunction is by definition

$$\Phi = \phi(\infty) + E_{N-1} - E_N . \quad (3.8)$$

Here  $\phi(\infty)$  is the total electrostatic potential far from the surface,  $E_N$  and  $E_{N-1}$  are the ground-state energies of a neutral  $N$ -electron crystal and of the singly ionised crystal (one electron is removed from the system), respectively. The electron-spillover at the surface leads to the creation of a dipole layer, which the electron has to overcome, in order to leave the solid. This requires work. The workfunction can be therefore expressed in terms of the change in electrostatic potential across the dipole double layer and the chemical potential, i.e., using the definition of the chemical potential  $\mu = \partial E / \partial N = E_N - E_{N-1}$  [84]

$$\Phi = \phi(\infty) - \mu = [\phi(\infty) - \bar{\phi}] - \bar{\mu} . \quad (3.9)$$

$\bar{\phi}$  is the average of the total electrostatic potential over the metal and  $\bar{\mu}$  is the bulk chemical potential relative to the interior potential.

In the case of a metallic system, the chemical potential is equal to the Fermi energy,  $E_F$ , the value of the highest occupied Kohn-Sham eigenvalue, therefore

$$\Phi = \phi(\infty) - E_F . \quad (3.10)$$

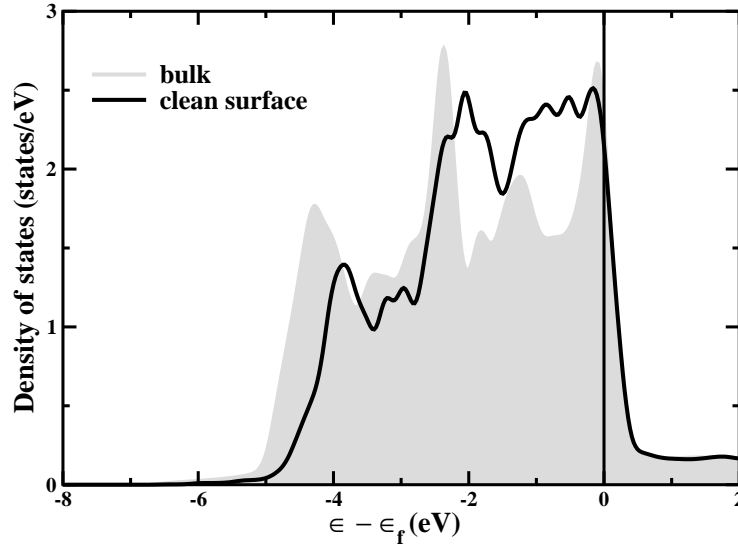


Figure 3.3: Total DOS for palladium bulk (grey shaded area) and for the Pd(111) surface top layer atoms (black line).

Since the workfunction is related to the dipole barrier at the surface, which an electron must transcend in order to escape from the solid, it is obviously dependent on the surface termination. This is reflected in the values calculated for two of the low index surfaces of Pd. The value of the workfunction at the Pd(111) surface is  $\Phi = 5.25$  eV, while  $\Phi = 5.16$  eV is obtained for the (100) surface. From photoelectric experiments the workfunction for a polycrystalline Pd sample is measured to be 5.12 eV [85] and 5.6 eV for crystalline Pd(111) [86]. The noticeable difference between theory and experiment (0.35 eV) is in line with other GGA calculations. In Ref. [83] the following values obtained from FP-LMTO calculations are reported:  $\Phi(\text{Pd}(111)) = 5.53$  eV and  $\Phi(\text{Pd}(100)) = 5.30$  eV.

In the end, it is interesting to take a look at the changes the density of states (DOS) undergoes at a surface. The total DOS of a palladium bulk and the total DOS of the surface layer atoms of a Pd(111) surface are shown in Fig. 3.3. The DOS is comprised mostly of  $d$ -states. A narrowing of the  $d$ -band at the surface, compared to the bulk, is clearly seen. This can be understood by the following simple model [87]. At the surface the coordination of the atoms is reduced compared to the bulk. For the surface to retain its charge neutrality, the center of the  $d$ -band shifts. This shift is negative for less than half-filled  $d$ -bands and positive in the opposite case. This shift increases with the number of broken bonds at the surface.

For palladium, which has an almost full  $d$ -band the band center moves upwards, i.e. towards  $E_F$ .





# Chapter 4

## Oxygen adlayers on Pd(111)

This chapter will focus on the on-surface chemisorption of oxygen on Pd(111) for coverages up to one monolayer (ML). For a fully adsorbate covered surface, i.e. 1ML, the number of oxygen atoms on the surface equals the number of substrate atoms in the first layer. A prerequisite for such a study is the knowledge of the sites available for on-surface adsorption, some of which are shown in Fig.4.1.

The high symmetry sites on the (111) surface are: on-top, bridge, and two hollow sites - hcp and fcc. (The sub-surface sites will be discussed in the following chapter). An atom adsorbed in an on-top site (not shown in Fig.4.1) is situated just above a substrate atom of the first layer. The bridge position is found between two first layer atoms. The two three-fold hollow sites differ only slightly - an oxygen atom in fcc is located above a palladium atom of the third layer, while an hcp site is above a palladium atom of the second layer. For and hexagonal close packed material (e.g. Ru) the situation is the same, with the sole exception that the "fcc" site has no atom below it.

The two primitive vectors of the (111) surface are also shown in Fig. 4.1. They form an angle of  $120^\circ$  and are connected to the equilibrium lattice constant  $a_0$  through the equation  $|\mathbf{a}_1| = |\mathbf{a}_2| = \sqrt{2}a_0/2$ , as mentioned in the previous chapter.

When an atom (or molecule) is adsorbed on a surface, it usually favours a given high symmetry site. Such a preference is identified by comparing the energetics

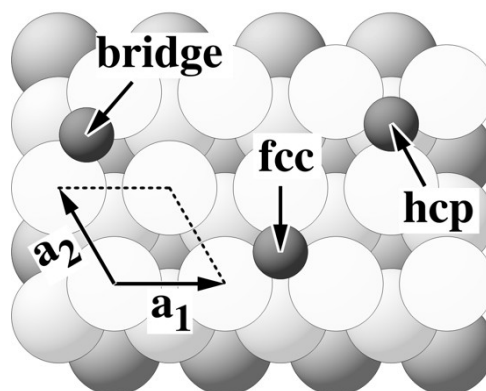


Figure 4.1: View of the Pd(111) surface. The palladium atoms are represented by the large white (1st layer) and grey (light grey: 2nd layer, dark grey: 3rd layer) circles. The small dark circles depict the oxygen atoms in different adsorption sites. The (1x1) cell, spanned by the primitive vectors  $\mathbf{a}_1$  and  $\mathbf{a}_2$  is shown as well.

of different geometries with the adsorbate in varying sites. The structure with the lowest energy is then the most stable one, within the subset of considered adsorbate phases at a certain coverage.

## 4.1 Energetics

To investigate the chemisorption of O on the Pd(111) surface, the oxygen coverage is increased from 0 to 1 monolayer (ML) in quarter ML steps. Zero coverage, obviously, corresponds to the clean surface.

The central quantity obtained from the DFT calculations is the average binding energy of oxygen defined as

$$E_b(\theta) = -\frac{1}{N_O} \left( E_{O@M} - E_M - N_O \left( \frac{1}{2} E_{O_2} \right) \right), \quad (4.1)$$

where  $N_O$  is the total number of O atoms (on-surface or sub-surface) present in the unit-cell at the considered coverage.  $E_{O@M}$ ,  $E_M$  and  $E_{O_2}$  are the total energies of the slab containing oxygen, the corresponding clean metal (111) slab and of an isolated oxygen molecule, respectively. The definition is such, that a positive number indicates that the dissociative adsorption of  $O_2$  is exothermic (stable) and a negative number indicates endothermic (unstable).

Structure	$\theta$	fcc	hcp ( $\Delta E$ )	br ( $\Delta E$ )
O - ( $2 \times 2$ )	0.25ML	1.47	1.24 (0.23)	0.93 (0.53)
O - ( $2 \times 1$ )	0.50ML	1.12	0.90 (0.22)	-
3O - ( $2 \times 2$ )	0.75ML	0.76	0.54 (0.22)	-
O - ( $1 \times 1$ )	1.00ML	0.38	0.12 (0.26)	-0.15 (0.53)

Table 4.1: Binding energies (in eV/atom) for O on Pd(111), relative to the dissociation energy of the oxygen molecule, for the investigated surface structures. The differences in binding energies,  $\Delta E$ , calculated relative to the respective fcc-hollow site value, are also given.

The calculated binding energies for the considered sites are summarized in Table 4.1. The oxygen prefers adsorption in the highly-coordinated hollow sites, in agreement with previous high-resolution electron energy loss spectroscopy (HREELS) [18] data and previous DFT calculations [25]. Furthermore, a preference for the fcc site over the hcp site is revealed, which is with  $\approx 0.2$  eV almost constant over the whole considered coverage range. For the two borderline cases at 0.25 ML and 1 ML coverage the bridge site between two palladium atoms was also tested. As expected [18, 25], it turned out to be less stable than adsorption in the hollow sites and is therefore not considered further. Still, it is interesting

to notice, that in both the  $O(2 \times 2)$  and the  $O(1 \times 1)$  the bridge site is about 0.5 eV less stable than the fcc sites, suggesting that the diffusion barrier also does not vary much with coverage.

The energy difference between the two hollow sites is similar to the one found on Rh(111) [35], while for O/Ru(0001) [34] it is large for lower coverages and only becomes as small as 0.1 eV for 1 ML. The preference for the fcc adsite on fcc Pd(111) is also consistent with observation on the basal plane of Ru, Rh and Ag, where oxygen is always found to occupy those sites that continue the bulk layer sequence (i.e. fcc on fcc Rh, Ag; hcp on hcp Ru) [4, 34, 35]. In this respect and similar to the conclusions of the study by Seitsonen *et al.* [22], this calculations cast severe doubt on the interpretation of ion scattering data by Steltenpohl and Memmel, determining the hcp site as the most stable O adsorption site on Pd(111) [88]. However, at this point one can not rule out, that the top layer of Pd(111) shifts upon oxygen adsorption (e.g. at steps), assuming a hcp stacking at the surface. Such a situation may confuse an experimental analysis. Calculations for Ru(0001) [89] show that such a shift is in fact likely, at least for Ru.

A marked decrease in the binding energy with increasing oxygen coverage is observed, cf. Fig. 4.2. This weakening of the adsorbate-substrate bond reflects the overall repulsive lateral interactions within the more and more densely packed electronegative overlayer. It favours the formation of dilute adlayer structures over dense islands. Should the slope of  $E(\theta)$  have had the opposite incline oxygen islands would have been the preferred structure. However, no conclusions can be drawn as to which ordered or disordered overlayers may actually form as a thermodynamik phase (allowing also for metastable states) on the basis of the few ordered structures calculated here. Such a statement requires the additional evaluation of a larger set of structures, leading to the construction of a lattice gas Hamiltonian, thus making the subsequent Monte Carlo calculations possible [90].

It is instructive to compare the interactions of palladium with oxygen, once more, to its 4d neighbours. Detailed studies on the oxygen adsorption in the coverage range up to 1 ML on Ru(0001), Rh(111) and Ag(111) are available from DFT calculations [4, 34, 35]. In particular the study by Ganduglia-Pirovano and Scheffler on Rh(111) [35] used a FP-LAPW setup analogous to the one of this work. The other two studies use the pseudo-potentials approach. The O/Ru(0001) system

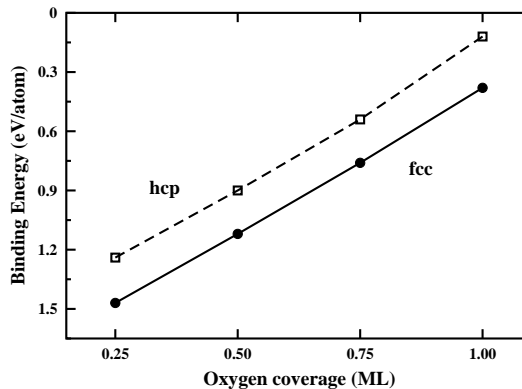


Figure 4.2: Calculated binding energies of oxygen on Pd(111) in fcc- (solid circle) and hcp- (open square) hollow sites, for various coverages, with respect to the dissociation energy of oxygen

has been also investigated with the FP-LAPW method [82]. To complete the study for all four elements within one method using a similar setup, several calculations for O on Ag(111) were performed<sup>1</sup>. This data is used to plot the dependence of the binding energy on coverage, for the most stable oxygen adsorption site on the basal plane of each of the considered elements, cf. Fig. 4.3. A similar decrease over the investigated coverage range, which agrees even in magnitude, is observed. While this suggests similar lateral interactions at these four surfaces, the *absolute* bond strength decreases progressively throughout the sequence of late 4d TMs.

In contrast to the highly exothermic binding of oxygen on Ru(0001), the bond strength on Ag(111) is already so small, that dissociative adsorption would be endothermic for coverages beyond 0.5 ML. The reason for this gradual weakening of the bond strength is the continued filling of the *d*-band towards the right of the periodic table. The consequence is an increased occupation of antibonding oxygen-metal states, which weakens the bonding [91]. To illustrate this concept, the projected local density of states for each of the four elements at a full ML coverage with oxygen, are shown in Fig. 4.4. The gray shaded area corresponds to the metal *d* projected DOS, while the dark shaded area shows the O *p*-states. The interaction of the adsorbate states with the narrow *d*-band of the metals gives rise to a split in the oxygen states into two states situated on both sides of the *d*-band. One state is bonding with respect to the adsorbate and the metal *d*-states and the other, above the *d*-band, is antibonding. A comparison of the four pictures shows that a continued filling of the metal *d*-states goes hand in hand with the population of antibonding states of oxygen. While for ruthenium the weight is on the side of the bonding states, the picture is completely reversed for silver.

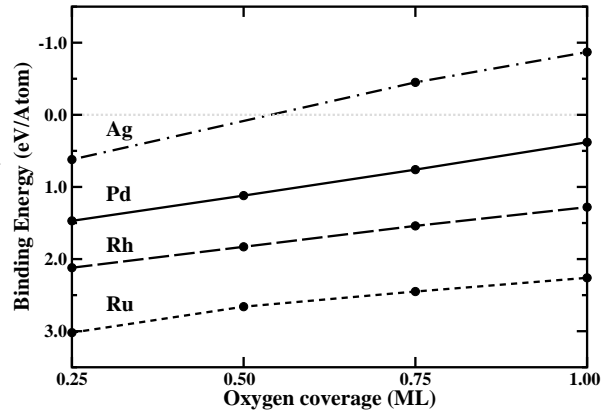


Figure 4.3: Calculated binding energy for on-surface O chemisorption on the basal surface on the late 4d transition metals. Shown is the energy of the most stable adsorption site in each case, i.e. hcp on Ru(0001) and fcc on Rh(111), Pd(111) and Ag(111). Data: O/Ru(0001) [82], O/Rh(111) [35], O/Ag(111) - this work, basis set described in footnote 1.

<sup>1</sup> $R_{\text{MT}} = 2.36$  bohr,  $R_{\text{MT}}^{\text{O}} = 1.3$  bohr, wave function expansion inside the muffin tin spheres up to  $l_{\text{max}}^{\text{wf}} = 12$ , potential expansion up to  $l_{\text{max}}^{\text{pot}} = 4$ , and local orbitals for the 4s and 4p semicore states of Ag, as well as for the O 2s. The energy cutoff for the plane wave representation in the interstitial region between the muffin tin spheres was  $E_{\text{wf}}^{\text{max}} = 17$  Ry for the wavefunctions and  $E_{\text{pot}}^{\text{max}} = 169$  Ry for the potential. A  $(12 \times 12 \times 01)$  Monkhorst-Pack grid with 19 irreducible  $\mathbf{k}$  points, was used for the Brillouin zone integration. To obtain the same sampling of the

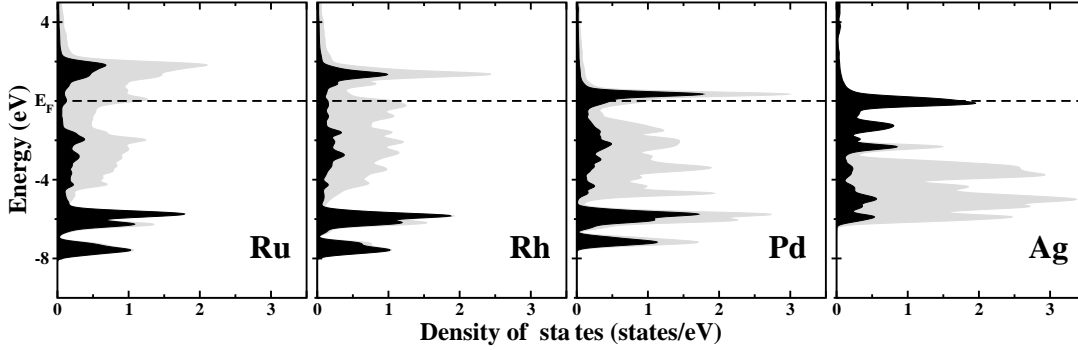


Figure 4.4: Density of states for 1 ML O adsorbed on the basal surface of the late 4d transition metals, projected on the metal 4d states (grey) and oxygen 2p states (black). All calculations were performed with FP-LAPW using the following basis set parameters: Ru - basis set as described in Ref. [89]; Rh -  $R_{\text{MT}}^{\text{O}} = 2.2 \text{ bohr}$ , all remaining parameters are as described for palladium in A.0.2; Ag - s. footnote 1.

#### 4.1.0.1 Oxygen induced surface relaxations

The presence of adsorbates can perturb the periodicity of the clean surface. It was shown in the preceding discussion that the oxygen-palladium interactions are sufficiently strong to favour the creation of commensurable overlayers, which then may have larger surface unit cells. Since the adsorbate coverage in the sub-monolayer range was increased in quarter monolayer steps,  $(2 \times 2)$  cells can be used to describe the ensuing structures. In the following, a detailed description

Geometry parameters	DFT-GGA ( $\text{\AA}$ )	LEED ( $\text{\AA}$ )[22]	DFT-GGA ( $\text{\AA}$ )[22]
$d_{\text{O-Pd}}$	1.99	-	1.97
$d_{01}$	1.16	$1.17 \pm 0.03$	1.16
$d_{12}$	2.29( 0.4%)	$2.30 \pm 0.03$ (2%)	2.34
$d_{23}$	2.27(-0.5%)	-	-
$d_b$	2.28	-	2.31
$\Delta z_1$	0.09	$0.07 \pm 0.03$	0.07
$\Delta z_2$	0.10	$0.08 \pm 0.05$	0.00

Table 4.2: Calculated structural parameters in  $\text{\AA}$  for the O- $(2 \times 2)$ /Pd(111) structure with O in the fcc-hollow position. For the interlayer distances, the center of mass of each Pd layer is used.  $d_{\text{O-Pd}}$  indicates the bondlength and  $\Delta z_1$ ,  $\Delta z_2$  the buckling in the first and second outermost layers, respectively. The percentual relaxations are calculated with respect to the bulk value (positive value means expansion, negative contraction). The experimental LEED data and pseudopotential DFT-GGA values are from Ref. [22].

reciprocal space for bigger surface cells, this number was reduced accordingly.

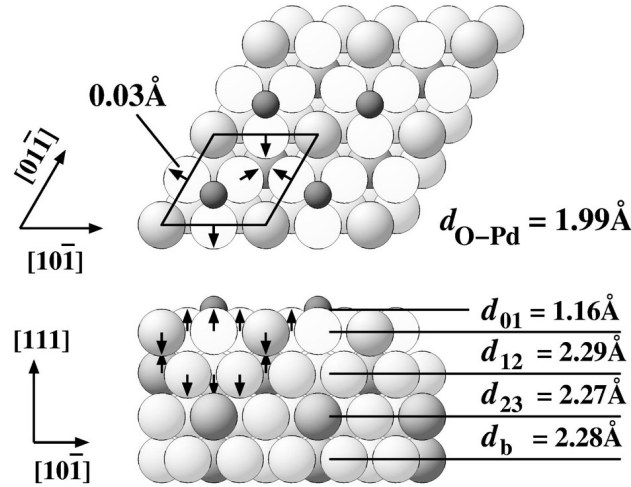


Figure 4.5: Top and side view of the atomic geometry of  $(2 \times 2)$ -O/Pd(111). The small dark grey circles represent the oxygen atoms. The large white and grey circles represent the palladium atoms, where those lying in the same plane and equivalent under the threefold symmetry have the same colour. The arrows (not drawn to scale) indicate the direction of the displacements of the substrate atoms with respect to the bulk positions.

of the relaxed atomic geometries for the most stable structures (i.e. oxygen adsorbed in fcc hollow site) at different coverages, is given. For each case the oxygen overlayer and the two outermost Pd(111) layers were fully relaxed. To determine interlayer distances, the center of mass of each layer is used.

At a 0.25 ML coverage one fourth of the available hollow sites are occupied giving rise to an O  $(2 \times 2)$  structure, see Fig. 4.5. This is the only hitherto experimentally analysed structure. The calculated geometry parameters are in good agreement with the existing LEED data [22], as summarised in Table 4.2. Oxygen pushes its three Pd neighbours a little bit radially away ( $0.03 \text{ \AA}$ ) and lifts them up. This is counteracted by a downward movement of the remaining undercoordinated Pd atom in the  $(2 \times 2)$  cell, leading to a modest first and (indirectly) second layer buckling of  $0.09 \text{ \AA}$  and  $0.10 \text{ \AA}$ , respectively. Overall this changes the slight compression of the clean surface  $d_{12}$  into a small expansion, but in total the first interlayer relaxation is still negligible.

Due to the lowered symmetry the relaxation pattern for the O  $(2 \times 1)$  structure, corresponding to 0.50 ML oxygen coverage, is a bit more complex, cf. Fig. 4.6 (left). An upward, sideward ( $0.06 \text{ \AA}$ ) movement of the twofold O-coordinated surface Pd atoms displaces the oxygen by  $0.05 \text{ \AA}$  from the ideal fcc site towards the top side. This goes hand in hand with a downward movement of the onefold O-coordinated Pd surface atoms, yielding a substantial  $0.16 \text{ \AA}$  first-layer buckling. The oxygen-induced increase of  $d_{12}$  found for the 1/4 ML phase continues

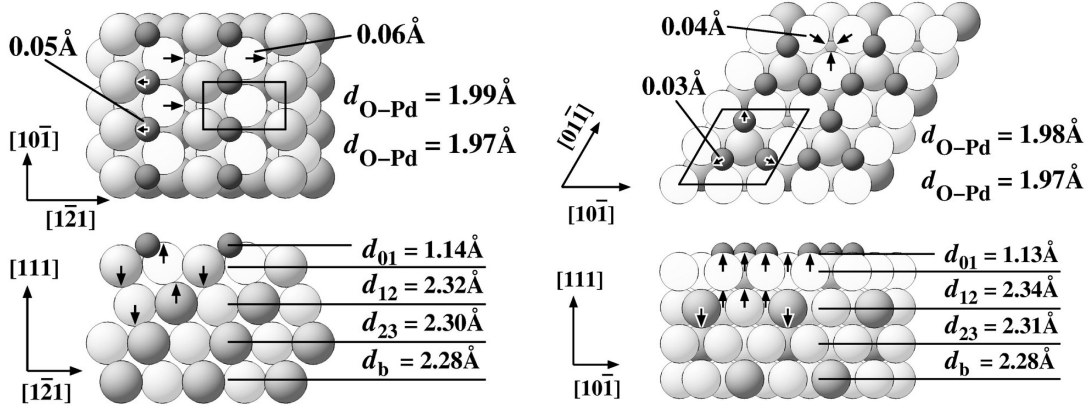


Figure 4.6: Top and side view of the atomic geometry of  $(2 \times 1)$ -O/Pd(111) to the left, and of  $3\text{O } (2 \times 2)$  to the right.

and results in a  $+2.0\%$  expansion with respect to the bulk value. The distance between second and third layer is also expanded ( $+0.9\%$ ). In addition the second layer is still quite buckled ( $0.10 \text{ \AA}$ ).

Further increase of the oxygen coverage to  $\theta = 0.75 \text{ ML}$  leads back to a threefold symmetry structure, the  $3\text{O } (2 \times 2)$ , shown in Fig. 4.6 (right). Here the buckling is less pronounced ( $0.09 \text{ \AA}$  and  $0.05 \text{ \AA}$  in first and second layer respectively), but the overall relaxation pattern is the same as before: oxygen is slightly pushed laterally away from the highest coordinated surface atoms, while the three Pd atoms, that are equivalent under the threefold symmetry have moved slightly ( $0.04 \text{ \AA}$ ) closer to each other. The first and second interlayer spacing is further expanded ( $+2.6\%$  and  $+1.3\%$ ). It comes therefore as a surprise that this layer relaxation trend is not continued, and even reversed, in the final  $\text{O}(1 \times 1)$  structure (where lateral displacements are not possible by symmetry). Whereas  $d_{23}$  is found to be expanded to now  $+1.8\%$ , the first interlayer distance suddenly exhibits a significant contraction of  $-1.7\%$ .

As a first step towards understanding this somewhat puzzling result and to ensure that it is not just an artefact of the calculation, the total-energy landscape for the  $\text{O}(1 \times 1)$  was mapped out as a function of the relaxation. For varying values of  $d_{12}$  and  $d_{23}$  the interlayer distances were kept fixed, while the oxygen layer was relaxed. The ensuing result shows a very shallow energy corrugation of only  $0.05 \text{ eV}$ . A local minimum, separated by a small energy barrier ( $0.02 \text{ eV}$ ) from the global minimum, seems to exist at about  $d_{12}=2.0\%$  and  $d_{23}=1.0\%$ . The global minimum is quite spreadout. Still, it lies in the same region as the reported first palladium layer contraction.

The question arises if this result is due to the adsorbed oxygen or a true feature of palladium. Performing the same study for the clean metal surface, i.e.

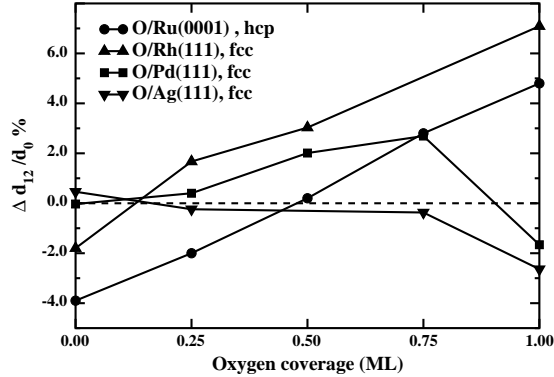


Figure 4.7: Calculated change in the mean outermost layer spacing relative to that of a bulk-terminated surface, as a function of oxygen coverage. The results for Ru(0001) and Rh(111) are taken from Refs. [35, 82]. The results for Ag(111) are from the already mentioned FP-LAPW calculations (cf. footnote 1)

determining the energy for different fixed values of  $d_{12}$  and  $d_{23}$ , show a fairly symmetric energy surface with just one minimum. It is, however, once again very shallow, indicating already that the observed contraction for the full monolayer oxygen coverage is largely due to the properties of palladium.

A comparison to the neighbouring  $4d$  elements may help to shed light into the relaxation behaviour of Pd. The results obtained within the FP-LAPW method are used once again, to exclude any additional uncertainties, possibly due to the use of pseudo-potentials in the studies on Ru(0001) [34] and Ag(111) [4]<sup>2</sup>. The calculated changes in mean interlayer distance  $d_{12}$  as a function of coverage, with oxygen each time in the most stable adsites (i.e. fcc on Rh, Pd, Ag; and hcp on Ru) are displayed in Fig 4.7 and show significant differences between the four metals. For the clean surfaces, the aforesaid strong contraction for Ru(0001) is lifted gradually from Rh(111) to Pd(111) and Ag(111). Furthermore, oxygen adsorption induces a strong increase of the outermost interlayer distance on Ru(0001) and Rh(111), that is almost linear with coverage. This is a reflection of the strong oxygen-metal bonds formed in these systems, weakening the remaining backbonding of the first-layer atoms to the underlying substrate. At Ag(111) on the other hand,  $d_{12}$  stays first more or less constant, and then even contracts at full ML coverage. This has likewise been attributed to the rather weak O-Ag

<sup>2</sup>Overall a very good agreement with the surface geometries described in the pseudopotential studies, was obtained for Ru(0001) and Ag(111). In particular, all oxygen-induced lateral displacements and buckling in the first two layers are found to be very similar for all four metals for all on-surface structures – both in magnitude and directions. Correspondingly, one can consider these details in the relaxation pattern to be a mere consequence of the specific adsorption geometry with O in the threefold hollow sites.



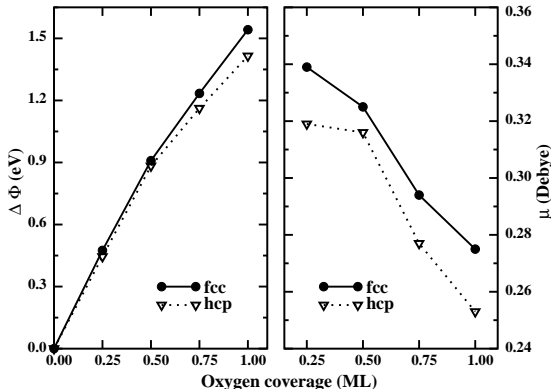


Figure 4.8: Calculated workfunction change (left) and dipole moment (right) for O on Pd(111) as a function of the oxygen coverage  $\theta$ , for the two most stable on-surface adsorption sites, i.e. fcc (filled circle) and hcp (empty triangle) hollow sites.

bonds that are no longer able to significantly disturb the metal surface geometry [4]<sup>3</sup>. Within this picture, O/Pd(111) appears as a borderline case. Initially, the O-Pd bond is still strong enough to induce a progressive expansion of the first interlayer distance with increasing O coverage, cf. Fig. 4.7. Yet, compared to Ru and Rh the bond strength is already so weak that this expansion is much less pronounced (smaller slope). And in the O(1 × 1) structure, the repulsive lateral interactions among the adsorbates have further weakened the O-Pd bond so much, that the outward relaxation can no longer be sustained and the surface prefers to contract, resembling in this aspect the Ag(111) surface. Of course, this tentative assignment glosses over many details, as e.g. reflected in the almost constant O-Pd bondlength of  $1.98 \pm 0.01 \text{ \AA}$  over the whole sub-monolayer coverage range, which resembles much more the values found on Ru(0001) and Rh(111), rather than the  $2.1 \text{ \AA}$  obtained for Ag.

#### 4.1.0.2 Electronic structure

Proceeding towards the electronic properties of the O/Pd(111) system, first the change in the workfunction  $\Delta\Phi(\theta)$ , relative to the clean surface, is considered as a function of oxygen coverage. For the clean surface the calculated workfunction

<sup>3</sup>It should be mentioned, however, that the character of the bonding on Pd and Ag is quite different. In Ag the bonding is governed largely by  $d-d$  repulsion and  $s$ -bonding. The Pd  $4d$ -band is almost completely full. The additional electron, when going from Pd to Ag can, therefore, go only partly into the  $d$ -band, and then at its antibonding end. For a more than half-full  $d$ -band, each additional  $d$ -electron, reduces the inward relaxation of the localised  $d$ -bonds. The increase  $sp$ -charge (for Ag), increases the inward relaxation effect of the Smoluchowski smoothing [83]. Therefore, Ag-Ag attraction is due to the  $s$ -electrons, while the O-Ag bonding is probably due mostly to  $4d$ -electrons.

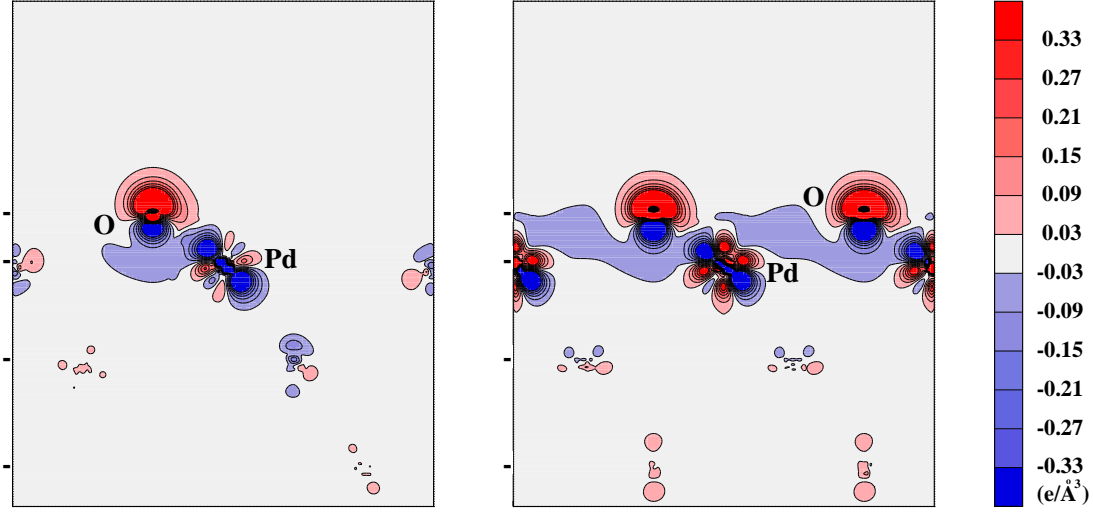


Figure 4.9: Difference electron density plot for 0.25 ML (left) and 1.00 ML (right) oxygen adsorbed on Pd(111) in fcc-hollow site. The contour plot depicts the  $[\bar{2}11]$  plane perpendicular to the (111) surface. Areas of electron accumulation and depletion have positive and negative signs respectively, contour lines are drawn at  $0.06 e/\text{\AA}^3$ . The small black lines to the left of each picture show the approximate position of the respective atom layers, i.e. one oxygen and three palladium layers.

is 5.25 eV (see chapter 3.2). As shown in Fig. 4.8 (left),  $\Delta\Phi(\theta)$  rises almost linearly with coverage for both hollow adsorption sites, but is slightly larger for the fcc site. Both curves exhibit a typical curvature reflecting a depolarisation with increasing coverage. To the right in Fig. 4.8 the adsorbate-induced dipole moment is shown, for which the depolarisation is also visible - it decreases by about 20% from a quarter to full monolayer coverage.

The adsorbate dipole moment is a direct consequence of the adsorbate-induced electron density redistribution, which is shown in Fig. 4.9. The difference electron density is determined by subtracting from the electron density of the chemisorbed system,  $n^\Delta(\mathbf{r})$ , both that of the clean Pd(111) surface ( $n^{sub}(\mathbf{r})$ ), and that of the isolated adsorbate layer ( $n^{ad}(\mathbf{r})$ ), the interatomic distances of the latter two corresponding exactly to those the adsorbate system [92]:

$$n^\Delta(\mathbf{r}) = n(\mathbf{r}) - n^{sub}(\mathbf{r}) - n^{ad}(\mathbf{r}). \quad (4.2)$$

A difference electron density analysis might also allow the identification of orbitals involved in the interactions between adsorbate and substrate, hence, it yields a microscopic understanding of the binding mechanism.

The difference electron density plot for the O(2x2) (Fig. 4.9 (left)) and O(1x1) (Fig. 4.9 (right)) structures, with O adsorbed in the fcc hollow site, depict a plane perpendicular to the surface. Obviously for the 0.25 ML case (left), the

perturbation of the surface due to the oxygen atom is localised mostly on the oxygen atom itself and on its nearest neighbour Pd atom. For oxygen adsorbed in the hcp site, the result is essentially the same, rendering the small difference found between the O binding energy of these two sites comprehensible. The symmetry of the orbitals involved in the bonding suggests that it (the bonding) occurs through a hybridisation of the  $2p$ -orbitals of the oxygen and the palladium  $4d_{xz}/4d_{yz}$  states. Furthermore, the electron density of the oxygen atom is quite polarised, and enhanced on the vacuum side. The palladium orbitals pointing towards the oxygen are depleted, while the ones pointing away from it, have an enhanced electron density. The resulting (inward pointing) surface dipole moment may be quantified via the Helmholtz equation [93, 94, 95]

$$\mu = (1/12\pi)A \Delta\Phi/\theta, \quad (4.3)$$

where  $A$  is the area per  $(1 \times 1)$  surface unit cell (in  $\text{\AA}^2$ ). The induced work function change,  $\Delta\Phi(\theta) = \Phi(\theta) - \Phi^{\text{clean}}$  is given in eV and the coverage  $\theta$  in ML. Then the dipole moment is measured in Debye.

$\theta$	0.25	0.50	0.75	1.00
$\Phi$ (eV)	5.74	6.17	6.50	6.79
$\mu$ (Debye)	0.34	0.33	0.29	0.28

Table 4.3: Change in the workfunction and dipole moment for O in fcc hollow on Pd(111) with coverage.

Comparing the difference electron density pictures for the O  $(2 \times 2)$  and the O  $(1 \times 1)$  structures, it is noticeable that the electron density distribution for the full monolayer case is rather delocalised. This is reflected in the decrease of the surface dipole moment  $\mu$  with increasing oxygen coverage (cf. Fig. 4.8).

The adsorbate-adsorbate interactions, obviously, also affect the density of states (DOS). The DOS for the clean Pd(111) surface, the 1/4 ML and 1 ML O/Pd(111) structures with O in fcc sites is shown in Fig. 4.10. Comparing the DOS of the clean surface with the DOS of either adsorbate structures (cf. Fig. 4.10 (a)), reveals the O-Pd bonding and antibonding states. They are seen even better in the difference DOS<sup>4</sup>, Fig. 4.10 (b), and are located just below and just above the nearly fully occupied palladium  $d$ -band. The bonding states are around 5-8 eV below the Fermi-level and the antibonding states around and just above the Fermi level.

An appreciable splitting is seen in the O-Pd bonding peaks at the lower end of the

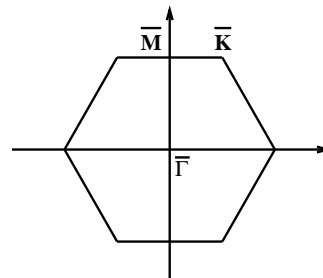


Figure 4.11: Surface Brillouin zone.

<sup>4</sup>The difference DOS shows the adsorbate induced change, i.e.  $\Delta N = N_{\text{O@M}} - N_{\text{M}}$  [92].

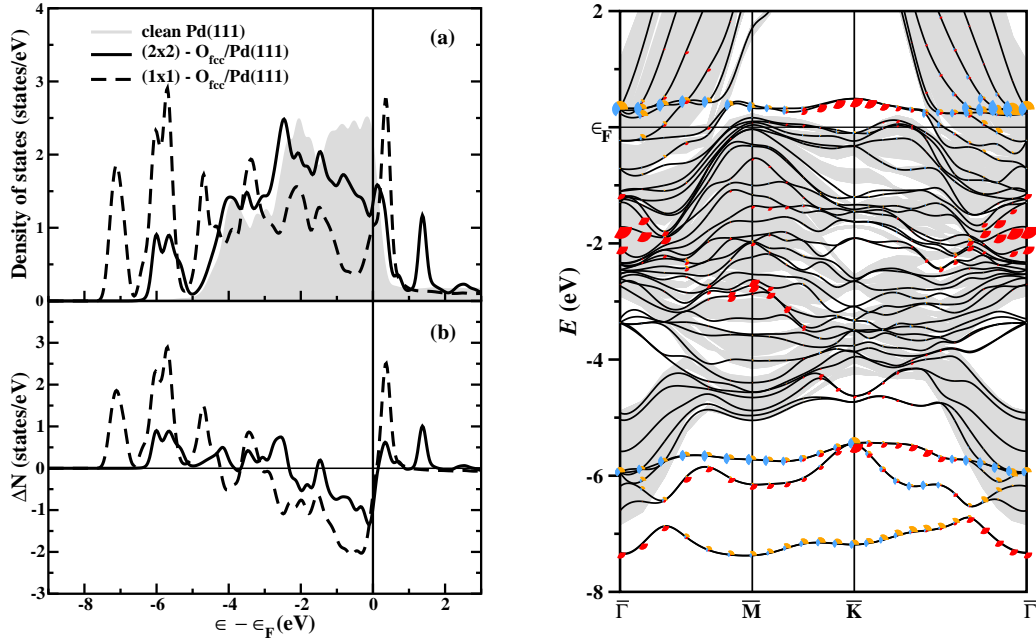


Figure 4.10: Left (a): Calculated total density of states (DOS) for a one-fold coordinated surface Pd atom in the (2x2)-O/Pd(111) system (solid line) and a threefold O-coordinated Pd atom in the (1x1)-O/Pd(111) structure (dashed line). The DOS of the top layer Pd atom of the clean surface is shown as a grey area. Left (b): Corresponding difference of the DOS. Right: Surface band structure of O (1x1)/Pd(111) (solid lines). The grey area corresponds to the projected Pd bulk band structure, and the circle segments reflect the oxygen  $p$ -orbital character of the bands:  $p_x$  (orange),  $p_y$  (blue) and  $p_z$  (red). The radius scale with the projection onto the corresponding spherical harmonics within the oxygen muffin-tin spheres.

$d$ -band for the full monolayer – 4 peaks are clearly discernable. At this coverage the formation of an adsorbate band structure is expected [92], shown to the right in Fig. 4.10. The three lower peaks (-7.2 eV to -5.8 eV) are clearly due to the bonding states of the O  $2p$  orbitals (the antibonding states are seen just above the Fermi energy in the surface bandstructure plot). The peak around -4.7 eV has mainly  $d$  character and can be traced back to a state which splits off the bulk  $d$ -band at the  $\bar{K}$  point (cf. Fig. 4.11).

It is again instructive to compare these findings with the detailed results available for O at the other late  $4d$  TMs [4, 34, 35]. Concerning the DOS the obvious difference between Ru, Rh, Pd and Ag is the progressively higher lying Fermi-level in the  $4d$ -band, yielding an about half-filled band in Ru and a fully occupied band in Ag. Since the O-metal interactions give rise to bonding and antibonding states located at the lower and upper edge of the  $4d$ -band, the filling of the  $d$ -band towards the right of the periodic table populates the antibonding states. As already mentioned in section 5.5, the consequence is a substantially weakened

oxygen bond strength, decreasing roughly by 1 eV for each element towards the right within this late  $4d$  series. Despite this appreciable change in the energetics, the nature of the O-metal bond as arising primarily from the interaction with the  $4d$ -states does not change, and correspondingly difference electron density plots e.g. as published for the O( $2 \times 2$ ) phase on Ru(0001) [34], on Rh(111) [35], on Pd(111), cf. Fig. 4.9, and Ag(111) [4] are exceedingly alike.

Concerning the workfunction a similar increase with oxygen coverage has been reported for Ru(0001), Rh(111) and Ag(111). On the prior two surfaces, even the absolute magnitude of the rise is very similar to the one found for Pd(111). At least for coverages up to  $3/4$  ML, as both Ru and Rh exhibit a saturation of  $\Delta\Phi$  for the O( $1 \times 1$ ) structure, i.e. the value of the workfunction remains almost constant for  $0.75 \text{ ML} < \theta \leq 1.00 \text{ ML}$ . Pd(111) does not show such a saturation and is in this respect more similar to Ag(111), for which a monotonic increase up to the full monolayer was computed. However, this rise is more than twice as large compared to the one at the basal plane of Ru, Rh and Pd. This trend is consistent with the observation that the difference in electronegativity between O and Ru, Rh and Pd seems to be almost constant, while it is slightly higher for Ag [96]. Similar to the conclusion obtained from the surface relaxations, Pd appears therefore as a borderline case in this late  $4d$  series, which shows high similarities to its lefthand neighbours for lower O coverages, but switches at the full oxygen ML coverage to resemble more Ag.



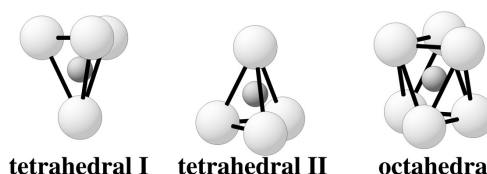
## Chapter 5

# Oxygen incorporation into the Pd(111) surface

Proceeding with the investigation of the oxygen-palladium system, this chapter addresses the issue of oxygen incorporation into the (111) surface of this transition metal. The initial penetration of oxygen into the region between first and second substrate layer will be studied, as well as the implications this has for oxide formation. Furthermore, the question about the amount of oxygen that can be solved in the bulk will be investigated.

To study the penetration of O into the Pd(111) surface, one has to look at the several available sub-surface sites. There are three high-symmetry interstitial sites, that have to be taken into account: one octahedral site with sixfold Pd

coordination (henceforth referred to as octa) and two tetrahedral sites with fourfold Pd coordination (henceforth referred to as tetra-I and tetra-II). The octa and the tetra-I sites are located directly below the on-surface fcc and hcp sites, respectively, whereas the tetra-II



II site is found below a surface Pd atom, as sketched in Fig. 5.1. (In a bulk material one would have to consider only an "octa" and one "tetra" site - there

would be no distinction between "tetra-I" and "tetra-II". Close to the surface the sites have a reduced symmetry (only  $C_{3V}$  symmetry), making such a differentiation necessary.) The same sites are also present at the (0001) surface of an hcp metal (i.e. Ru).

Each of the three sub-surface sites was considered for the oxygen adsorption on palladium along with the available on-surface sites. However, for each considered coverage, adsorption in a sub-surface site alone was energetically always less favourable than adsorption in a threefold-hollow site. In most cases pure

Sub-surface sites	Coverage $\theta$			
	0.25 ML	0.50 ML	0.75 ML	1.00 ML
tetra-I	-0.37	-0.22	-0.13	-0.44
tetra-II	-0.58	-0.34	-0.05	0.10
octa	-0.78	-0.44	-0.34	-0.38

Table 5.1: Binding energies (in eV/atom) for O adsorbed in one of the available high-symmetry sub-surface sites on Pd(111), relative to the dissociation energy of the oxygen molecule.

sub-surface adsorption is even endothermic, cf. Table 5.1.

It was seen in the preceding chapter, that the binding energy for on-surface adsorption, decreases progressively not only throughout the sequence of elements, in which the  $4d$ -states are successively filled, but increasing oxygen coverage causes a decline as well. In the case of palladium the full monolayer coverage came out just exothermic, whereas for silver, coverages beyond  $1/2$  ML were already endothermic. In this regard, one has to consider that oxygen may start penetrating into the Pd(111) surface even before a full monolayer is adsorbed on it.

## 5.1 Thermodynamic model

The coverage, at which oxygen incorporation into the surface should begin, can be estimated with the help of a thermodynamic equilibrium model proposed by King and coworkers [97], already from the data available for the on-surface adsorption. The model assumes that the critical coverage,  $\theta_c^{\text{thd}}$ , at which the transition between a chemisorbed phase and the appearance of an oxidic film occurs is thermodynamically, not kinetically, determined, meaning that below  $\theta_c^{\text{thd}}$  the heat of adsorption of the chemisorbed phase is higher than the heat of formation of the oxide. This reasoning has been applied successfully to explain experimental data on the critical coverage for oxide formation on Ni(100) and Ag(111) [97].

The binding energy,  $E_b$ , of oxygen adsorbed on any of the so far discussed transition metals, decreases with coverage (cf. Fig. 4.3). This allows to approximate the integral heat of adsorption as  $\Delta H_{\text{ad}}(\theta) \approx E_b(\theta) \cdot \theta$ . Then, the above statement translates as follows: Repulsive interactions between the O adatoms drive the differential heat of adsorption,  $\partial(\Delta H_{\text{ad}})/\partial\theta$ , down sharply with increasing coverage, until at  $\theta_c^{\text{thd}}$  it is equal to the heat of formation of an oxide,

$$[\partial(\Delta H_{\text{ad}})/\partial\theta]_{\theta_c^{\text{thd}}} = \Delta H_f^{\text{oxide}} . \quad (5.1)$$

To evaluate the differential heat of adsorption,

$$\frac{\partial}{\partial\theta} \Delta H_{\text{ad}}(\theta) \approx \frac{\partial}{\partial\theta} [E_b(\theta) \cdot \theta] = E_b(\theta) + \theta \cdot \frac{\partial E_b}{\partial\theta} , \quad (5.2)$$



the computed values for  $E_b$  and their change with coverage,  $\partial E_b/\partial\theta$ , are needed. The later are easily obtained from the slope of the calculated binding energy curves,  $E_b(\theta)$ , which are roughly linear with coverage (cf. Fig. (4.3)):

$$E_b(\theta) \approx E_b(0.25 \text{ ML}) + (\theta - 0.25 \text{ ML}) \frac{\partial E_b}{\partial\theta}, \quad (5.3)$$

The heat of formation,  $\Delta H_f^{\text{oxide}}$ , of the most stable bulk oxide phase for each of the considered metals is:  $\Delta H_f(\text{RuO}_2) = 3.4 \text{ eV}$  [89],  $\Delta H_f(\text{Rh}_2\text{O}_3) = 3.8 \text{ eV}$  [98],  $\Delta H_f(\text{PdO}) = 0.9 \text{ eV}$  [99] and  $\Delta H_f(\text{Ag}_2\text{O}) = 0.2 \text{ eV}$  [100], available from DFT calculations<sup>1</sup>. After solving eq. (5.1) for the critical coverage,

$$\theta_c^{\text{thd}} = \frac{\Delta H_f^{\text{oxide}} - E_b(0.25 \text{ ML}) + 0.25 \text{ ML} \cdot \frac{dE_b}{d\theta}}{2 \frac{dE_b}{d\theta}}, \quad (5.4)$$

one obtains the values listed in Table 5.2 for the coverage at which the transition to an oxide should occur. Therefore, within this model, it is expected that the

	Ru	Rh	Pd	Ag
$\theta_c^{\text{thd}}$ [ML]	0.84	0.56	0.32	0.23

Table 5.2: Calculated critical thermodynamic coverage (in ML),  $\theta_c^{\text{thd}}$ , for the oxide formation on the late  $4d$  transition metals.

oxide phase will become more stable only after almost a full ML of oxygen is adsorbed on the Ru surface. This value decreases sequentially for Rh and Pd, until it is less than a quarter of a ML for Ag.

## 5.2 Initial oxygen incorporation

The thermodynamic model gives the coverage relevant for oxide formation, but does not account for the *microscopic processes* underlying the phase transition from an adsorbate layer to an oxide<sup>2</sup>. Trying to supplement the thermodynamic result with microscopic information, the incorporation of the first O atom into the sub-surface region of Pd(111), which initiates the oxide formation, is addressed in the following.

Occupation of sub-surface sites will commence when a structure containing oxygen in sub-surface sites becomes energetically more stable than its counterpart with the same total oxygen coverage,  $\theta_{\text{tot}}$ , but with O adsorbed just on the

<sup>1</sup>To determine  $\theta_c^{\text{thd}}$  the heat of formation of the oxide is needed per oxygen atom, i.e.,  $\Delta H_f(\text{RuO}_2) = 1.7 \text{ eV}/(\text{O atom})$ ,  $\Delta H_f(\text{Rh}_2\text{O}_3) = 1.3 \text{ eV}/(\text{O atom})$ ,  $\Delta H_f(\text{PdO}) = 0.9 \text{ eV}/(\text{O atom})$  and  $\Delta H_f(\text{Ag}_2\text{O}) = 0.2 \text{ eV}/(\text{O atom})$ .

<sup>2</sup>Here and in the following the term "oxide" does not necessarily have to mean three-dimensional bulk oxide. While the oxide phase observed on Ru(0001) is RuO<sub>2</sub>(110) [1], Pd and Ag show an affinity towards the formation of surface oxides [3, 101, 102]. Surface oxides will be discussed in the following chapters.

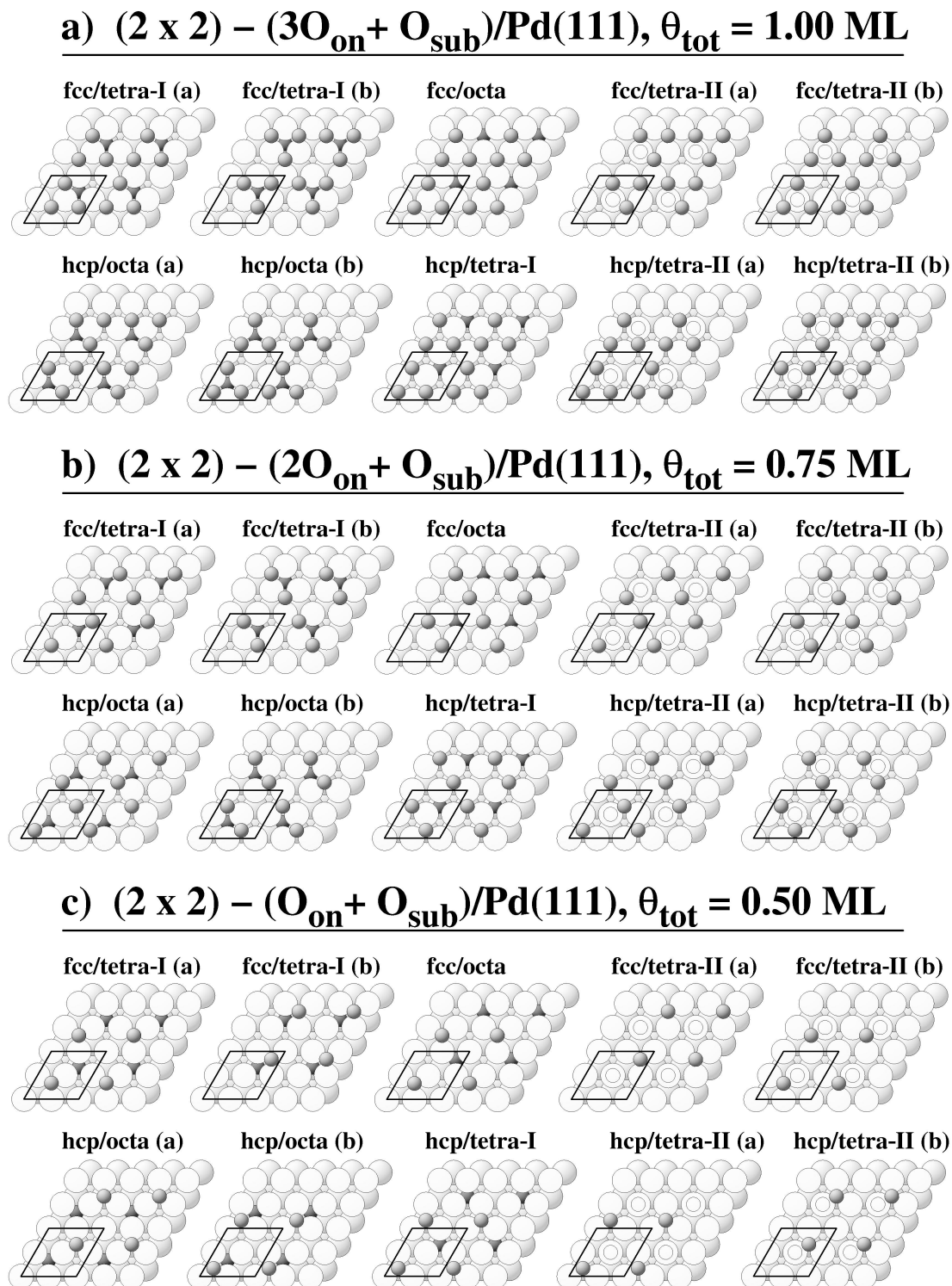


Figure 5.2: Top view of all possible on-surface/sub-surface site combinations for total coverages: a)  $\theta_{\text{tot}} = 1 \text{ ML}$ , b)  $\theta_{\text{tot}} = 0.75 \text{ ML}$ , c)  $\theta_{\text{tot}} = 0.50 \text{ ML}$ . Inequivalent geometries with the same site occupation are denoted with (a) and (b), the (a)-geometries being the more stable ones. Big spheres correspond to palladium atoms (white = surface layer, light grey = second layer). O atoms = small spheres (gray = on-surface, black = sub-surface). Sub-surface oxygen atoms in tetra-II sites are invisible in this representation and are shown schematically as small white circles.

surface. This implies that the stability and properties of structures, containing both on-surface and sub-surface oxygen, at coverages up to one monolayer,  $0 < \theta_{tot} \leq 1$  ML, have to be studied.

Such a study was carried out employing  $(2 \times 2)$  cells. The limitation to relatively small cells does, of course, not allow to pinpoint the exact coverage, at which the first oxygen atom will penetrate into the surface. Still, one will hardly be able to determine the exact coverage, even if *much* bigger cells were used, which is not really feasible. Besides, even the use of  $(3 \times 3)$  cells does not seem reasonable, provided that one is able to obtain the needed information from a  $(2 \times 2)$  cell calculation. Already such a calculation makes it possible to define a coverage range, in which the oxygen penetration into the surface will start. Therefore, one can hope to perform a trend study concerning the initial oxygen incorporation into the basal surface of each of the  $4d$  transition metals, considered in the preceding, even by using "just"  $(2 \times 2)$  cells.

The use of  $(2 \times 2)$  unit cells means that the average binding energy of fully relaxed geometries containing from  $N_{tot} = 1$  ( $\theta_{tot} = 0.25$ ML) to  $N_{tot} = 4$  ( $\theta_{tot} = 1.00$ ML) oxygen atoms is calculated. Of this  $N_{tot}$  oxygen atoms,  $0 \leq N_{sub} \leq N_{tot}$  can be located below the surface. Considering that there are two threefold hollow sites available for surface adsorption and three high-symmetry interstitial sites between the first and the second metal layer, a vast host of possible combinations has to be taken into account. In particular, one has to be aware, that in cases of mixed occupation several symmetry inequivalent structures, for the same combination of on-surface and sub-surface sites, may exist. Since for every given  $(\theta_{tot}, N_{sub}/N_{tot})$ , structures with site occupation of  $(N_{tot} - N_{sub})$  on-surface O in either fcc or hcp, and  $N_{sub}$  O atoms in either of the three sub-surface sites, have to be tested, this may result in as many as 12 trial geometries per coverage.

To investigate the incorporation of the first atom into the surface, one has to look at structures with  $N_{sub} = 1$ . All such structures with mixed on-surface/sub-surface site occupation, which are possible at the different considered coverages  $(\theta_{tot} = 1.00$ ML,  $N_{sub}/N_{tot} = 1/3)$ ,  $(\theta_{tot} = 0.75$ ML,  $N_{sub}/N_{tot} = 1/2)$ ,  $(\theta_{tot} = 0.50$ ML,  $N_{sub}/N_{tot} = 1/1)$ , are shown in Fig. 5.2. Two symmetry inequivalent geometries exist for each case. For two of them, namely fcc/octa and hcp/tetra-I, one site combination can be, however, excluded from the beginning, since in it one on-surface and one sub-surface oxygen atom sit directly above each other (not shown). Due to the strong repulsion arising between the electronegative oxygens when they get close to each other (as seen in the previous chapter), it is clear from the start, that these two geometries will be unfavourable.

Starting with  $(\theta_{tot} = 1.00$ ML,  $N_{sub}/N_{tot} = 1/3)$ , all structures shown in Fig. 5.2 were relaxed using a coarse basis set<sup>3</sup>. The calculated binding energies are dis-

---

<sup>3</sup>The parameters which differ from the ones used for the converged calculations are the following: The energy cutoff for the plane wave representation of the wave function in the interstitial region between the muffin tin spheres was  $E_{wf}^{max} = 15$ Ry. A  $(4 \times 4 \times 1)$  Mohnkhorst-Pack grid with 4(7) irreducible  $\mathbf{k}$  points, depending on symmetry, was used for the Brillouin

Sites on-/sub-surface	Coverage $\theta$		
	0.50 ML	0.75 ML	1.00 ML
fcc/tetra-I (a)	1.09	0.73	0.26
fcc/tetra-I (b)	0.09	-0.11	-0.24
fcc/octa	0.19	0.15	0.00
fcc/tetra-II (a)	0.18	0.26	0.01
fcc/tetra-II (b)	-	-0.12	-0.01
hcp/octa (a)	0.78	0.58	-0.05
hcp/octa (b)	-	-	-0.57
hcp/tetra-I	-	-	-0.16
hcp/tetra-II (a)	-	-	-0.06
hcp/tetra-II (b)	-	-	-0.07

Table 5.3: Binding energies (in eV/atom) for O, adsorbed in one of the available high-symmetry sub-surface sites on Pd(111), relative to the dissociation energy of the oxygen molecule. The energy cutoff for the wavefunctions in the interstitial region was  $E_{max}^{wf} = 15$  Ry. For  $\theta = 0.75$  ML and  $\theta = 1.00$  ML a  $(4 \times 4 \times 1)$  Monkhorst-Pack (MP) grid with  $k_{ir} = 4$ ,  $k_{ir} = 7$  or  $k_{ir} = 13$ , in the irreducible part of the Brillouin zone, depending on symmetry and coverage. For  $\theta = 0.50$  ML a  $(6 \times 6 \times 1)$  MP grid, with  $k_{ir} = 7$  or  $k_{ir} = 13$ , (depending on symmetry) was used.

played in Table 5.3.

The prerogative was to get a feeling which structures may be relevant for further consideration. Since the use of a coarser basis set, does not influence the sequence of the different geometries with respect to their stability, but merely introduces a bigger absolute error into the calculated binding energies, such a procedure is legitimate. Analysing the obtained energies reveals, that for each pair of symmetry inequivalent site combinations, the one, in which a greater number of oxygen atoms are located as far away from each other (within the  $(2 \times 2)$  unit cell) as possible, is always the more stable one, which is another manifestation of the repulsive oxygen-oxygen interactions. Furthermore, cases, in which the on-surface oxygen atoms are adsorbed in an fcc place (this was the most stable adsorption site for pure on-surface adsorption), are favoured over the ones with oxygen atoms in hcp position. Most probably the coupling to the substrate plays also a role, since in most geometries the tetrahedral sites seem to be favoured over the octahedral site. The gained knowledge allows for a less thorough testing of the lower coverage cases. For  $\theta_{tot} = 0.75$  ML all the fcc/sub-surface oxygen atoms combinations, as well as the hcp/octa (as the most stable site combination, of the hcp/sub-surface group) structure were relaxed with the coarser basis set<sup>4</sup>.

---

zone integration.

<sup>4</sup>Here a  $(4 \times 4 \times 1)$  MP-grid corresponds to  $k_{ir} = 7$  or  $k_{ir} = 13$ , depending on symmetry.

Sites on-/sub-surface	$\theta_{tot}$			
	0.25 ML	0.50 ML	0.75 ML	1.00 ML
fcc/-	1.47	1.12	0.76	0.38
fcc/tetra-I	-	1.04	0.84	0.49
-/tetra-I	-0.37	-0.22	-0.13	-0.04

Table 5.4: Binding energies (in eV/atom) change with coverage for the most stable geometry with mixed O site occupation, i.e. fcc/tetra-I (a), on Pd(111), relative to the dissociation energy of the oxygen molecule. For convenience, the binding energies for adsorption in fcc (Table 4.1) and tetra-I (Table 5.1) position are also shown.

The same is also true for  $\theta_{tot} = 0.50 \text{ ML}$ <sup>5</sup>. All the geometries with mixed site occupation that were considered, are summarised in Table 5.3.

Each time the fcc/tetra-I (a) combination was the energetically preferred one and was consequently relaxed with the converged basis set. The resulting binding energies are listed in Table 5.4. For convenience, the binding energies for adsorption in fcc and tetra-I positions are shown, as well. Thus it is easy to detect, that at a total coverage of  $\theta_{tot} = 0.75 \text{ ML}$  and  $\theta_{tot} = 1.00 \text{ ML}$  the fcc/tetra-I (a) site combination is more stable than pure on-surface adsorption. At  $1/2 \text{ ML}$  coverage the on-surface adsorption site remains the preferred one, which means that incorporation of oxygen into the surface will start at some point after the Pd(111) surface is covered by half a monolayer O, but before a  $3/4 \text{ ML}$  coverage is reached.

### 5.3 The mixed $O_{\text{fcc}}/O_{\text{tetra-I}}$ structures

In the following, the main structural and electronic properties of the stable fcc/tetra-I site combination, i.e., at  $\theta_{tot} = 1 \text{ ML}$  and  $\theta_{tot} = 0.75 \text{ ML}$  are described in more detail.

The two relaxed structures  $(2 \times 2) - (3O_{\text{fcc}} + O_{\text{tetra-I}})/\text{Pd}(111)$  and  $(2 \times 2) - (2O_{\text{fcc}} + O_{\text{tetra-I}})/\text{Pd}(111)$  are shown in Fig. 5.3. Each of them has, apart from inversion symmetry, a mirror plane along the longer diagonal of the unit cell, but no rotation axes are found. Due to the additional presence of sub-surface oxygen, which reduces symmetry, these geometries exhibit a much more complex relaxation pattern compared to the afore discussed pure on-surface chemisorption cases, cf. chapter 4. A number of similarities in the relaxation behaviour of different atoms in the two structures are detected. The three first layer palladium atoms in the vicinity of the sub-surface oxygen move sideways away from it and are lifted up, increasing the volume, which the sub-surface O has at its disposal. The fourth palladium atom is pushed away and downward, as the on-surface

<sup>5</sup>Here a  $(6 \times 6 \times 1)$  MP-grid corresponds to  $k_{ir} = 7$  or  $k_{ir} = 13$ , depending on symmetry. The fcc/tetra-II (b) case was not considered.

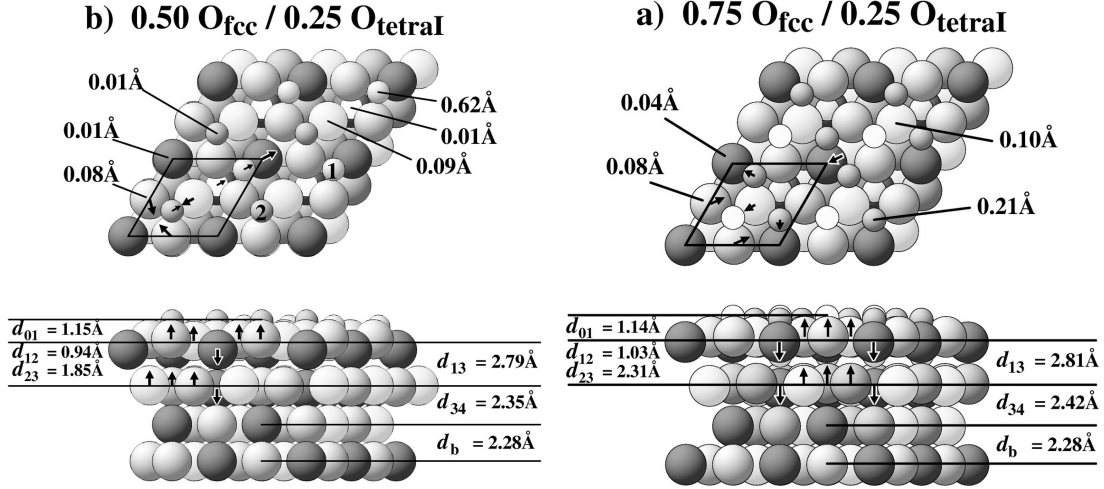


Figure 5.3: Top and side view of the atomic geometries (a)  $(3\text{O}_{\text{fcc}} + \text{O}_{\text{tetra-I}})/\text{Pd}(111)$  and (b)  $(2\text{O}_{\text{fcc}} + \text{O}_{\text{tetra-I}})/\text{Pd}(111)$ . The small circles represent the oxygen atoms. The large circles represent the palladium atoms, where those lying in the same plane and equivalent with respect to the mirror symmetry have the same colour. The arrows (not drawn to scale) indicate the direction of the displacements of the substrate atoms from their ideal (bulk-like) positions.

oxygen atom(s) in the immediate neighbourhood of the sub-surface oxygen, try to increase their distance to it, moving towards an on-top position. The slight change in the position of the second on-surface oxygen atom, seems therefore to be rather a consequence of the displacement of the surrounding palladium atoms. The vertical relaxations for the  $(0.75\text{O}_{\text{fcc}}/0.25\text{O}_{\text{tetra-I}})/\text{Pd}(111)$  system are as follows: the distance between the first two palladium layers is increased by 23% ( $d_{13} = 2.81\text{Å}$ ),<sup>6</sup> with a buckling of  $\Delta z_1 = 0.28\text{Å}$  for the first and  $\Delta z_2 = 0.36\text{Å}$  for the second layer. The expansion between second and third layer is  $d_{34} = 2.42\text{Å}$  (6%). The buckling of the first and second palladium layers of the  $(0.50\text{O}_{\text{fcc}}/0.25\text{O}_{\text{tetra-I}})/\text{Pd}(111)$  geometry is  $\Delta z_1 = 0.28\text{Å}$  and  $\Delta z_2 = 0.36\text{Å}$ , respectively, and thus identical to the values determined for the higher coverage case. Still, the reduced on-surface O coverage is reflected in the slightly smaller expansion between the palladium layers. For the distance between the first and the second layer  $d_{13} = 2.79\text{Å}$  (22%) is calculated, while  $d_{34} = 2.35\text{Å}$  (3%). It is interesting to notice, that the O-Pd bondlength, listed for the  $(2 \times 2) - (2\text{O}_{\text{fcc}} + \text{O}_{\text{tetra-I}})/\text{Pd}(111)$  geometry in Table 5.5, remains relatively constant for both structures, assuming values between  $1.9\text{Å}$  and  $2\text{Å}$ . The numbers found for

<sup>6</sup>The center of mass of each layer is used to calculate the distance between them. The nomenclature is as follows (cf. Fig. 5.3):  $d_{01}$  - distance between the on-surface oxygen layer and the first Pd layer;  $d_{12}$  and  $d_{23}$  are the distances between the sub-surface oxygen layer and the first, respectively second, palladium layers;  $d_{13}$ ,  $d_{34}$  are the interlayer distances between first and second, and second and third palladium layers, respectively.

	Pd <sub>2</sub>	Pd <sub>1</sub> (dark)	Pd <sub>1</sub> (light)	Pd <sub>1</sub>
O <sub>sub</sub>	1.99	-	1.95	2.00
O <sub>1</sub>	-	1.97	-	2.05
O <sub>2</sub>	-	-	1.98	1.93

Table 5.5: Bondlength (in Å) between O and Pd in the  $(2 \times 2) - (2O_{\text{fcc}} + O_{\text{tetra-I}})/\text{Pd}(111)$  structure. Notation is as follows: Pd<sub>2</sub> is the palladium atom of the second layer, located directly below the sub-surface oxygen atom and Pd<sub>1</sub> stands for the Pd atoms of the 1st layer. The indications in the brackets and the indices of the oxygen atoms refer to Fig. 5.3.

pure on-surface chemisorption were in the same range.

It is furthermore instructive to compare the coverage dependence of the workfunction for the situation of mixed on-/sub-surface site occupation, to the case of pure on-surface chemisorption. To this end, the change in workfunction upon increasing oxygen coverage relative to the clean surface is shown in Fig. 5.4. Incorporation of oxygen into the sub-surface region, lowers the workfunction. The shift remains almost constant,  $\approx 0.2$  eV, for all the mixed fcc/tetra-I structures,

cf. Table 5.4. The decline of  $\Phi$  is the consequence of a competition arising between sub-surface and on-surface oxygen for the bonding charge of the surface Pd atoms. This makes the on-surface O species slightly less negatively charged (seen by a comparison of the initial state shift of the O2s core-levels), compared to a situation with no sub-surface oxygen involved. One can further see, that the slope of the workfunction rise remains the same as  $\theta_{\text{tot}}$  increases, regardless if one considers just on-surface or just mixed site occupation. This reflects the depolarisation with increasing coverage.

It was argued in the preceding chapter, that the reduction of the inward pointing dipole moment due to an enhanced density at the surface oxygen atom with coverage, is a consequence of the growing repulsive interactions within a more and more densely packed overlayer. It is therefore expected, that the presence of an oxygen atom below the surface, will further reduce the dipole. This is demonstrated by the dramatic

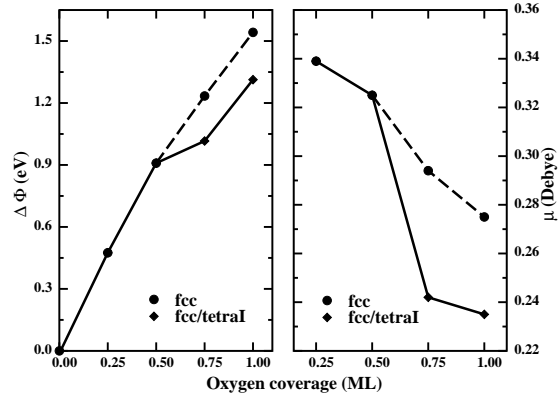


Figure 5.4: Dependence of the calculated workfunction (left) and dipole moment (right) on the oxygen coverage  $\theta$  for the most stable geometry at each considered coverage. At  $\theta_{\text{tot}} = 0.75$  ML and  $\theta_{\text{tot}} = 1$  ML both fcc and the fcc/tetra-I combinations are shown.

$\theta$	0.25	0.50	0.75	1.00
$\Phi$ (eV)	-	5.99	6.28	6.57
$\mu$ (Debye)	-	0.26	0.24	0.24
$\Delta\Phi(\text{O}_{\text{fcc}})$ (eV)	0.49	0.92	1.25	1.54
$\Delta\Phi(\text{O}_{\text{fcc}}/\text{O}_{\text{tetra-I}})$ (eV)	-	0.71	1.03	1.33

Table 5.6: Change in the workfunction,  $\Phi$ , and dipole moment,  $\mu$ , of the  $((\theta - \theta_{\text{sub}}) \text{O}_{\text{fcc}}/0.25 \text{O}_{\text{tetra-I}})$  geometry with O coverage. The change of the workfunction with respect to the clean Pd(111) surface is listed for pure on-surface chemisorption (O in fcc hollow) and mixed fcc/tetra-I adsorption, as well.

change of  $\mu$  as the  $(0.50 \text{O}_{\text{fcc}}/0.25 \text{O}_{\text{tetra-I}})$  structure becomes more stable than the  $(2 \times 2) - 3 \text{O}_{\text{fcc}}/\text{Pd}(111)$  structure.

To gain insight into the bonding mechanism of the  $\text{O}_{\text{fcc}}/\text{O}_{\text{tetra-I}}$  structures, it is helpful to take a look at the difference electron density of the  $(2 \times 2) - (2 \text{O}_{\text{fcc}} + \text{O}_{\text{tetra-I}})/\text{Pd}(111)$  geometry, shown in Fig. 5.5 (left). A strong depletion of the  $4d_{xz,yz}$  states of the surface palladium atom(s) bonded to both  $\text{O}_{\text{fcc}}$  and  $\text{O}_{\text{tetra-I}}$  occurs, while the electron density at the oxygen atoms is increased. It seems likely, that the linear  $\text{O}_{\text{fcc}} - \text{Pd} - \text{O}_{\text{tetra-I}}$  coordination allow the strong hybridisation of the Pd  $4d_{xz,yz}$  orbital with the  $\text{O}_{\text{fcc}}$  and  $\text{O}_{\text{tetra-I}}$  species, and also screens the electrostatic interactions between them. A reason for the move of the on-surface O atom (marked as 1 in Fig. 5.3) towards an on-top position (with respect to the first layer palladium atom) might be, that the repulsive interactions between this atom and the sub-surface oxygen are not screened. However, it is equally possible that this lateral displacement is due to purely geometric reasons and is caused by the strong upward relaxation of the three palladium atoms surrounding the sub-surface oxygen. The same arguments can be applied to the  $(2 \times 2) - (3 \text{O}_{\text{fcc}} + \text{O}_{\text{tetra-I}})/\text{Pd}(111)$  structure, in which a linear  $\text{O}_{\text{fcc}} - \text{Pd} - \text{O}_{\text{tetra-I}}$  alignment exists as well. There, the two on-surface oxygen atoms (darker color in Fig. 5.3) in the vicinity of the sub-surface oxygen, have moved away from it (by  $0.21 \text{ \AA}$ , cf. Fig. 5.3), while no lateral displacement is observed for the remaining on-surface oxygen (participating in the linear alignment).

The difference electron density plot points toward a strong coupling between the O-Pd-O "trilayer" and the underlying palladium atoms, which is mediated predominantly by the hybridisation of Pd  $4d_{z^2}$  orbital with the O  $2s$  orbitals of the sub-surface oxygen atom. The coupling can be visualised, shown to the right of Fig. 5.5, by the following procedure. One has to obtain a self-consistent electron density for the O-Pd-O "trilayer",  $n^{\text{O-Pd-O}}(\mathbf{r})$ , and the substrate,  $n^{\text{sub}}(\mathbf{r})$ , (the  $(2 \times 2) - (2 \text{O}_{\text{fcc}} + \text{O}_{\text{tetra-I}})/\text{Pd}(111)$  geometry, without the "trilayer"). The interatomic distances of the latter two corresponding exactly to the ones of the relaxed  $(0.50 \text{O}_{\text{fcc}}/0.25 \text{O}_{\text{tetra-I}})$  geometry. Then this electron densities are sub-



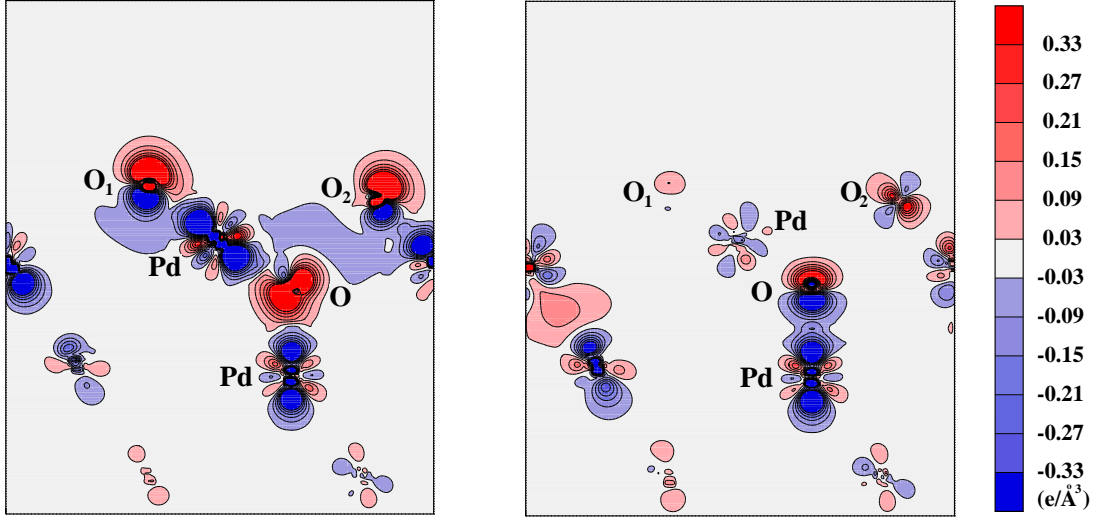


Figure 5.5: Difference electron density plot for the  $(2 \times 2) - (2O_{\text{fcc}} + O_{\text{tetra-I}})/\text{Pd}(111)$  structure visualising the bonding (left) and the coupling of the O-Pd-O trilayer to the Pd(111) substrate (right). The contour plot depicts the  $[\bar{2}11]$  plane perpendicular to the (111) surface. Regions of electron accumulation and depletion have positive and negative signs respectively, contour lines are drawn at  $0.06 e/\text{\AA}^3$ . The nomenclature  $O_1$  and  $O_2$  refers to the two on-surface oxygen atoms marked as "1" and "2" in Fig. 5.3.

tracted from that of the  $(0.50 O_{\text{fcc}}/0.25 O_{\text{tetra-I}})$  system. The coupling can be quantified by the equation

$$E_{\text{coupling}} = \frac{1}{2}(E^{\text{all}} - E^{\text{O-Pd-O}} - E^{\text{sub}}). \quad (5.5)$$

Here  $E^{\text{all}}$  is the energy of the whole system,  $E^{\text{O-Pd-O}}$  is the energy of the "trilayer" and  $E^{\text{sub}}$  is the energy of the substrate, as described above. Division by two is necessary on account of the two surfaces present in a slab. Thus it was determined that the coupling of the "trilayer" to the substrate is  $3.41 \text{ eV}/(2 \times 2)$  cell for the  $(0.50 O_{\text{fcc}}/0.25 O_{\text{tetra-I}})$  structure and  $3.83 \text{ eV}/(2 \times 2)$  cell for the  $(0.75 O_{\text{fcc}}/0.25 O_{\text{tetra-I}})$  system. The coupling in the geometry with more on-surface oxygen is somewhat stronger compared to the lower coverage case. This is most probably a consequence of repulsive interactions between the sub-surface atom and its two on-surface O neighbours (as compared to one in the lower coverage case), which push the sub-surface atom further to the outside of the "trilayer" (compare  $d_{12}$  for both structures in Fig. 5.3), thus closer to the atom beneath it. The "coupling-plot" shows, that the interaction between the Pd atoms (seen on the left side of the plot) is smaller than the coupling between the sub-surface O and the Pd atom of the second substrate layer. As the distance between the palladium atoms in the "trilayer" and the palladium atoms of the substrate layer

beneath has increased quite a lot, it is probable, that most of the coupling is the result of the interactions between the O and Pd atoms.

It was argued in the beginning of this chapter, that one of the factors playing a role towards favouring one structure over another is the coupling between the "trilayer" atoms to the palladium atoms of the second layer. In this respect, it is interesting to compare the coupling of an "unfavourable" geometry, e.g.  $(2 \times 2) - (3\text{O}_{\text{hcp}} + \text{O}_{\text{octa}})/\text{Pd}(111)$ , to the stable one at the same coverage. The coupling calculated for the  $(0.75\text{O}_{\text{hcp}}/0.25\text{O}_{\text{octa}})$  is  $1.51\text{ eV}/(2 \times 2)$  cell, which is less than half the value obtained for the stable on-/ sub-surface site combination  $(0.75\text{O}_{\text{fcc}}/0.25\text{O}_{\text{tetra-I}})$ , supporting the assumption.

## 5.4 Stability of sub-surface oxygen

Insight into the formation of surface oxides at the late  $4d$  transition metals [103] can be gained by comparing the initial incorporation of oxygen into Ru(0001) [89], Rh(111) [104], Pd(111) and Ag(111) [100]. On each of these metals the fcc/tetra-I site combination is always found to be either the most stable one or energetically very close to the most stable geometry. Therefore, the computed average binding energies of the mixed fcc/tetra-I structures, along with the values for oxygen chemisorbed in fcc sites on the surface and tetra-I sites below the surface, are used to visualise the O penetration into the basal surface of each metal, shown in Fig. 5.6. Since the highest binding energy is found for the pure on-surface chemisorption phase at  $1/4\text{ ML}$  coverage, its value is chosen as zero reference. Each subsequent contour line in the plot corresponds to a  $0.1\text{ eV}$  less stable  $E_b$ . The white circles shown in the palladium plot mark the actually calculated binding energies, cf. Table 5.4. The change in adsorption site preference from pure on-surface chemisorption at low coverages to mixed on-/sub-surface site occupation, as more and more oxygen is put on the surface, can be traced by the gradual change of the contour line slopes in the plot, at their intersection point with the x-axis. Between  $\theta_{\text{tot}} = 0.50\text{ ML}$  and  $\theta_{\text{tot}} = 0.75\text{ ML}$  the slope is actually reversed from negative to positive, indicating that occupation of sub-surface sites becomes more favourable, than the continued filling of the on-surface ones.

Pure on-surface chemisorption ( $(N_{\text{sub}}/N_{\text{tot}}) = 0\%$ ) is favoured for both Ru and Rh in the whole sub-monolayer coverage range. This means, that oxygen incorporation will only start after completion of a full O  $(1 \times 1)$  adlayer on the surface,  $\theta_c \approx 1\text{ ML}$ , in agreement with experimental findings [105, 106]. Still, the shallower valley in the Rh contour plot might account for a small, but finite concentration of sub-surface O already at total coverages slightly below  $1\text{ ML}$  at elevated temperatures [107]. The critical coverage for Ag surpasses the palladium value, so that only a small on-surface coverage may be stabilised before oxygen goes sub-surface, again, in reasonable agreement with experiment, which finds initial surface oxides at Pd(111) and Ag(111) at local coverages of  $\approx 0.7\text{ ML}$  and

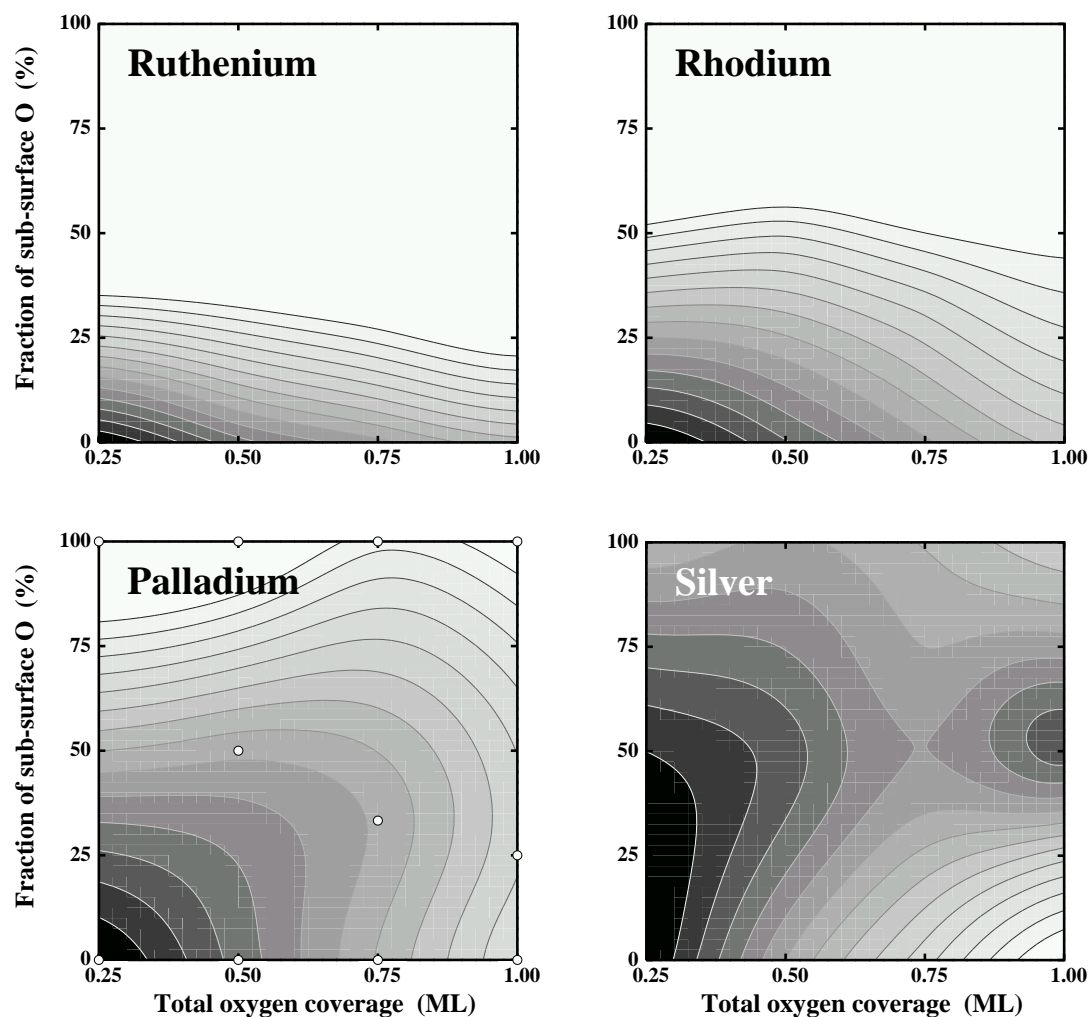


Figure 5.6: Average binding energy  $E_b$  as a function of the total oxygen coverage of which the fraction  $N_{sub}/N_{tot}$  is located below the surface (on-surface in fcc and sub-surface in tetra-I site). The highest  $E_b$  is always found for the pure on-surface chemisorption phase at  $\theta_{tot} = 0.25$  ML (chosen as zero reference, black area), with each contour line at 0.1 eV steps toward less stable  $E_b$ . The white circles in the palladium plot denote the actually calculated binding energies, displayed in Table 5.4. Data: Ru, Rh and Ag [103].

	Ru	Rh	Pd	Ag
$\theta_c$ (ML)	1.00	1.00	0.50	0.25
$\theta_c^{\text{thd}}$ (ML)	0.89	0.59	0.33	0.24

Table 5.7: Critical coverage (in ML) for oxide formation at the late  $4d$  transition metals, determined from the calculations,  $\theta_c$ , and by use of the thermodynamic model,  $\theta_c^{\text{thd}}$ .

$\approx 0.4$  ML, respectively [3, 97].

A comparison to the afore described  $\theta_c^{\text{thd}}$ , above which the bulk oxide phase becomes thermodynamically stable, reveals, that for the considered  $4d$  transition metal (TM) sequence, the critical coverages for initial O incorporation follow both the same trend and have approximately the same value, cf. Table 5.7. The similarity of  $\theta_c$  and  $\theta_c^{\text{thd}}$  reflects an important bottleneck function of the initial O incorporation in the oxidation sequence of the considered surfaces: If  $\theta_c$  was significantly smaller than  $\theta_c^{\text{thd}}$ , sub-surface O could exist as a stable phase in the coverage range up to  $\theta_c^{\text{thd}}$ . This is apparently not the case, and oxygen is only incorporated at coverages, where the bulk oxide is about to become stable. The close correlation of  $\theta_c^{\text{thd}}$  with existing experimental data on the critical coverage

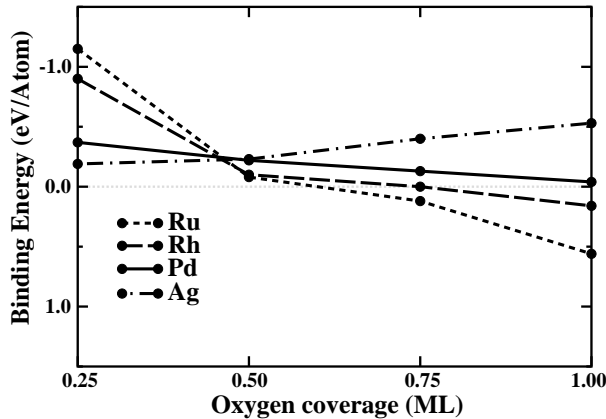


Figure 5.7: Calculated binding energies for sub-surface O incorporation into the tetra-I sites below the fully relaxed surface (no on-surface O present). The energy zero is the energy of a free  $\text{O}_2$  and the clean surface at its equilibrium geometry. Data: Ru [82], Rh [104], Ag [100].

structures containing both on- and sub-surface O as a "co-adsorbate system", as the different sites available to the two types of oxygen allow to distinguish them as two species. In this sense the stability of such structures can be discussed in

for oxide formation [97, 108] then implies that at  $\theta_{\text{tot}} \approx \theta_c \approx \theta_c^{\text{thd}}$  not only is O incorporated into the sub-surface region, but a phase transition, towards the formation of a surface oxide, is initiated. Thus, the role of sub-surface oxygen is that of a metastable precursor, and at not too low temperatures the phase transition will proceed nearly instantaneously after the first incorporation of oxygen below the surface. With this interpretation, the initial incorporation of O may be used as a good measure to understand the ease of oxide formation of these TM surfaces.

Setting out to analyse the obtained lowering of  $\theta_c$  from Ru(0001) to Ag(111), it is helpful to look upon

terms of separate properties of the on- and sub-surface O, as well as the interactions between them. The latter can be determined by comparing the binding energies computed for the mixed structures with the averaged binding energies of two calculations where O is only present in either the fcc or the tetra-I sites at the corresponding coverages. The so computed values are found to be rather small, i.e.  $< 0.2$  eV, which is comprehensible since part of them are effectively screened by the TM atoms in between (as discussed for Pd and Ag [100]). Therefore, these interactions are neglected in the following and the initial sub-surface incorporation of O, is addressed just in terms of the separate stability of on- and sub-surface oxygen.

The computed binding energies for structures that contain from one ( $\theta_{tot} = 0.25$  ML) up to four ( $\theta_{tot} = 1$  ML) sub-surface oxygens in tetra-I sites are shown in Fig. 5.7. Considering the filling of the metallic  $d$ -band as the ruling quantity to determine the O-metal bond strength across the elements, one would typically expect decreasing binding energies from Ru to Ag as in the on-surface O chemisorption case depicted in Fig. 4.3. Interestingly, this is not the case, and in particular for Ru and Rh the energies are by several eV less favourable than for chemisorption in the (also highly coordinated) on-surface hollow sites. The main reason behind this different behaviour in Figs. 4.3 and 5.7 is the lattice distortion created by the sub-surface oxygen. The deformation caused by the O incorporation into the metal surface is clearly seen by comparing the electron density plots shown in Fig. 5.8. The first picture shows the clean Pd(111) surface, followed by a bulk-truncated geometry with 1 ML oxygen incorporated in a tetra-I site. The last two pictures show the relaxed  $(1 \times 1) - \text{O}_{\text{tetra-I}}/\text{Pd}(111)$  structure, but the oxygen is removed from the tetra-I site, in the last one, showing the empty distorted lattice. In all relaxed structures the sub-surface O-metal bond lengths are each about  $2 \text{ \AA}$ . Yet, these O-metal bond lengths are incompatible with the space available inside a frozen metal lattice. For Ru, which has the smallest lattice constant of the four considered materials, the tetra-I site would only allow for an O-metal bond length of  $1.65 \text{ \AA}$ . This situation gradually becomes better for the other elements, yet even for Ag, which has the largest lattice constant, this value is with  $1.80 \text{ \AA}$  still significantly too small. To achieve its optimal bondlength the sub-surface oxygen induces a substantial local expansion of the metal lattice,

Element	Ru	Rh	Pd	Ag
$B_0^{bulk}$ (GPa)	320	259	163	81
$E_{cohesive}^{bulk}$ (eV)	6.74	6.10	3.64	2.56
$d_{111}^{bulk}$ ( $\text{\AA}$ )	2.15	2.21	2.27	2.40

Table 5.8: Bulk modulus (in GPa), cohesive energy (in eV) and distance between the  $\{111\}$  planes (in  $\text{\AA}$ ) for the late  $4d$  transition metals; Ru [82], Rh [35],  $E_{cohesive}^{bulk}$ (Ag) [4].

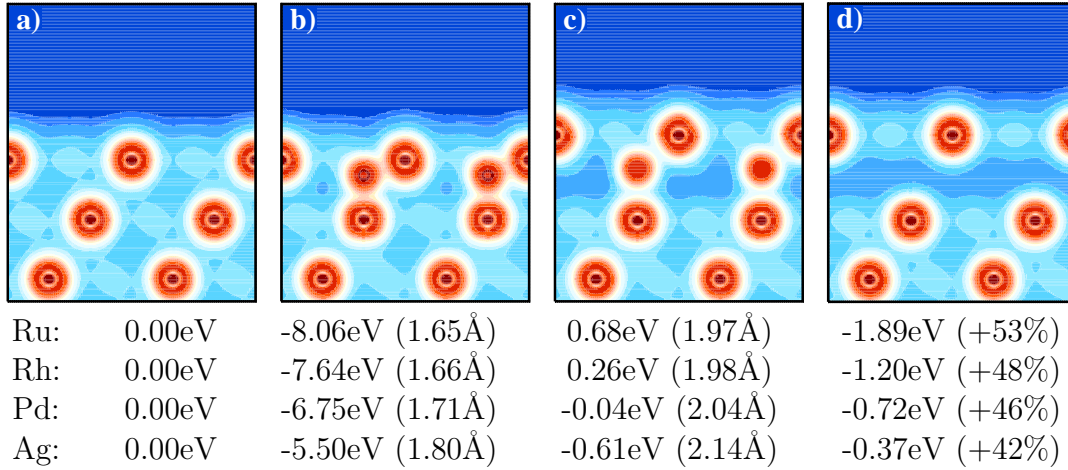


Figure 5.8: Electron density plots of the: a) clean Pd(111); b) bulk-truncated  $(1 \times 1) - \text{O}_{\text{tetra-I}}/\text{Pd}(111)$  geometry; c) relaxed  $(1 \times 1) - \text{O}_{\text{tetra-I}}/\text{Pd}(111)$  geometry; d)  $(1 \times 1) - \text{O}_{\text{tetra-I}}/\text{Pd}(111)$  geometry, with  $\text{O}_{\text{tetra-I}}$  removed. The numbers correspond to the structure shown in the picture above them, and show the binding energy (eV), the average O-TM bondlength in Å and the relaxation, due to the oxygen in %, for the late 4d transition metals. Data for relaxed Ru [82]; data for relaxed Rh [109].

which is as much as 53% for the considered Ru case. Still, the energy required to distort the corresponding TM lattice is with almost 2 eV quite high for Ru, but gradually decreases toward silver. This lattice deformation energy scales roughly like the bulk cohesive energy or the bulk modulus, cf. Table 5.8. The energy cost of distorting the metal lattice can be approximately removed by computing the binding energy of the sub-surface oxygen with respect to a metal surface which has been already deformed into the final adsorption geometry (shown in Fig. 5.8 (d)). This causes a significant increase in the binding energy, particularly for Ru and Rh, cf. Fig. 5.9. It does not remove, however, the preference of Ru and Rh for sub-surface island formation, as seen by the slope of the  $E_b(\theta)$  curves in both Fig. 5.7 and Fig. 5.9. Palladium shows no such preference, whereas in silver quite the opposite is observed - the repulsive interactions between the adsorbate atoms lead to a decrease in the binding energy with increasing coverage, which was also the case for pure on-surface adsorption. The affinity toward island formation on Ru and Rh is understandable in view of the high cost for a distortion of the lattice. Their sharing of the relaxation costs is apparently so favourable, that it overcomes even the electrostatic repulsion between the oxygens. As the lattice is easily deformed for Ag, the repulsion between O atoms plays once again a dominant role in determining their behaviour with increasing sub-surface coverage.

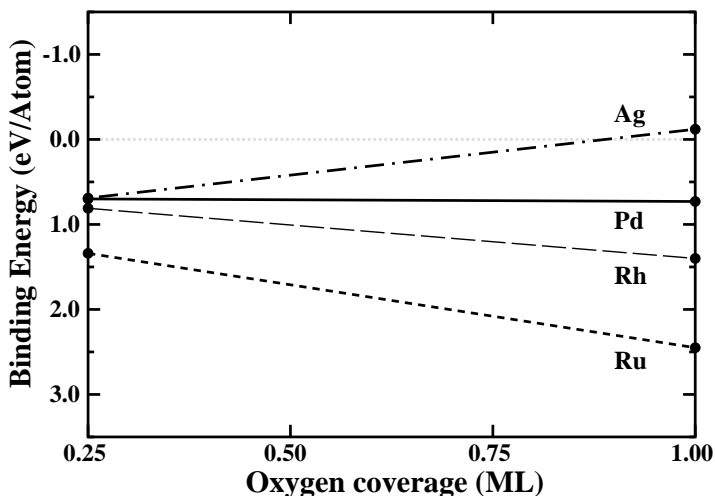


Figure 5.9: Calculated binding energies for sub-surface O incorporation into the tetra-I sites below the fully relaxed surface (no on-surface O present). The energy zero is the energy of a free  $O_2$  and the clean surface at the (artificial) geometry of the respective adsorbate system (cf. text). Data: Ru [82], Rh [109].

The gradual decrease in the deformation cost from Ru to Ag all but compensates the  $d$ -band related weakening of the O-metal bond strength, resulting in the rather similar stability of sub-surface O in all four elements. Due to this lattice distortion cost, sub-surface oxygen is in the low coverage limit always less stable than on-surface chemisorption. Yet, with increasing on-surface coverage, the repulsive interaction among the more densely packed adsorbates decreases the preference for on-surface adsorption; eventually oxygen penetration may then become more favourable than a continued filling of the on-surface sites. Correspondingly, the critical total coverage,  $\theta_c$ , beyond which penetration starts is lowered, as the lattice deformation cost become lower, i.e. it decreases from Ru to Ag.

## 5.5 Bulk dissolved oxygen

It was seen in the above discussion that the penetration of oxygen into the palladium lattice is not as costly, as e.g. Ru. Apart from this, on purely entropic grounds, there will always be a finite concentration of oxygen defects in a bulk material, even though the creation of such a defect costs energy. Therefore, it is interesting to consider what is the amount of oxygen which can be dissolved in a palladium crystal. In order to answer this question, it is necessary to know the binding energy of an oxygen atom found in an interstitial site inside the bulk. The octahedral site is the high-symmetry site with the largest volume, which means that an oxygen atom placed in it will be least squeezed in. For this

reason, the binding energy of an O atom in an octa site of a large ( $4 \times 4 \times 4$ ) palladium bulk unit cell with 97 atoms, was calculated. Relaxation of the nearest Pd neighbours is allowed, but due to the finite size of the supercell, long range elastic interactions of the metallic lattice are not properly accounted for in the resulting binding energy of  $E_b = -0.70$  eV. Estimating that the later would not improve the binding energy by more than 0.5 eV makes it possible to state a conservative upper limit of  $E_b = -0.20$  eV for the binding energy of bulk dissolved oxygen. This number brings the bulk dissolved oxygen in the stability range of sub-surface oxygen (cf. Table 5.1). Therefore and because of the vast number of available interstitial sites, it is conceivable that a considerable amount of oxygen may be deposited into a sample at finite temperatures.

The number,  $N_O$ , of oxygen atoms solved in the bulk at temperature  $T$  depends on the total number,  $N$ , of available interstitial sites. To estimate  $N_O$  the Gibbs free energy [68] has to be minimised:

$$\left. \frac{\partial G}{\partial N_O} \right|_{T,p} = \frac{\partial}{\partial N_O} \left[ E_{tot} - TS_{conf} + pV \right]_{T,p} = 0 \quad (5.6)$$

The reservoir for the oxygen solved in the bulk is the oxygen atmosphere, which is described by an O pressure  $p$  and a temperature  $T$ . The change in the internal energy of the system upon "adsorption" of an oxygen atom in a bulk interstitial site is given by  $E_{tot} = -N_O(E_b + \Delta\mu_O)$  ( $E_b > 0$  is exotherm), with  $\Delta\mu_O(T, p) = \mu_O(T, p) - \frac{1}{2}E_{O_2}$ . Usually, the number of available sites  $N$  exceeds by far the number of defect sites  $N_O$  ( $N_O \ll N$ ). Then, the configurational entropy is

$$S_{conf} = k_B \ln Z(N_O), \quad (5.7)$$

where  $k_B$  is the Boltzmann constant and the partition function is given by

$$Z = \frac{N \cdot (N-1) \cdots (N-N_O-1)}{1 \cdot 2 \cdots N_O} = \frac{N!}{(N-N_O)! N_O!}. \quad (5.8)$$

For the considered case Stirling's formula,  $\ln N! \approx N(\ln N - 1)$ , valid for  $N, N_O \gg 1$  can be used:

$$TS_{conf} = k_B T \left[ N_O \ln \left( 1 - \frac{N_O}{N} \right) - N \ln \left( 1 - \frac{N_O}{N} \right) \right]. \quad (5.9)$$

The contribution of the  $pV$  term in the Gibbs free energy is negligible [89] compared to the entropy contribution. Therefore, from the minimisation of  $G(T, p)$  one gets the formula

$$\frac{N_O}{N} = e^{[E_b + \Delta\mu_O(T,p)]/k_B T}. \quad (5.10)$$

Obviously, the concentration  $N_O/N$  of oxygen atoms in a bulk depends on the oxygen pressure and on the temperature. For  $p_O = 10^{-12}$  atm, characteristic for



UHV, and using the upper limit obtained for the binding energy, a concentration of  $1.28 \times 10^{-14}$  and  $2.42 \times 10^{-13}$  for  $T = 300$  K and  $T = 800$  K, respectively, is calculated<sup>7</sup>. The oxygen concentration in the bulk decreases as the temperature is raised, to leave the sample for the "more attractive" gas phase.

Most surface science experiments quantify uptakes in ML, which makes it seem reasonable to convert this numbers into monolayers. The volume of an octahedral interstitial site in a palladium crystal is

$$V^{\text{octa}} = \left[ \left( \frac{\sqrt{2}a_0}{2} \right)^2 \cdot \sin 60^\circ \right] \cdot \frac{\sqrt{3}a_0}{3} = 1.53 \times 10^{-23} \text{cm}^3. \quad (5.11)$$

Therefore, the number of octa sites found in a Pd crystal of  $1 \text{cm}^3$  volume is  $6.52 \times 10^{22}$  sites/ $\text{cm}^3$ , and a coverage of 1 ML corresponds to

$$\frac{1 \text{ atom}}{(\sqrt{2}a_0/2)^2 \cdot \sin 60^\circ} = 1.48 \times 10^{15} \text{atoms/cm}^2. \quad (5.12)$$

Hence the above stated concentrations translated into the equivalents of  $5.66 \times 10^{-7}$  ML and  $1.06 \times 10^{-5}$  ML at room temperature and  $T = 800$  K, respectively. In a similar study concerned with the oxygen dissolution in a ruthenium crystal [89], the negligible amount of  $1.38 \times 10^{-24}$  ML at room temperature and  $2.73 \times 10^{-12}$  ML at  $T = 800$  K is found. This notable difference in the solvent behaviour of the two elements towards oxygen reflect once more the already discussed differences in their material properties. The volume of an interstitial octahedral site in palladium is about 10 % bigger compared to ruthenium, and deformation of palladium is much less costly than deformation of ruthenium. The greater amount of oxygen solved in palladium is therefore not astonishing. Unfortunately, such studies are not yet available for Rh and Ag, but one would expect the number of oxygen atom solved in Rh to be intermediate between the ones found for Ru and Pd, whereas the palladium value will be exceeded in Ag.

---

<sup>7</sup>The values for the chemical potential of oxygen are calculated using eq. (7.6) with the appropriate value for  $1/2\tilde{\mu}_{\text{O}_2}(T, p^\circ)$  taken from Table (7.1). Thus,  $\Delta\mu_{\text{O}}(T = 300 \text{ K}, p = 10^{-12} \text{ atm}) = -0.627 \text{ eV}$  and  $\Delta\mu_{\text{O}}(T = 800 \text{ K}, p = 10^{-12} \text{ atm}) = -1.803 \text{ eV}$ .



## Chapter 6

# The $(\sqrt{5} \times \sqrt{5})R27^\circ$ surface oxide on the Pd(100) surface

After the formation of chemisorbed phases, studied in the preceding chapters, further oxidation of the palladium low index surfaces leads to the formation of surface oxides. Traditionally such initial surface oxides were considered to be closely-related, thin versions of the corresponding bulk oxides, but recent atomic-scale characterisations especially at Pd [3, 101] and Ag [102, 100, 110] surfaces revealed structures, that have often only little, if any resemblance to the bulk counterparts. The observed surface oxides usually have a low degree of order at the surface and highly complex, large unit-cell geometries, which are just a few of the difficulties one encounters, when attempting to characterise them microscopically.

Considering the oxidation of palladium, it seems logical to proceed with an investigation of the corresponding surface oxides. The surface oxide on the Pd(111) surface<sup>1</sup> has been identified [3] to be an incommensurable O-Pd-O layer. This means, that one has to use very large unit cells in order to investigate it. Therefore, this chapter will focus on the  $(\sqrt{5} \times \sqrt{5})R27^\circ$  surface oxide observed on the Pd(100) surface, which turns out to be a commensurable structure.

A view of the (100) surface is shown in Fig. 6.1. Three high-symmetry sites are present on this surface: on-top, bridge and hollow.

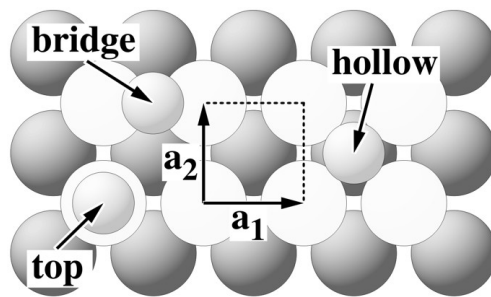


Figure 6.1: View of the Pd(100) surface. The palladium atoms are represented by the large white (1st layer) and grey (dark grey: 2nd layer) circles. The small light grey circles depict the oxygen atoms in different adsorption sites. A (1x1) cell, spanned by the primitive vectors  $\mathbf{a}_1$  and  $\mathbf{a}_2$  is shown as well. Just like on the (111) surface, an

<sup>1</sup>More details about its structure will be given in the next chapter.

atom adsorbed in an on-top site is located directly above an atom of the first substrate layer, while the bridge position is between two first layer substrate atoms. There is only *one* fourfold hollow site on the (100) surface, in contrast to the *two* threefold hollow sites found on the (111) surface. The two primitive vectors of the (100) surface are perpendicular to each other and have the length  $|\mathbf{a}_1| = |\mathbf{a}_2| = \sqrt{2}a_0/2$ .

Experimentally [27, 28, 29, 30, 31, 111] the ordered surface structures  $p(2 \times 2)$  and  $c(2 \times 2)$  have been observed for the oxygen adsorption on Pd(100). A  $p(2 \times 2)$  structure corresponds to a 0.25 ML<sup>2</sup> oxygen coverage. It has the same orientation as the cell shown in Fig. 6.1, but covers a four times larger surface area, i.e., its sidelength is  $(2 \cdot |\mathbf{a}_1|)$ . A  $c(2 \times 2)$  cell corresponds to a 0.50 ML coverage. It is half as big as a  $p(2 \times 2)$  cell and rotated by  $45^\circ$  with respect to it. The experimental studies (LEED [111] and STM [27]) found the O atoms adsorbed in the fourfold hollow sites. Therefore the calculations performed for the oxygen adsorbate phases on Pd(100) at different coverages were carried out only for the hollow site. The results of this calculations<sup>3</sup> are summarised in Table 6.1. The structural data for the  $p(2 \times 2)$  structure compare well to the experimen-

$\theta$	0.25 ML	0.50 ML	0.75 ML	1.00 ML
Parameters	O- $p(2 \times 2)$	O- $c(2 \times 2)$	3O- $(2 \times 2)$	O- $(1 \times 1)$
$E_b$ (eV/atom)	1.13	0.89	0.43	0.12
$\Phi$ (eV)	5.48	5.06	5.81	5.71
$d_{\text{O-Pd}}$ (Å)	2.13	2.03	2.08	2.05
$d_{\text{O1}}$ (Å)	0.83	0.50	0.64	0.57
$d_{12}$ (Å)	2.01 (1.9%)	2.18 (10.3%)	2.16 (9.63%)	2.29 (16%)
$d_{23}$ (Å)	1.99 (0.8%)	1.98 (0.2%)	1.97 (-0.2%)	1.96 (-0.8%)
$\Delta z_2$ (Å)	0.15	0.07	0.18	-

Table 6.1: Binding energies, relative to the dissociation energy of the oxygen molecule (in eV/atom), workfunctions, and structural parameters for O adsorbed on the Pd(100) surface.  $d_{\text{O-Pd}}$  is the oxygen palladium bondlength.  $d_{\text{O1}}$  is the distance between the oxygen layer and the first Pd layer.  $d_{12}$  and  $d_{23}$  are the distances between first and second, and second and third palladium layers, respectively. The center of mass of the corresponding layer is used to determine the interlayers distance between them.  $\Delta z_2$  is the buckling of the second palladium layer. The bulk distance is  $d_b = 1.97\text{Å}$ .

tal results [111]:  $d_{\text{O-Pd}} = 2.11\text{Å}$ ,  $d_{\text{O1}} = 0.830 \pm 0.020\text{Å}$ ,  $d_{12} = 2.01 \pm 0.015\text{Å}$ ,  $d_{23} = 1.94 \pm 0.015\text{Å}$ , and  $\Delta z_2 = 0.115 \pm 0.010\text{Å}$  (The nomenclature is the same as in Table 6.1).

<sup>2</sup>One monolayer coverage means, that the number of oxygen atoms equals the number of Pd atoms in a Pd(100) plane.

<sup>3</sup>The parameters used for this calculations are described in A.0.2.

Upon further oxidation, the two adsorption phases ( $p(2 \times 2)$  and  $c(2 \times 2)$ ) are followed by an intermediate ( $5 \times 5$ ) surface oxide, which will not be further investigated in this work. Finally, the  $(\sqrt{5} \times \sqrt{5})R27^\circ$  surface oxide (abbreviated  $\sqrt{5}$  phase in the following) concludes the series of ordered phases observed on Pd(100), for  $T > 400$  K, before three-dimensional cluster growth sets in [27].

The identification of the  $\sqrt{5}$  phase, which was made possible by a collaboration between experiment and theory [103], will be discussed in the following. Starting with a presentation of the experimental results, it will be shown that they are incompatible with an existing model [32, 33] proposed for this surface oxide phase. Afterwards a new structural model for the  $\sqrt{5}$  phase will be presented.

## 6.1 HRCLS data

Core electron wave functions are relatively compact and are generally assumed not to participate in the bonding itself. Their energies are however quite sensitive to changes in the electrostatic potential of an atom in different environments. At surfaces, the core-level energies of the substrate change relative to the bulk, giving rise to so-called surface core-level shifts (SCLSs). This shifts can be measured for both clean and adsorbate covered surfaces by high resolution core-level photoemission spectroscopy (HRCLS) [112].

A SCLS, which reflects the changes in the electronic distribution at an unperturbed surface, i.e. before the excitation of a core-hole, is called *initial state*. However, a total SCLSs comprises not only initial, but also *final state* effects, which are due to the different screening capabilities of the already core-ionised system at the surface and in the bulk [113].

From an initial state viewpoint, the core-level shifts at clean transition metal surfaces, are well understood in terms of the narrowing of the surface valence  $d$  band due to the lowered coordination [113] (cf. Fig. 3.3). The center of a less (more) than half full  $d$  band moves down (up) in energy, in order to maintain charge neutrality. The ensuing change in potential acts on the core electrons and induces a positiv SCLS (to higher binding energies) for the early and a negative SCLS (to lower binding energies) for the late transition metals. This trend involves a change in sign across the series and is confirmed by theoretical and experimental studies [113, 114, 115, 116]. The negative (initial state) SCLS calculated<sup>4</sup> for the clean Pd surface (e.g. -0.38 eV for Pd(111) and -0.43 eV for Pd(100)) fit quite nicely, as well.

Interactions of the O  $2p$  levels with the Pd  $4d$  levels upon oxygen adsorption on the Pd(111) surface, leads to the formation of bonding and antibonding states close to the lower and upper edge of the  $4d$  band (cf. Fig. 4.10), as discussed in Chapter 4. The resulting broadening of the  $d$  band requires an adjustment of the band center, in order to maintain local charge neutrality. The band shifts down

---

<sup>4</sup>The way to calculate SCLS will be described in section 6.4.3.

in energy (just opposite to the clean surface case), reflected in more and more positive SCLSs as the number of oxygen atoms on the surface increases. This has been confirmed experimentally and theoretically for, e.g., the oxygen adsorption on Ru(0001) [117] and Rh(111) [118].

The evolving sequence of ordered structures, which form on the Pd(100) surface with increasing oxygen coverage, is depicted in Fig. 6.2 by the experimental HRCL spectra for the O 1s and the Pd 3d<sub>5/2</sub> levels. The two known adsorption phases,  $p(2 \times 2)$  and  $c(2 \times 2)$ , are followed by the intermediate  $(5 \times 5)$  surface oxide, before finally the  $\sqrt{5}$  phase is obtained.

A quite surprising feature seen in the O 1s spectrum of the  $\sqrt{5}$  phase are two distinct sharp peaks in contrast to the single peak observed at all lower coverage structures. As the Pd 3p levels are lying energetically very close, they at first hinder a definite assignment to the O 1s levels. Since no similar features are observed at the low binding-energy side of the Pd 3d spectrum and after changing the photon energy to vary the escape depth of the photoelectrons, it was concluded that they must originate from oxygen atoms close to the surface. It is possible to approximately remove the contribution of the Pd 3p levels by subtracting the Pd 3p spectrum recorded from the clean surface. The corresponding HRCL spectra for the  $\sqrt{5}$  phase, now recorded at higher photon energies of 900 eV and 650 eV for the O 1s and Pd 3d levels, respectively, are shown in Fig. 6.3. The two peaks, which have a ratio of about 1:1, are still clearly distinguishable and are shifted by  $\approx 0.75$  eV with respect to each other. On the basis of this analysis the presence of at least two oxygen species, in close to equal amounts, situated at or near the surface of the  $\sqrt{5}$  phase, is anticipated.

The Pd 3d<sub>5/2</sub> spectra in Fig. 6.2, shows at least three oxygen-induced components, at  $-0.32$  eV,  $+0.38$  eV and  $+1.30$  eV, that are resolved experimentally. A positive surface core-levels shift indicates a higher binding energy with respect to the reference Pd bulk component. From the simple initial-state arguments described above, it is expected that increasing oxygen coordination yields positive SCLS for the Pd 3d<sub>5/2</sub> level. In a previous study, concerning the intermediate

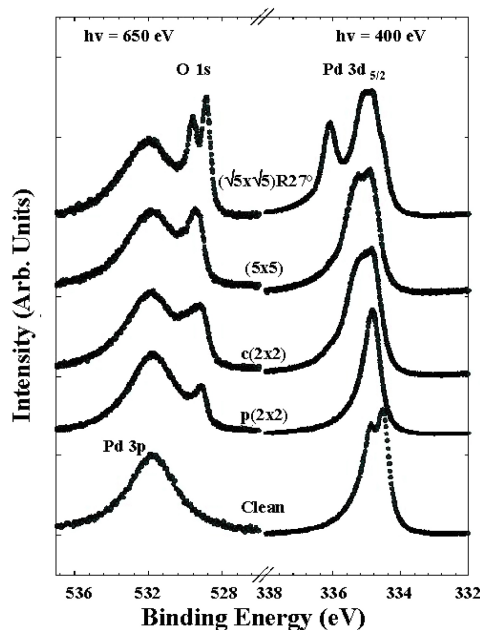


Figure 6.2: Experimental HRCL spectra of the O 1s and the Pd 3d<sub>5/2</sub> levels for the sequence of ordered structures that form on Pd(100) with increasing oxygen coverage. The photon energies were 650 and 400 eV respectively [101]

oxide structure at Pd(111) [3], a component shifted by +1.3 eV was attributed to Pd atoms fourfold coordinated to oxygen. One would, therefore, expect that the component shifted by +1.30 eV is due to similar highly oxygen coordinated Pd atoms, while the peak shifted by +0.38 eV should be assigned to Pd atoms coordinated to less oxygen atoms (possibly two or three). It was argued in the preceding that the narrowing of the  $d$  band due to a reduced coordination at the surface, leads to negative SCLSs. For this reason, the component shifted by -0.32 eV is likely to originate from Pd atoms at the interface between the Pd(100) substrate and the thin oxidic film.

## 6.2 The LEED model

A previous tensor LEED analysis suggested the  $\sqrt{5}$  phase to correspond essentially to a rumpled PdO(001) plane on top of Pd(100) [32, 33], cf. Fig. 6.4 (a). (It is abbreviated in the following with "LEED model".) As all the oxygen atoms in a PdO(001) plane are equivalent (with respect to their Pd coordination), one would typically not expect their core-levels to split. Nevertheless, it is conceivable, that the waviness of the PdO(001) overlayer, due to the inequivalent positions of the Pd atoms in it with respect to the underlying Pd(100) substrate, could affect the core-level shifts of the O atoms. Therefore, the published atomic positions were first used as input to the DFT calculation. The obtained SCLS were compared to the present HRCLS data and found to be incompatible. The LEED model was then subjected to a complete structural relaxation. The resulting final state SCLSs after relaxation are shown in Fig. 2 and are still difficult to reconcile with the experimental data: The large splitting of the O 1s spectrum is not reproduced and almost identical O 1s positions are obtained for all O atoms in the structure. The agreement of the Pd 3d SCLSs is not much better, obtaining computed shifts that are split into two distinct groups in contrast to the four component structure seen experimentally.

Geometrically, the structural relaxation in DFT almost completely removes most of the strong rumpling introduced in the LEED study to fit the experimental  $I(E)$ -curves, and the substrate/oxide interface smoothens out at a large interface distance indicating a very weak coupling. The palladium atoms of the substrate, in turn, try to assume more bulk like positions, moving to fill the voids still seen between the PdO rows. In the end, the absolute average binding energy per O atom,  $E_b$ , of the LEED model was still not very high ( $E_b = +0.32$  eV/O atom with respect to molecular oxygen), making it even more doubtful that this is the right structure to describe the Pd(100)-( $\sqrt{5} \times \sqrt{5}$ ) $R27^\circ$ -O phase.

Finally, STM (scanning tunneling microscopy) measurements of the  $\sqrt{5}$  phase, a corresponding image of which is shown in Fig. 6.3 (left), revealed that neighbouring bright rows are shifted by half a nearest neighbour distance with respect to

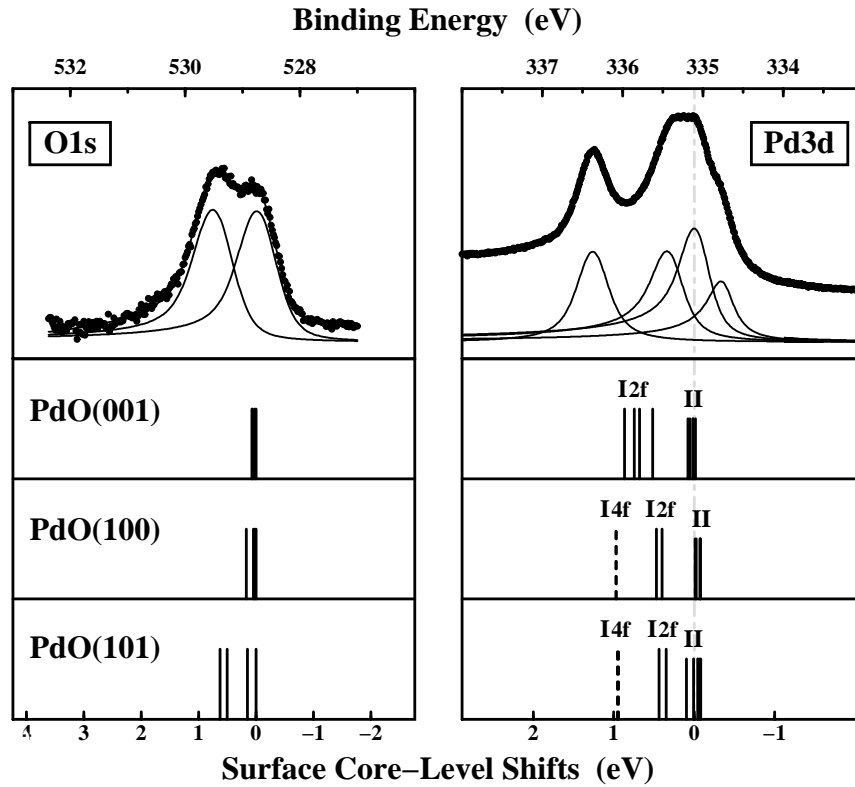


Figure 6.3: Top panel: measured HRCL spectra of the O  $1s$  and the Pd  $3d_{5/2}$  levels from the Pd(100)- $(\sqrt{5} \times \sqrt{5})R27^\circ$ -O phase at higher photon energies (900 eV and 650 eV for O  $1s$  and Pd  $3d$ , respectively) and with the Pd  $3p$  contribution of the clean surface removed. Bottom panel: Calculated final-state shifts for the three structural models shown in Fig. 6.4. For Pd  $3d$  the bulk-level is employed to align theoretical and experimental spectra. For O  $1s$  the lowest-energy theoretical peak is simply aligned to the lowest-energy experimental peak (see text). Note that only the PdO(101) layer on Pd(100) exhibits a split O  $1s$  spectrum with two significantly shifted components. See Fig. 6.4 for the nomenclature used to describe the atoms from which the various theoretical Pd core-level shifts originate.



each other, in contrast to what would be expected from the PdO(001) geometry depicted in Fig. 6.4 (a).

STM is based on the quantum mechanical tunneling between the surface of a metal or a doped semi-conductor and a metal tip, moved over the probe with the help of a piezo-ceramic control system, at less than 1 nanometer above it [119]. Applying a voltage causes a tunneling current to flow over the contact, the magnitude of which depends on the distance from the surface and its electronic structure. Scanning over the probe with a tip makes it possible to generate pictures of the surface. It is important to note that in STM the atoms are not necessarily what is imaged. Rather the tunneling current between surface and STM tip is monitored. There are two modes of operation. The first one is a constant current mode, in which the distance between tip and surface is varied to ensure a constant current flow. The second is the constant height mode, in which the tip is moved at a constant height (as indicated by the name) over the surface and the changes in the current are measured. The experimental STM images in Fig. 6.3, are taken in the constant current mode and the tunneling parameters are: voltage  $U = 0.76$  V and current  $I = 0.57$  nA.

Returning to the surface oxide, one can conclude on the basis of the STM finding, from the absence of a split in the calculated O 1s spectrum (HRCLS) and the low energetic stability (DFT), neither of which is compatible with the prevalent LEED  $\sqrt{5}$  model, that the rumpled PdO(001) overlayer on Pd(100) is most probably not the structure corresponding to the  $\sqrt{5}$  phase.

### 6.3 Searching for a new model

Considering the vast number of possibilities for the structure of the  $\sqrt{5}$  surface oxide, it is helpful to have in advance as much information about it as possible, before attempting to find an alternative geometry. Therefore, the experimental STM data are further analysed. The STM image shows two different phases, the upper one of which has a ring like structure and is identified to be the surface oxide. In the bottom right half of the STM image shown in Fig. 6.3 a coexisting domain of the  $p(2 \times 2)$  on-surface adsorption phase is seen. In the  $p(2 \times 2)$  structure the oxygen atoms are chemisorbed in the fourfold hollow sites of the underlying Pd(100) substrate [28, 29, 30, 31, 111]. A simulation of this structure<sup>5</sup> is superimposed onto the experimental image and highlighted by a black line around it. It shows that the oxygen atoms appear as dark spots in the STM image, which allows the construction of a Pd(100) lattice (filled dark circles), overlaying the experimental image in Fig. 6.3 (right). Each of these dark spots is situated directly over a palladium atom of the Pd(100) lattice, defining the

---

<sup>5</sup>The STM images (here and in the following) are simulated from the self-consistent charge density employing the Tersoff-Hamann approximation [120]. More details about the simulations are given in section 6.4.2.

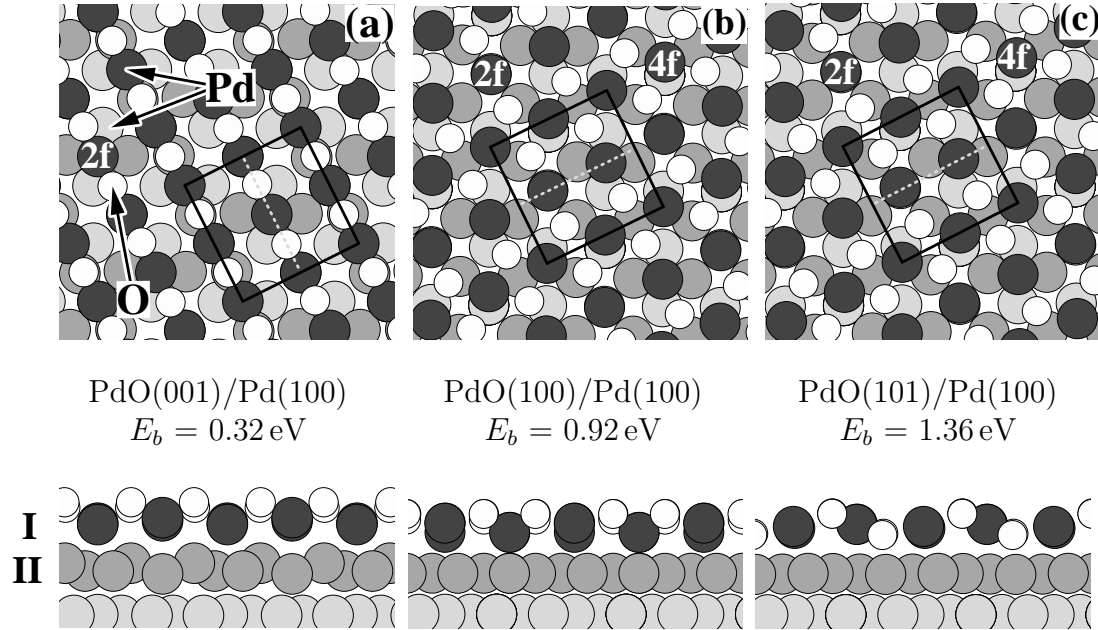


Figure 6.4: Top- and side-view of the three structural models considered for the Pd(100)- $(\sqrt{5} \times \sqrt{5})R27^\circ$ -O phase using low index PdO surfaces. All models assume an oxygen coverage of 0.8 ML. (a) PdO(001) layer on Pd(100) [32, 33], (b) PdO(100) layer on Pd(100), and (c) PdO(101) layer on Pd(100). The  $\sqrt{5}$  unit-cell is sketched in the top-view pictures (solid line), while the dashed lines indicate the direction of atomic rows seen in the STM images. The DFT binding energy of the three models clearly reveals the PdO(101) layer on Pd(100) as the most favourable model.  $2f$  and  $4f$  denote two- and fourfold coordinated first-layer Pd atoms, and relate to the labels in Fig. 6.3 used to specify the atomic origin of the various computed core-level shifts.

fourfold hollow site.

If one additionally assumes that the bright protrusion in the STM image correspond to the geometric positions of the Pd atoms, the Pd sub-lattice of the suspected surface oxide layer can also be drawn into the STM image, as done in Fig. 6.3 (right). This results in a total of three Pd atoms per  $\sqrt{5}$  unit cell, which form a rather open ring-like layer, the structure of which does not resemble any bulk-like PdO planar nearest-neighbour environment at all. The latter would be obtained, if a fourth palladium atom was present in the  $\sqrt{5}$  unit cell in the position of the large dark spots seen in the image. Analysing the relative positions of the two superimposed lattices (drawn into the experimental image), reveals that the dark spots are situated directly on top of a hollow substrate site, which would give a straightforward explanation of why these latter Pd atoms do not show up in the STM images. The Pd atoms over the Pd(100) hollow sites are expected to relax inward giving rise to a large corrugation within the surface oxide overlayer.

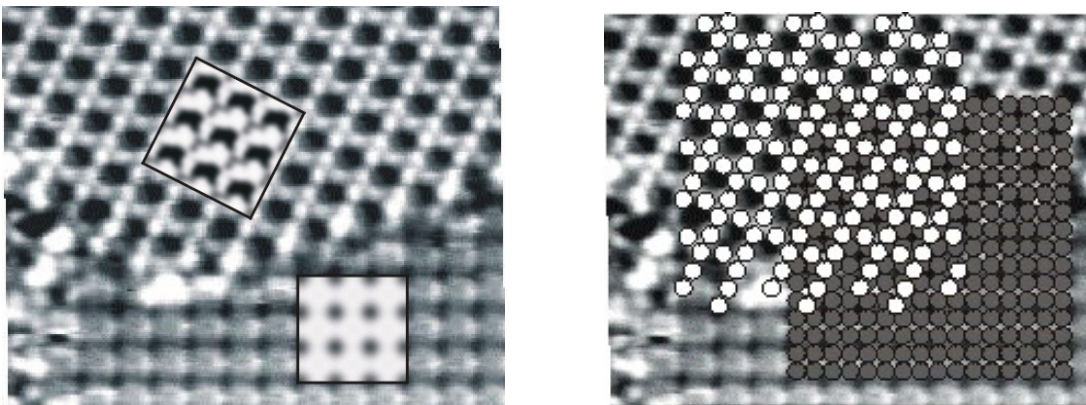


Figure 6.5: Left: STM image showing a domain boundary between the Pd(100)- $(\sqrt{5} \times \sqrt{5})R27^\circ\text{-O}$  and the  $p(2 \times 2)$  phase (lower part of the image). Right: The same STM image but with a Pd(100) lattice superimposed (grey circles). This shows directly that in the  $\sqrt{5}$  phase bright spots (assigned to Pd atoms, white circles) are shifted in neighbouring rows by half a nearest neighbour distance, and that the dark spots (Pd atoms in hollow sites) coincide with hollow sites of the underlying Pd(100) substrate (Tunnel parameters:  $U=0.76$  V,  $I=0.57$  nA). STM simulations performed for both structures (each confined by a black square) are superimposed onto the left image.

While the STM images allow a tentative determination of the positions of the Pd atoms, they do not allow for any conclusion about the position and number of O atoms in the  $\sqrt{5}$  unit cell. The latter can be, however, discerned from the HRCLS measurement. The spectra, cf. Fig. 6.2, was calibrated with the  $p(2 \times 2)$  (0.25 ML) and  $c(2 \times 2)$  (0.50 ML) adsorbate structures known from the previous LEED work [28, 29, 30, 31, 111], which allowed for a rough estimate of  $\theta \sim 0.8$  ML to be obtained. This corresponds to four O atoms per  $\sqrt{5}$  unit cell.

With this information about the position of the palladium atoms of the surface oxide and the Pd(100) substrate, relative to each other, as well as the number of Pd and O atoms per  $\sqrt{5}$  unit cell, namely 4 of each, one can proceed and set up structural models for the  $\sqrt{5}$  phase, and investigate their compatibility with the remaining data. The most appealing choice for a model, assuming that the  $\sqrt{5}$  phase is indeed some form of surface oxide on Pd(100), are then PdO-like overlayers. A systematic look at all low-index PdO planes, leads to two orientations in which the lateral arrangement of the Pd atoms corresponds to the one deduced from the STM data. These are the PdO(100) and PdO(101), shown in Fig. 6.4(b) and 6.4(c). It should be stressed that due to the *tetragonal unit-cell* of PdO [121] the PdO(001) plane and the Pd(100) plane are *not* equivalent, meaning that the LEED model features precisely an orientation, which does not fit the STM data, as seen by comparing Fig. 6.4(a) and Fig. 6.3.

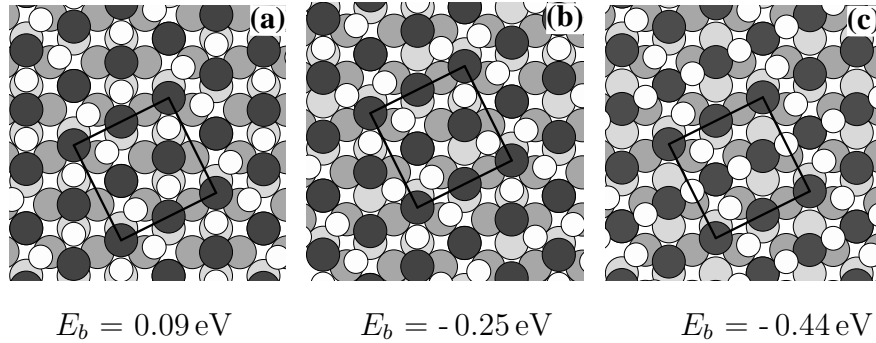


Figure 6.6: Top view of structural models, in which the overlayer does not resemble any PdO surface, considered for the Pd(100)- $(\sqrt{5} \times \sqrt{5})R27^\circ$ -O phase. In each, the position of the Pd atoms is initially fixed to the one determined on grounds of analysing the STM images. The positions of the oxygen atoms is chosen such, that some of them are in hollow and some are in bridge sites between the overlayer Pd atoms, thus producing differently coordinated O atoms at the surface (s. text). Big circles: Pd atoms (dark: overlayer, dark grey: 1st substrate layer, light grey: 2nd substrate layer); small white circles: O atoms.

## 6.4 The new model: PdO(101)/Pd(100)

### 6.4.1 Geometric consideration

A closer look at the PdO(100) and PdO(101) overlayers, filtered out as possible candidates for a new structural model, reveals that each of them has 4 Pd and 4 O atoms per  $\sqrt{5}$  unit cell, which fits nicely the previously described experimental estimations. The only difference between them is the vertical position of the oxygen atoms, all of which are above the Pd layer in the case of PdO(100), while for PdO(101) groups of two are located above and below the surface, respectively. Both structures were fully relaxed and, interestingly, each turned out to be significantly more stable than the afore discussed LEED model, providing the final evidence for the incorrectness of the latter. More precisely, the PdO(101)/Pd(100)  $\sqrt{5}$  geometry is found to be the most stable of the three, having an average binding energy of  $E_b = 1.36 \text{ eV/O atom}$ , while the corresponding number for the other two structures is  $E_b = 0.92 \text{ eV/O atom}$  for the PdO(100)/Pd(100) overlayer and  $E_b = 0.32 \text{ eV/O atom}$  for PdO(001)/Pd(100) (the LEED model). It should be stressed, that the PdO(101)/Pd(100) structure is thus more than 1 eV/O atom (!) more stable than the LEED model.

Taking into account, that the surface oxide might have a structure totally different from an PdO-layer, some further geometries were tested. As core-level shifts are known to be particularly influenced by the coordination of an atom, first geometries in which the oxygens have a different local environment were considered. Such geometries, in which the initial position of the Pd atoms are

fixed to the ones determined by the STM analysis are displayed in Fig. 6.6. It can be seen that the combinations chosen for the lateral position of the oxygen atoms is always such, that some of them are found in hollow and some of them in bridge sites between Pd atoms. As a result, the O atoms at the surface are always differently coordinated, which could possibly generate a split O 1s core-level spectrum. Yet, in all such combinatorial cases (with O in hollow and bridge sites), the obtained binding energies are significantly lower than the PdO(101)/Pd(100) model<sup>6</sup>. Tested were also two geometries (not shown) in which the palladium atoms were slightly displaced from the STM-analysis based positions and a combination of O located above and below this Pd layer, but neither of them brought an energetic improvement over the most stable model.

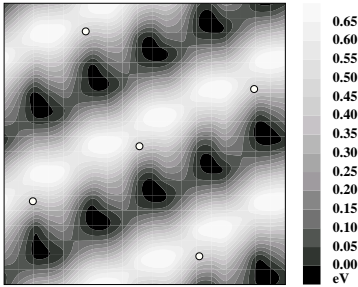


Figure 6.7: Total energy landscape, corresponding to different PdO(101) registries over the Pd(100) substrate. The white dots show the positions of the Pd atoms of the first substrate layer. The energy of the most stable geometry is taken as reference.

Their repeated appearance is due to the repetition of structures with the same registry, which reemerge, as the overlayer is shifted over the substrate. This means, e.g., that an atom which was previously in a bridge position with respect to the underlying substrate moves to a hollow position, while the reverse is true for the Pd atom, which was originally in the hollow position. The "registry" search did not reveal an energetically more stable structure. It can therefore be concluded, that each of the performed DFT calculations strongly favours the initially chosen PdO(101)/Pd(100) structure for the  $\sqrt{5}$  phase.

Finally, it is considered that the dark holes seen in the STM image could mean, that the palladium atom located over the fourfold hollow site, Pd<sub>H</sub> in Fig.6.4, is really absent. With bulk Pd as reservoir for the removed Pd atom, such a model is found to be less stable, as well ( $E_b=0.32$  eV/atom).

The last series of tests comprised a search for the optimal position of the overlayer atoms over the Pd(100) substrate. This was done by shifting the whole PdO(101) overlayer laterally over the surface, resulting in 10 additional inequivalent structures, which had to be taken into account. Any further displacement of the PdO layer leads to a geometry, which had been already calculated. The atoms of both the substrate and the overlayer, but for one Pd atom of the PdO-layer, were relaxed. The resulting energy landscape is shown in Fig. 6.7. The energy of the most stable geometry is taken as zero and appears as dark areas in the plot.

## 6.4.2 Compatibility with the STM data

To ensure the compatibility of the proposed model, PdO(101)/Pd(100) with the STM data, STM images of this structure have to be simulated. To make such

<sup>6</sup>The displayed structures were not fully relaxed. Still, considering the evolvement of the binding energy as the forces on the atoms become smaller, it is not expected, that the energy will improve by more than 0.4 eV, which is a conservative limit.

simulations possible, it was necessary to implement the according programs into the WIEN package<sup>7</sup>.

A system, which has to be considered in a STM theory is comprised of tip and probe. It is rather complex and cannot be treated without some approximations. A lack of knowledge about the precise atomic structure and chemical composition of the tip, is just one of the encountered problems.

A rather simplified theory of STM, which is used in the present work, is based on the *modified Bardeen approach*[122, 123]. The tip is regarded as a small perturbation of the system and applying Fermi's Golden rule the tunneling current can be expressed as [123]

$$I(r) = 4\pi \int_{-\infty}^{+\infty} [f(\epsilon - eU) - f(\epsilon)] n_d^t(\mathbf{r}, \epsilon - eU) n_d(\mathbf{r}, \epsilon) |M|^2 d\epsilon, \quad (6.1)$$

where  $f$  is the Fermi function,  $U$  is the applied voltage and consequently  $eU$  is the difference between the Fermi energies,  $E_F$ , of the tip and of the surface. The local density of states for the tip and the surface are  $n_d^t(\mathbf{r}, \epsilon) = \sum_i |\phi_i^t(\mathbf{r})|^2 \delta(\epsilon - \epsilon_i)$  and  $n_d(\mathbf{r}, \epsilon) = \sum_j |\phi_j(\mathbf{r})|^2 \delta(\epsilon - \epsilon_j)$ . The tunneling matrix  $M$  between tip and probe can be expressed as the integral over any surface lying entirely within the vacuum barrier region separating the two systems,

$$M_{i,j} = \frac{1}{2} \int (\phi_i^{t*} \nabla \phi_j - \phi_j \nabla \phi_i^{t*}) dS. \quad (6.2)$$

In the limit of small voltage and temperature, the Fermi functions can be approximated and eq. (6.1) simplified. It then takes the form:

$$I(\mathbf{r}) = 4\pi \int_{E_F}^{E_F + eU} n_d^t(\mathbf{r}, \epsilon - eU) n_d(\mathbf{r}, \epsilon) |M|^2 d\epsilon, \quad (6.3)$$

where  $E_F$  denotes the Fermi function of the sample.

In the theory of Tersoff and Hamann [120], the easiest imaginable approximation is used for the unknown tip-states - they are assumed to have  $s$ -like character. The tip is then modeled by a locally spherical potential centered at it, and the current can be expressed as

$$I(\mathbf{r}, U) \propto \int_{E_F}^{E_F + eU} n_d(\mathbf{r}, \epsilon) d\epsilon, \quad (6.4)$$

or using the discrete states of a supercell calculation, the integral can be evaluated as the sum,  $N_d(\mathbf{r}, U)$ , over the charge density of the Kohn-Sham-Eigenfunctions in the considered interval

$$I(\mathbf{r}, U) \propto N_d(\mathbf{r}, U) = \sum_{E_F \leq \epsilon_i \leq E_F + eU} n_d(\mathbf{r}, \epsilon_i) = \sum_{E_F \leq \epsilon_i \leq E_F + eU} |\phi_i(\mathbf{r})|^2. \quad (6.5)$$

<sup>7</sup>The details are given in the Appendix.

In other words, the tunneling current in the *Tersoff-Hamann picture* is simply proportional to the local density of states *of the surface* at the position of the tip, and is given by the properties of the surface alone, i.e., tip-surface interactions do not influence the measured current in this model. This makes simulations of STM images rather straightforward. The only thing that is needed, is the local density of states at a certain distance from the surface, which is a standard information evaluated in electronic structure methods.

STM images for each of the structures shown in Fig. 6.4 were simulated from the self-consistent charge density employing the Tersoff-Hamann approximation. The constant current STM mode is modeled by plotting the interpolated height distribution above the surface where the integrated electron density within 0.5 eV around the Fermi-level remains constant. This constant value is hereby chosen in such a way that it roughly corresponds to the electron density about 6 Å above the surface<sup>8</sup>. The three images are displayed next to each other in Fig. 6.8.



Figure 6.8: Simulated STM images for the PdO(001)/Pd(100) (left), PdO(100)/Pd(100) (middle), PdO(101)/Pd(100) (right).

They obviously look quite different from one another. To make comparison to experiment easier, each of them was superposed onto the experimental image, but only the PdO(101)/Pd(100) inset complemented it, cf. Fig. 6.3. It is now easy to verify the initial assumptions done during the analysis of the experimental STM image. The bright spots can be immediately identified as the protrusions of the three

Pd atoms in their ring-like arrangement in the PdO-layer. The palladium atom above the hollow site, Pd<sub>H</sub> (cf. Fig 6.4), is indeed seen as a dark hole. The initial interpretation is, however, not correct. It was assumed, that the origin of the strong indentation in the STM image is the inward relaxation of this atom. The calculated 0.17 Å relaxation towards the substrate is however not that large. The appearance of the Pd<sub>H</sub> as dark spots is therefore rather an electronic, than a geometric effect. This demonstrates, that one should be careful with the interpretation of STM images and resort to a simulation or some different experimental technique to verify assumptions, since the relation between an STM picture and the real geometric structure is not necessarily simple.

Dark spots at the Pd<sub>H</sub> position are also seen in the simulation of the PdO(100)/Pd(100) structure, shown in Fig. 6.8 (middle). Here, it is not that clear whether they are a consequence of the geometric structure or of electronic effects, since the inward relaxation of this atom is 0.52 Å. In the PdO(001)/Pd(100) picture, on the other hand, cf. Fig. 6.8 (left), one can be quite sure, that the observed dark rows are due to the geometry, as can be easily discerned by comparison to the structure shown in Fig. 6.4 (left).

<sup>8</sup>A sufficient criteria concerning the reliability of the Tersoff-Hamann model is that there is no substantial interactions between surface and tip. This means, that for metal surfaces the tip-sample separation has to be larger than 5-6 Å [124].



### 6.4.3 Surface core-level shifts

What remains to be seen, is if the surface core-level shifts (SCLSs) of the new model can be reconciled with the experimental HRCLS data, as well. The SCLS,  $\Delta_{SCLS}$ , is defined as the difference in energy needed to remove a core electron either from the surface or from the bulk,

$$\Delta_{SCLS} = [E^{\text{surface}}(n_c - 1) - E^{\text{surface}}(n_c)] - [E^{\text{bulk}}(n_c - 1) - E^{\text{bulk}}(n_c)]. \quad (6.6)$$

Here  $E^{\text{surface(bulk)}}(n_c)$  is the total energy of the system considered as a function of the number of electrons  $n_c$  in the corresponding core level  $c$  of a surface or bulk atom, respectively [113]. It was mentioned already, that SCLSs comprise of *initial* and *final* state effects. In the initial state approximation the SCLS arises simply from the variation of the computed orbital eigenenergies before the excitation of the core electron and are given by

$$\Delta_{SCLS}^{\text{initial}} \approx -[\epsilon_c^{\text{surface}}(n_c) - \epsilon_c^{\text{bulk}}(n_c)], \quad (6.7)$$

where,  $\epsilon_c^{\text{surface}}(n_c)$  and  $\epsilon_c^{\text{bulk}}(n_c)$  are the Kohn-Sham eigenvalues of the particular core state  $c$ . Final state effects are due to the different screening capabilities of the already core-ionised system at the surface and in the bulk. A full calculation of the SCLSs, involves an additional component due to the screening contribution from the valence electrons in response to the created core hole. It is determined by calculating the total energy of an impurity with a core hole in the selected core state. The SCLS is then the difference of two total energies, with the impurity located once at the surface and once inside the bulk [125]. This difference can also be obtained approximately via the Slater-Janak transition state approach (cf. Chapter 2.3.2) of evaluating total energy differences [48, 126]. Equation (6.6) can be transformed into the form of eq. (6.7) using the mean value theorem of integration:

$$E(n_c - 1) - E(n_c) = \int_{n_c}^{n_c-1} \frac{\partial E(n')}{\partial n'} dn' \approx -\epsilon_c(n_c - 1/2), \quad (6.8)$$

as exemplified in Ref. [117]. The initial state SCLS's can be directly obtained from the normal all-electron scheme, but the total SCLS's require an additional self-consistent impurity calculation, where one atom is ionised by removing half an electron from the considered core level. This latter approach, from which the total SCLS is derived, takes both initial and final state effects (in the spectroscopic sense) into account, so that the results can be compared with the experimental values.

The necessity to align theoretical and experimental spectra might arise. Finding a reasonable value to use as an anchor for such an alignment may present a problem. In the case of the Pd 3d SCLSs the position of the bulk value is a well defined



	Initial	Screening	Final	Experiment
$I_{4f}$ , Pd <sub>Br/H</sub>	+0.79	+0.10	+0.89	+1.30
	+0.86	+0.05	+0.91	
$I_{2f}$ , Pd <sub>Br</sub> Pd <sub>H</sub>	+0.20	+0.10	+0.30	+0.38
	+0.18	+0.21	+0.39	
II, Pd1	-0.31	+0.18	-0.13	-0.32
	-0.28	+0.19	-0.09	
	-0.26	+0.15	-0.11	
	+0.01	-0.05	-0.04	
	+0.16	-0.11	+0.05	

Table 6.2: Calculated and measured Pd 3d surface core-level shifts for the PdO(101)/Pd(100) model in eV. The computed values are separated into initial-state and screening contribution, yielding the total final-state shift that can be compared to experiment. See Figs. 6.3 and 6.4 for the notation to describe the various first (I) and second (II) layer atoms.

reference value, which can be employed. More problematic is the alignment of experimental and theoretical O 1s data. Several possible alignment procedures and problems one may encounter when using them are listed in the following. First, one could use the position of the palladium bulk value as reference for all the data. Since the two types of orbital eigenvalues (i.e. of Pd and O) have, however, a different convergence behaviour with respect to the basis set, such an alignment might require the use of very high cutoff parameters. A second possibility is the use of the Fermi-level position. For system with high oxygen loads like surface oxides, band bending can not be excluded and can present a problem, especially for experiment. A further possible alignment level is the value of the electrostatic potential in the middle of a slab. Any of this procedures should make it possible to align experimental and theoretical data to give (of course) the same result. The only information needed in the present discussion is about the existence (or non-existence) of a split in the O 1s spectrum. This difference in relative O 1s level positions of various atoms within the same geometry is well defined and independent of the reference zero used. Therefore, just in order to present the theoretical and experimental data in the same plot a rather crude, but simple alignment approach is used. The position of the lowest theoretical O 1s core-level position has been equated to the lowest lying experimental one in Fig. 6.3, for purely graphical purpose. This does not enter, however, the physical argument. A comparison of the computed final-state SCLS for the different models, presented in Fig. 6.3, makes it immediately apparent that only the O 1s core-level spectrum of the PdO(101) exhibits an appreciable split, due to the presence of both on- and sub-surface O atoms in it. The O 1s core-levels of the LEED model

		Initial	Screening	Final
on-surface,	O <sub>Br</sub>	0	0	0
	O <sub>H</sub>	0.15	0	0.15
sub-surface,	O <sub>Br</sub> <sup>sub</sup>	0.53	-0.03	0.50
	O <sub>H</sub> <sup>sub</sup>	0.70	-0.07	0.63

Table 6.3: Calculated O 1s surface core-level shifts for the PdO(101)/Pd(100) model in eV. The lowest lying value is taken as reference. Notation of the various O atoms, according to Fig. 6.9.

are lying almost on top of each other, as one would expect, since all of them have the same coordination. In the case of PdO(100) a negligible split ( $\approx 0.17$  eV), arising due to the strong corrugation of the overlayer, is observed.

On the palladium site, the three groups of shifts are obtained for both the PdO(100)/Pd(100) and PdO(101)/Pd(100), shown for the later in Table 6.2. As both of them contain the same groups of Pd atoms in the PdO-overlayer, one would expect also similar shifts of the Pd 3d levels. The obtained Pd 3d shifts of +0.9 eV and +0.4 eV are due to fourfold and twofold oxygen coordinated Pd atoms in the PdO(101) overlayer, Pd<sub>Br/H</sub> and Pd<sub>Br</sub>/Pd<sub>H</sub> in Fig. 5, and compare reasonably with the two experimental peaks that had already been assigned to differently coordinated Pd atoms on the basis of initial-state arguments. The remaining experimentally resolved peak with a small negative shift had similarly been attributed to the top Pd substrate atoms at the interface, which in the calculations exhibit almost vanishing SCLSs (Pd1 in Fig. 6.9).

Obviously, the PdO(101)/Pd(100) model is also compatible with the experimental HRCLS data. Of course, such split in the O 1s is expected solely on the basis of a geometry containing an equal amount of both on- and sub-surface oxygen. The significant rumpling together with a different coordination of the sub-surface O to the underlying substrate, yields even slightly different shifts for the two atoms of each oxygen species, cf. Table 6.3. Averaging the contributions within each group, a computed initial (final) state shift of 0.55 eV (0.49 eV) between the O 1s peaks due to on- and sub-surface oxygen atoms, is obtained, in reasonable agreement with the measured value of 0.75 eV.

## 6.5 Strained PdO(101)/Pd(100)

The new structural model for the  $\sqrt{5}$  phase is essentially a strained and rumpled PdO(101) film on top of Pd(100). The PdO(101) in-plane lattice constant is almost equal to that of a  $\sqrt{5}$  unit-cell on Pd(100), with the unit surface area of the commensurable film found here smaller by only 1.4% than for unstrained PdO(101). The vertical relaxations and the rumpling of the PdO(101)/Pd(100),

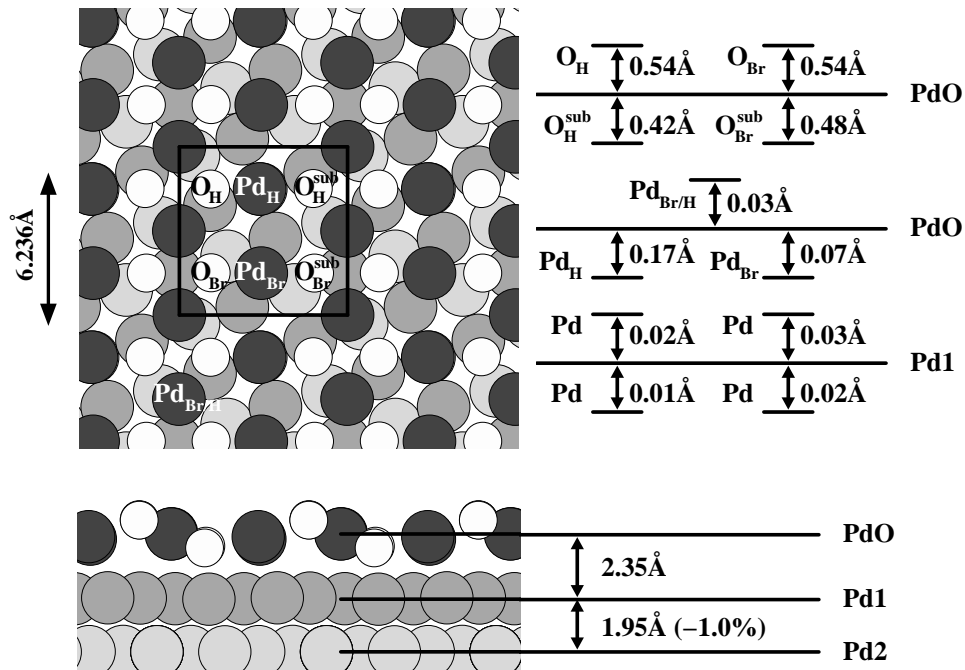


Figure 6.9: Top- and side-view of the PdO(101)/Pd(100) model for the  $\sqrt{5}$ -phase. The rumpling of both the O and Pd atoms in the PdO overlayer and of the Pd atoms in the topmost substrate layer is given with respect to the center of mass of the respective layers. In the bottom right, also the average layer distance between these center of mass are indicated.

each calculated with respect to the center of mass of the corresponding layer, are shown in Fig. 6.9. Comparison to the PdO(101) in a stoichiometric termination, reveals that the thin PdO(101) layer is more compressed perpendicular to the surface, compared to the O-Pd-O surface layer of the former. One can immediately think of two possible reasons why this is so. First, it could be an indication that the atoms in the layer are more strongly bound to each other. Comparing the average binding energy determined for the PdO(101)/Pd(100) structure, i.e.  $E_b = 1.36$  eV, to the binding energy determined for PdO(101) in a stoichiometric termination,  $E_b = 2.31$  eV<sup>9</sup>, this possibility can be, however, ruled out. The second possibility, would be that the surface oxide reacts to the slight lateral expansion by a compression perpendicular to it, so that the O-Pd bondlength attains its optimum value. As this bondlength does not change appreciably from the surface oxide to the bulk and has a value of  $\approx 2$  Å, (this was also the bondlength oxygen preferably had when chemisorbed on the Pd(111) surface), this rather favours the second assumption.

It is interesting to compare the SCLS of a PdO(101) in a stoichiometric termination to the shifts seen for the surface oxide. The Pd 3d and O 1s SCLS in the initial state for both structures are shown in Fig. 6.10<sup>10</sup>. As expected, all the oxygen bonded Pd atoms exhibit a positive shift. The two Pd(100) substrate atoms (with the positive shift) are in the vicinity of the subsurface oxygens. The other second layer Pd atoms resemble more atoms of the clean surface (-0.51 eV), as they are further away from the oxygen atoms and are not as influenced by them. As the Pd atoms of the PdO layer are also almost decoupled from these second layer Pd atoms, as well, they experience an environment similar to the one on a clean surface, which explains such a shift. The on-surface O atoms in the surface oxide resemble the on-surface O atoms in PdO(101) as they experience almost the same bonding situation. The sub-surface oxygen atoms, on the other hand, do not resemble their sub-surface counterpart in PdO(101), but seem more bulk-like. This is true in particular for the  $O_H^{\text{sub}}$ , which has a more bulk like environment. This oxygen atom is almost equidistant to all its Pd (next)neighbours, which is not the case for the  $O_{\text{Br}}^{\text{sub}}$ . The workfunction of the PdO(101)/Pd(100),  $\Phi = 5.40$  eV is somewhat higher than the value  $\Phi = 5.32$  eV for the stoichiometric PdO(101). This is probably due to the lack of the second next O-Pd-O layer, which would be present in a PdO(101), leading to an increased charge accumulation on the surface oxide side (compared to PdO(101)) and therefore to a somewhat bigger inward pointing dipole moment.

It is interesting to notice that the PdO(101) orientation is not found to be a preferred growth direction of PdO crystallites, as found experimentally [127]. Calculations [99] also show that already the bulk PdO(100) orientation shown

---

<sup>9</sup>J. Rogal, private communication

<sup>10</sup>All the PdO(101) SCLS were calculated by J. Rogal. The same muffin-tin radii,  $R_{\text{MT}}$ , as for the surface oxide calculations were used.

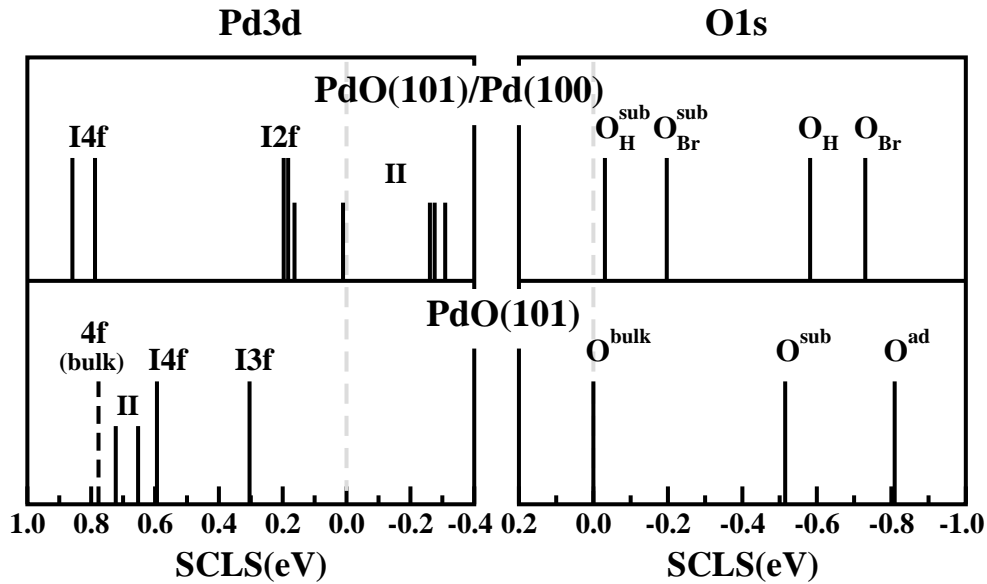


Figure 6.10: Calculated initial state Pd3d and O 1s SCSL shifts for the PdO(101)/Pd(100) structure (upper part) and a PdO(101) surface (lower part). The reference value for the Pd3d shifts is the value in a Pd bulk calculation and for the O 1s shifts, the value of O in a PdO bulk calculation is used, both indicated by dashed grey lines. Notation for PdO(101)/Pd(100) core-levels is as in Fig. 6.3. Labels for PdO(101): "I4(3)f" - fourfold (threefold) O coordinated 1 layer Pd atoms, "II" - 2 layer Pd atoms (4-fold O coordinated), "4f (bulk)" - Pd atom of the PdO bulk (also 4-fold O coordinated). The PdO bulk calculations were done by J. Rogal (using the same  $R_{MT}$ , as were used for the surface oxide calculations).

in Fig. 6.4 (middle) exhibits a significantly lower surface energy ( $33 \text{ meV}/\text{\AA}^2$ ) compared to the stoichiometric PdO(101) termination,  $57 \text{ meV}/\text{\AA}^2$ . The stoichiometric PdO(101) termination is considerably more stable than the other two ways of cleaving PdO in the (101) direction. Interestingly, the PdO(100) orientation is in the commensurable thin film geometry discussed here energetically not as favorable as the PdO(101)/Pd(100)  $\sqrt{5}$  model. Evidently, the presence of oxygen at the oxide/metal interface yields a stronger coupling to the underlying substrate and is ultimately responsible for the higher stability of the PdO(101)/Pd(100) surface oxide geometry. The coupling of the various oxide films to the Pd(100) substrate can be calculated using eq. (5.5). Thus a coupling of  $117 \text{ meV}/\text{\AA}^2$ , is calculated for PdO(101)/Pd(100), while the value for the PdO(100)/Pd(100) structure is  $109 \text{ meV}/\text{\AA}^2$ .

This example of the stabilisation of a higher energy crystal face in a thin oxide films due to strong interfacial coupling to the substrate adds another interesting aspect to the new physics found recently in studies concerning oxide formation at TM surfaces. Among other findings, the formation of incommensurable domains of low energy oxide faces has been reported for ruthenium single crystals [1, 128], delineating the opposite case to the results presented here, i.e. when the oxide orientation is more important than a good coupling to the underlying substrate. Apparently, the lower thermal stability of palladium oxides compared to RuO<sub>2</sub> increases the importance of the oxide/metal interface. This is further supported by the surface oxide structure found on Pd(111), which does not resemble any PdO bulk orientation at all [3]. Experimentally, oxide thicknesses below about 20 Å have been found in all of these cases, indicating either a slow growth kinetics once the thin films have formed or a thermodynamic hindrance to form thick bulk oxides. This could be of interest in oxidation catalysis, where such oxide patches forming on TM surfaces in the reactive environment are now discussed as the actually active material [1, 129, 130, 131]. In this context it is interesting to notice that the binding energy of the two on-surface O atoms in the PdO(101) surface oxide,  $E_b(\text{O}_{\text{Br}}) = 1.34 \text{ eV/atom}$  and  $E_b(\text{O}_{\text{H}}) = 1.42 \text{ eV/atom}$ <sup>11</sup>, do not differ much from the average binding energy determined for this structure. Furthermore, they lie in a medium range which might indeed be useful for catalysis, as comprised by the principle of Sabatier<sup>12</sup>. If a continued growth of these oxide films is not possible their structure will always remain significantly affected by the interfacial coupling. For thicker films, interfacial coupling will be progressively less influential, so that an initially stabilised higher energy oxide orientation as found in the present work should eventually become liable to faceting. The cor-

<sup>11</sup>The binding energies of the individual O atoms in the PdO(101)/Pd(100) structure can be calculated by removing the atom of interest from its position in the PdO(101) layer, i.e. creating a O vacancy in its place, and relaxing the new structure. Then one can calculate the binding energy by  $E_b(O) = \frac{1}{2}(E_{\text{PdO}(101)/\text{Pd}(100)} - E_{\text{vacancy PdO}(101)/\text{Pd}(100)} - 2(\frac{1}{2}E_{\text{O}_2}))$ .

<sup>12</sup>The principle of Sabatier states that a material should be a good catalyst if it binds atoms/molecules with an energy lying in a medium range.

responding three-dimensional cluster growth has indeed been observed for the continued oxidation of both Pd(100) and Pd(111) [26, 27].





# Chapter 7

## Thermodynamic stability/Phase diagrams

In order to gain atomic-scale understanding of the oxidation behaviour of palladium, the interactions between oxygen and the low index Pd(111) and Pd(100) surfaces were studied in the preceding chapters using DFT. However, one of the technological applications, which has led to the widespread use of palladium, is its high reactivity for the CO oxidation reaction. Whether a species is active or not depends on many factors, not the least of which are the temperature and pressure, at which this reaction takes place. Temperature and pressure can affect the stability of structures and this point was not considered so far. Clearly, the effect of  $T$  and  $p$  has to be accounted for, which can be done using the approach of "ab-initio atomistic thermodynamics" [8, 9, 10, 11, 12, 13, 14, 15].

In the following the basic ideas of this concept will be described and then applied to determine the stability range of various O-phases on the (111) and (100) surfaces of palladium.

### 7.1 Ab-initio atomistic thermodynamics

The consideration of realistic oxygen pressures and temperatures in *ab-initio* theory, can be achieved by explicitly taking the O environment, in terms of "ab-initio atomistic thermodynamics", into account. This concept is based on the assumption, that the surface is in equilibrium with the surrounding gas phase. It will be outlined in the following how the combination of thermodynamics and DFT can be applied to obtain the lowest energy surface structure with a surrounding gas phase, making it possible to construct a  $(T, p)$ -diagram of the stability regions of different surface phases.

The oxygen atmosphere with which a considered surface is in contact is described by the O pressure  $p$  and a temperature  $T$ . The environment then acts as a reservoir, since it can supply oxygen to the substrate or take oxygen from it, without

changing the temperature and pressure. The surface free energy, determined by

$$\gamma(T, p) = [G(T, p, N_{\text{Pd}}, N_{\text{O}}) - N_{\text{Pd}}\mu_{\text{Pd}} - N_{\text{O}}\mu_{\text{O}}]/A \quad (7.1)$$

is minimised by the most stable surface composition and geometry. Here  $\mu_{\text{Pd}}$  is the chemical potential of a Pd atom in the bulk and  $\mu_{\text{O}}$  is the chemical potential of an O atom in the gas phase, while  $N_{\text{Pd}}$  and  $N_{\text{O}}$  are the respective number of atoms. Furthermore,  $\gamma(T, p)$  is normalised to energy per unit area by dividing through a surface area  $A$ .

In experiment usually the  $\text{O}_2$  pressure and temperature are varied. It is therefore most useful to consider the stability of the surface structure with respect to  $\mu_{\text{O}}(T, p)$ . It is important to note that experimentally (and assuming that thermodynamic equilibrium applies),  $\mu_{\text{O}}$  can only be varied within certain bounds. If the oxygen chemical potential becomes too low, all oxygen would leave the sample, i.e. the oxide would decompose into solid Pd and oxygen gas. This means that in a pure oxygen environment, the condition for the stability of a bulk oxide ( $\text{M}_x\text{O}_y$ ) is

$$g_{\text{M}_x\text{O}_y}^{\text{bulk}} < xg_{\text{M}}^{\text{bulk}} + y\mu_{\text{O}}, \quad (7.2)$$

i.e.

$$\Delta\mu_{\text{O}} > \frac{1}{y} \left[ g_{\text{M}_x\text{O}_y}^{\text{bulk}} - xg_{\text{M}}^{\text{bulk}} - \frac{y}{2}E_{\text{O}_2}^{\text{total}} \right]. \quad (7.3)$$

Here  $\Delta\mu_{\text{O}}$  is defined as  $\mu_{\text{O}} - (1/2)E_{\text{O}_2}^{\text{total}}$ . For  $T = 0\text{ K}$  the bracket on the right hand side equals half of the low temperature limit of the heat of formation,  $H_f(T = 0\text{ K}, p = 0\text{ atm})$ , of the bulk oxide. As the  $(T, p)$ -dependence of the bulk phases is rather small, the right hand side will still be quite close to the  $H_f(T = 0\text{ K}, p = 0\text{ atm})$ -value, even for higher temperatures. Therefore the above can be rewritten to give the stability condition

$$\Delta\mu_{\text{O}} \gtrsim \frac{1}{y}H_f(T = 0\text{ K}). \quad (7.4)$$

On the other hand, the most oxygen rich-condition can be defined, as the point beyond which gas phase O would start to condense on the sample. Since the critical temperature for oxygen condensation is too low, compared to the temperature used e.g. under catalytic conditions, a condensation phase does not exist in the temperature range of interest. Still, an appropriate and well-defined estimate of the upper limit is  $\Delta\mu_{\text{O}} < 0$ .

The Gibbs free energy of formation of the palladium oxide at zero temperature and pressure is determined by

$$\begin{aligned} \Delta G_f(0, 0) : 2\text{Pd}(s) + \text{O}_2(g) &\rightarrow 2\text{PdO}(s) \\ \Delta G_f(0, 0)(\text{PdO}) &\approx \frac{1}{2}\{E(2\text{PdO}) - E(\text{O}) + 2E_b - 2E(\text{Pd})\} = -\mathbf{0.869}\text{ eV}^1 \end{aligned} \quad (7.5)$$

---

<sup>1</sup>J.Rogal, private communication.

$T$	$\mu_{\text{O}}(T, p^0)$	$T$	$\mu_{\text{O}}(T, p^0)$
100 K	-0.08 eV	600 K	-0.61 eV
200 K	-0.17 eV	700 K	-0.73 eV
300 K	-0.27 eV	800 K	-0.85 eV
400 K	-0.38 eV	900 K	-0.98 eV
500 K	-0.50 eV	1000 K	-1.10 eV

Table 7.1:  $\mu_{\text{O}}(T, p^0)$  in the temperature range of interest to the present study. The entropy and enthalpy changes used to obtain  $\mu_{\text{O}}(T, p^0)$  were taken from the JANAF thermochemical tables at  $p^0 = 1$  atm [132].

The  $T$  and  $p$  dependence is given mainly by the oxygen chemical potential,  $\mu_{\text{O}}$ , i.e. by the  $\text{O}_2$  gas phase atmosphere:

$$\mu_{\text{O}}(T, p) = \frac{1}{2} \left[ E_{\text{O}_2}^{\text{total}} + \tilde{\mu}_{\text{O}_2}(T, p^0) + k_B T \ln \left( \frac{p_{\text{O}_2}}{p^0} \right) \right], \quad (7.6)$$

where the temperature dependence of  $\tilde{\mu}_{\text{O}_2}(T, p^0)$  includes the contributions from rotations and vibrations of the molecules, as well as the ideal-gas entropy at  $p^0 = 1$  atm. The latter quantities can be computed from first principles, yielding results that are at the temperature range of interest, virtually indistinguishable from the experimental values listed in thermodynamic tables [132]. The values used for  $\tilde{\mu}_{\text{O}_2}(T, p^0)$  in the present work are taken from Ref. [89] and are listed in Table 7.1. The above formula further allows to convert results obtained as a function of the oxygen chemical potential, into pressure scales at any specific temperature.

As a main point of interest in this chapter is to investigate the effect of pressure and temperature on the stability of the various structures analysed in the previous chapters, one can follow the approach of Li, Stampfl and Scheffler[100] to evaluate the Gibbs free energy of adsorption and compare it to other possible states of the system like on- or sub-surface oxygen phases or the bulk oxide. The Gibbs free energy of adsorption can be written as

$$\begin{aligned} \Delta G(\Delta\mu_{\text{O}}) &\approx -\frac{1}{A} \left[ E_{\text{O}@Pd}^{\text{total}} - E_{\text{Pd}}^{\text{total}} - N_{\text{O}} \left( E_{\frac{1}{2}\text{O}_2} + \Delta\mu_{\text{O}} \right) \right] \\ &= \frac{N_{\text{O}}}{A} \left[ E_{\text{O}@Pd}^{\text{bind}} + \Delta\mu_{\text{O}} \right]. \end{aligned} \quad (7.7)$$

Here,  $E_{\text{O}@Pd}^{\text{total}}$  and  $E_{\text{Pd}}^{\text{total}}$  are the total energies of the surface with and without oxygen coverage of  $N_{\text{O}}$  oxygen atoms per surface area  $A$ . In the second line, the first terms in the brackets have been identified with the average binding energy of oxygen in the particular surface configuration and with respect to  $1/2E_{\text{O}_2}^{\text{total}}$ .

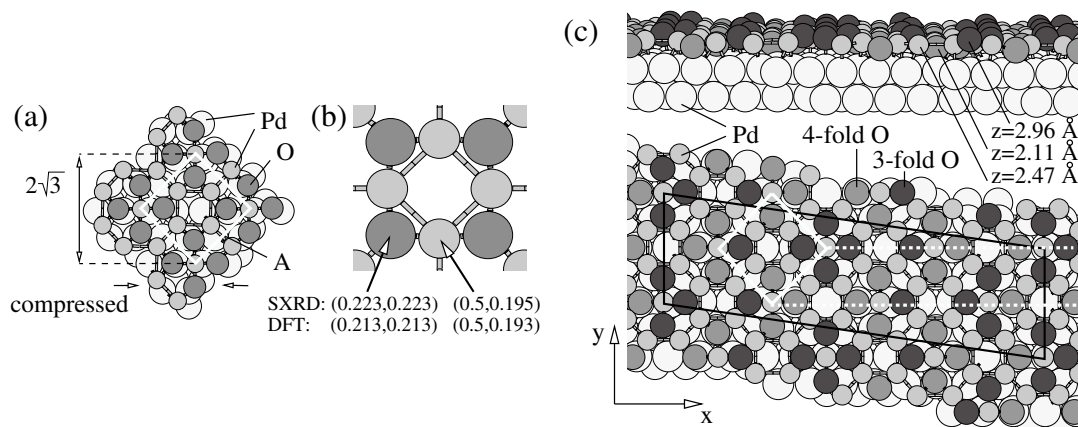


Figure 7.1: Surface oxide on the palladium (111) surface. The figure is taken from Ref. [3]. (a) unit cell of the  $\text{Pd}_5\text{O}_4$  surface oxide, (b) experimental (SXR) and theoretical (DFT) positions of the atoms in the unit cell, as multiples of the unit vectors of the adlayer, (c) Seven times replicated  $\text{Pd}_5\text{O}_4$  overlayer on the Pd(111) substrate resulting in the lowest energy concerning the registry of the oxygen layer to the substrate. The black lines show the supercell, the white square indicates the unit cell of the adsorbate.

## 7.2 Stability Range on Pd(111)

Starting with the Pd(111) surface, the above described formalism is used to study the stability of the different O-Pd phases on it. The binding energies for the stable oxygen adsorbate phases on Pd(111) are listed in Table 7.2, which means that for 3/4 ML and 1.00 ML coverages, the mixed  $\text{O}_{\text{fcc}}/\text{O}_{\text{tetra-I}}$  combinations are considered. The structure at the bottom of the table is the surface oxide identified on the Pd(111) surface [3], which has not been discussed so far.

This surface oxide is a O-Pd-O layer with a rather complicated structure, shown in Fig. 7.1. The site of its unit cell has the length  $\sqrt{6}$ . Therefore, this structure has been termed " $(\sqrt{6} \times \sqrt{6})\text{-O}$ ", in spite of the facts that it is a square structure on a substrate with threefold symmetry. It has 5 palladium and 4 oxygen atoms per unit cell and the oxygen coverage corresponds to 0.67 ML. The unit cell is commensurate in the direction of one cell diagonal (marked as " $2\sqrt{3}$ " in Fig. 7.1 (a)) and compressed along the other diagonal to reach commensurability. The oxygen atoms in the layer are quite buckled ( $\approx 0.85 \text{ \AA}$ ). There are two kinds of oxygen atoms in the  $\text{Pd}_5\text{O}_4$  layer. Half of the O atoms are threefold coordinated and bonded only to in-plane Pd atoms, the other half is fourfold coordinated and bonded also to the sub-surface Pd atoms, above which they are located. Four palladium atoms per unit cell are coordinated to two neighbouring oxygen atoms. The remaining palladium atom is coordinated to four oxygen atoms. The fourfold coordinated Pd atoms are located above densely packed Pd atom rows

$\theta$ /Structure	$E_b$ (eV)	$\Delta G(\Delta\mu_O)(\text{eV}/\text{\AA}^2)=$	$(\Delta\mu \mid \Delta G)$
0.25ML O O ( $2 \times 2$ )	1.47	$(1.47 + \Delta\mu)/26.942$	$(0 \mid 0.054)$ $(-2 \mid -0.020)$
0.50ML O O ( $2 \times 1$ )	1.12	$2 \cdot (1.12 + \Delta\mu)/26.942$	$(0 \mid 0.083)$ $(-2 \mid -0.065)$
0.75ML O 0.50 O <sub>fcc</sub> /0.25 O <sub>tetra1</sub>	0.84	$3 \cdot (0.84 + \Delta\mu)/26.942$	$(0 \mid 0.094)$ $(-1.742 \mid -0.100)$
1.00ML O 0.75 O <sub>fcc</sub> /0.25 O <sub>tetra1</sub>	0.49	$4 \cdot (0.49 + \Delta\mu)/26.942$	$(0 \mid 0.072)$ $(-1.162 \mid -0.100)$
0.67 ML $(\sqrt{6} \times \sqrt{6})$ -O	1.38	$4 \cdot (1.38 + \Delta\mu)/46.752$	$(0 \mid 0.118)$ $(-2 \mid -0.053)$

Table 7.2: The binding energies of different O/Pd(111) stable phases, and the structures they correspond to, are shown in the first two columns. The functional dependence of the change in Gibbs free energy on the chemical potential,  $\Delta G(\Delta\mu_O)$ , and the endpoints of the lines shown in Fig.7.2, calculated by this formula, are shown as well.

of the substrate, indicated by dashed lines in Fig. 7.1 (c). In contrast to the previously discussed surface oxide on the Pd(100) surface, the " $(\sqrt{6} \times \sqrt{6}) - \text{O}$ " structure has neither the stoichiometry nor structural similarity to any plane of the bulk PdO oxide.

The  $(\sqrt{6} \times \sqrt{6})$  cell covers an area of 6.92 Pd(111) unit cells. This information is used to calculate the surface area of the surface oxide

$$A(\sqrt{6} \times \sqrt{6}) = 6.92 \left[ \left( \frac{a_0^{\text{bulk}}}{\sqrt{2}} \right)^2 \sin 60^\circ \right] = 46.752 \text{\AA}^2. \quad (7.8)$$

As the calculations for the  $(\sqrt{6} \times \sqrt{6}) - \text{O}$  were performed with a different (pseudo-potential) code, the binding energies are shifted with respect to the ones determined in the present work. This can be seen by comparing the energies of the O ( $2 \times 2$ )/Pd(111) and O ( $2 \times 1$ )/Pd(111) structures of this work to the published ones, i.e. 1.36 eV and 0.95 eV [3]. To better compare to the data of the present work, this information is used to shift the value determined for the binding energy of the surface oxide (1.24 eV) to 1.38 eV (this value is used in the following). Such a shift does not affect the stability range of the different structures seen the stability diagram (Fig. 7.2), since only the difference between the energies of various structures matters for the plot<sup>2</sup>. Redrawing the figure (not shown) with the energies from Ref. [3] results in a overall shift of the plot, but the width of the various stability regions is not affected.

Apart from the binding energies, Table 7.2 shows the dependence of the Gibbs

<sup>2</sup>Should one use the value 1.24 eV [3] for the binding energy of the surface oxide, the stability range of the surface oxide becomes smaller, but it still exceeds the stability of the bulk oxide.

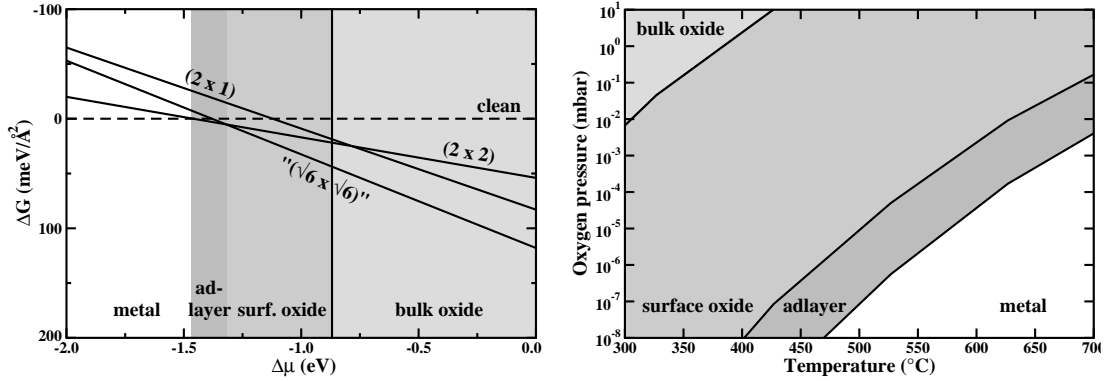


Figure 7.2: Computed Gibbs free energy of adsorption (left) for the  $p(2 \times 2)$  and the hypothetical  $p(2 \times 1)$  on-surface adsorption phase, as well as for the so-called  $(\sqrt{6} \times \sqrt{6})$ -O surface oxide on Pd(111). The stability range of the surface oxide extends beyond that of the bulk oxide, given by  $\Delta\mu_{\text{O}} \gtrsim -0.9$  eV, but there is also a finite range in which an ad-layer forms the thermodynamically most stable phase. The dependence on  $\Delta\mu_{\text{O}}$  is translated into  $(p, T)$ -phase diagram (right). In the bottom of each figure, the "material type" which is stable in the corresponding range of O chemical potential is listed and indicated by different colors.

free energy of adsorption,  $\Delta G(\Delta\mu_{\text{O}})$ , on the oxygen chemical potential for each considered case. The resulting stability diagram is shown in Fig. 7.2. The range of O chemical potential in which an according phase is thermodynamically stable is indicated by different background colours. At the bottom of each shaded region, the the corresponding stable phase is listed, as well. The Gibbs free energy of adsorption of the clean Pd(111) surface is obviously not dependent on the oxygen chemical potential. For low  $\mu_{\text{O}}$  it will be the most stable phase. As the oxygen pressure increases, i.e. increasing oxygen chemical potential, it gets harder to stabilise an oxygen deficient surface. Therefore a phase containing oxygen will eventually become more stable than the clean surface. For the considered (111) surface, the intersection point between the dashed line ( $\Delta G(\Delta\mu_{\text{O}})$  of the clean surface) with the line representing  $\Delta G(\Delta\mu_{\text{O}})$  of the  $p(2 \times 2)$  phase, indicates the chemical potential at which the 0.25 ML adsorbate phase becomes the favoured one. Obviously, the higher the oxygen content of a considered surface structure is, the steeper the decrease of  $\Delta G(\Delta\mu_{\text{O}})$  will be with increasing chemical potential. In the limit of an infinitely thick bulk oxide on top of the metal substrate, this will result in a vertical line that crosses the zero-axis at the stability condition for the bulk oxide in eq. (7.4). This value was determined earlier to be  $\Delta G_f(\text{PdO}) = -0.869$  eV (cf. eq. (7.5)). For any higher  $\Delta\mu_{\text{O}}$  the bulk oxide will be the stable phase. The region of bulk oxide stability is indicated in Fig. 7.2, as well.

The interesting question about the stability of the thin surface oxides, which are

found on both palladium surfaces considered in this work, arises. The previous discussion revealed that these thin films hardly resemble their bulk counterparts and/or are influenced by a strong coupling to the underlying metal substrate. Due to this coupling and structures particularly suited for layered configurations, one may expect the stability range of surface oxides to exceed that of the according bulk oxide. This is indeed seen in the diagram, which shows that the  $(\sqrt{6} \times \sqrt{6})$ -O structure becomes stable much earlier than the bulk oxide.

Therefore the  $\Delta G(\Delta\mu_{\text{O}})$  plot can be summarised as follows: After the formation of the well studied  $p(2 \times 2)$  on-surface adsorption phase, a further increase in oxygen pressure leads to the formation of the surface oxide, the stability of which exceeds that of the bulk oxide. This means, that from a thermodynamic point of view, only one of the O adsorbate structures discussed in connection with Pd(111) is relevant during the oxidation of this surface, since immediately after it the surface oxide should become stable. However, a thermodynamic picture totally disregards kinetic effects, which may well hinder the formation of a certain phase at conditions (i.e.  $p, T$ ) derived from thermodynamics.

Using eq. (7.6) the  $\Delta G$  vs.  $\Delta\mu_{\text{O}}$  plot can be transformed into a  $(T, p)$ -phase diagram. The different thermodynamically stable phases are separated from each other by lines (black lines in Fig. 7.2 (right)) of constant chemical potential. They correspond to the vertical lines in the  $\Delta G(\Delta\mu_{\text{O}})$  plot, given by the borders of the grey shaded areas in the left-hand side part of the figure. It is important to notice that these lines are parallel to each other, but shifted. Their inclination is such, that they run always from the lower left part of the  $(T, p)$ -diagram, i.e. lower temperature and pressure, to the upper right side of it, i.e. higher temperature and pressure. This should invariably be the case in thermodynamic equilibrium. The binding energy enters eq. (7.7). Therefore, changes in the binding energy can shift the lines of constant chemical potential, which separate the stability region of different phases. This means, that there is some uncertainty in the position of the drawn lines. Within the uncertainty limit estimated for the binding energies, this may mean a shift of up to 100 K in the temperature, and up to two orders of magnitude in the pressure scales.

### 7.3 Stability Range on Pd(100)

During the oxidation of the Pd(100) surface a  $p(2 \times 2)$  and a  $c(2 \times 2)$  ordered ad-layer structure with O in a fourfold hollow site [27, 111], as well as an ensuing  $(\sqrt{5} \times \sqrt{5})R27^\circ$ -O surface oxide phase, which has been studied in the preceding chapter, have been identified. The calculated binding energies of the possible O adsorbate structures, for oxygen coverages up to 1 ML with oxygen adsorbed in the fourfold hollow site, as well as the average binding energy determined for the surface oxide, are all listed in Table 7.3. They were used to obtain the  $\Delta G(\Delta\mu_{\text{O}})$  plot for the Pd(100) surface displayed in Fig. 7.3. The most striking feature of

<i>coverage</i>	$E_b$ (eV)	$\Delta G(\Delta\mu_O)(\text{eV}/\text{\AA})=$	$(\Delta\mu \mid \Delta G)$
0.25 ML O $p(2 \times 2)$	1.13	$(1.13 + \Delta\mu)/31.11$	$(0 \mid 0.036)$ $(-2 \mid -0.028)$
0.50 ML O $c(2 \times 2)$	0.88	$2 \cdot (0.88 + \Delta\mu)/31.11$	$(0 \mid 0.057)$ $(-2 \mid -0.072)$
0.75 ML O $3O(2 \times 2)$	0.43	$3 \cdot (0.43 + \Delta\mu)/31.11$	$(0 \mid 0.041)$ $(-1.462 \mid -0.100)$
1.00 ML O $O(1 \times 1)$	0.19	$(0.19 + \Delta\mu)/7.778$	$(0 \mid 0.025)$ $(-0.972 \mid -0.100)$
0.80 ML O PdO(101)/Pd(100)	1.36	$4 \cdot (1.36 + \Delta\mu)/38.89$	$(0 \mid 0.140)$ $(-2 \mid -0.066)$

Table 7.3: The calculated binding energies of different O/Pd(100) stable phases, and the structures they correspond to, are listed in the first two columns. The functional dependence of the change in Gibbs free energy on the change in chemical potential,  $\Delta G(\Delta\mu_O)$ , and the endpoints of the lines shown in Fig.7.3, calculated by this formula, are shown as well.

the plot is the  $\Delta\mu_O$ -range, in which the surface oxide has the lowest Gibbs free energy of adsorption (in comparison with all the considered structures). It not only exceeds the one of the PdO bulk, as discussed previously and already seen for the basal surface of palladium, but also the range in which the on-surface adsorption phases are more stable than the clean Pd(100) surface. This means, that the latter on-surface phases never correspond to a thermodynamically stable phase, and their frequent observation in UHV experiments [27, 111] appears to be the mere outcome of the limited O supply offered, as well as of kinetic barriers e.g. for O penetration at the low temperatures employed (UHV experiments are typically performed by depositing a finite number of ad-atoms, rather than by maintaining a given gas pressure).

Comparing this to the results shown in Fig. 7.2, it is evident that there are environmental conditions for which the surface oxide may already be thermodynamically stable on Pd(100), while on-surface adsorption still prevails on Pd(111).

Recently an experimental "surface phase diagram" for Pd(100) has been obtained by means of *in-situ* surface X-ray diffraction (SXRD) measurements [133]. The oxidation of the Pd(100) surface was monitored over the pressure range from  $10^{-6}$  to  $10^3$  mbar and up to sample temperatures of 1000 K. The formation of both the  $(\sqrt{5} \times \sqrt{5})R27^\circ$  surface oxide [101] and the transformation to a three-dimensional bulk oxide films have been seen. As the oxide growth thicker the  $(\sqrt{5} \times \sqrt{5})R27^\circ$  structure disappears from the surface, i.e. the initially formed PdO(101) plane does not continue to grow but instead restructures. This is in agreement with the observation that the (101) orientation is a high-energy facet of PdO [99], and also



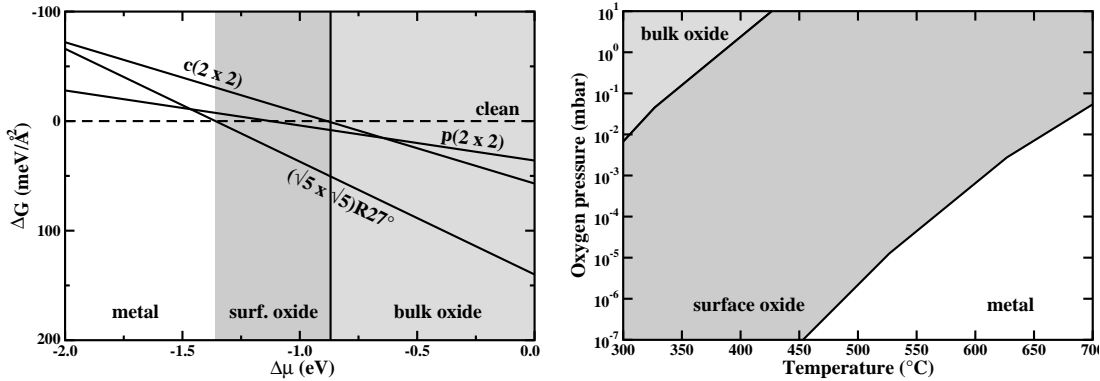


Figure 7.3: Computed Gibbs free energy of adsorption (left) for the  $p(2 \times 2)$  and the  $c(2 \times 2)$  on-surface adsorption phase, as well as for the  $(\sqrt{5} \times \sqrt{5})R27^\circ$ -O surface oxide on Pd(100). The stability range of the surface oxide extends once more beyond that of the bulk oxide, cf. Fig. 7.2, but no adlayer forms a thermodynamically stable phase. The surface oxide is the first oxygen phase stable after the clean surface. The  $(p, T)$ -phase diagram is shown again on the right side.

with experimental observations concerning the preferred growth direction of PdO [127]. It also supports the assumption that the strong coupling to the substrate, which was important for the stabilisation of the one O-Pd-O layer thick surface oxide, is no longer that important as the oxide film grows thicker.

The experimental and theoretical  $(T, p)$ -phase diagram (cf. Fig. 7.3), are compared in Fig. 7.4. The measured points are indicated in Fig. 7.4 (left). The drawn "phase boundaries" are rough estimates to guide the eye. Most strikingly, the  $(\sqrt{5} \times \sqrt{5})R27^\circ$  structure is found under a wide variety of conditions – even at an oxygen pressure of  $10^3$  mbar and a sample temperature of 575 K only the formation of this surface oxide is observed and no indications for the growth of a thicker oxide film (on the currently experimentally accessible time scale of the order of 1 hr) is found.

A gratifying overall agreement between theory and experiment in this wide range of environmental conditions is encountered. There are, however, also notable differences that go beyond the uncertainties underlying both the experimental and theoretical approach. This is particularly the observation of the  $(\sqrt{5} \times \sqrt{5})R27^\circ$  surface oxide in the top left corner of the experimental diagram, i.e. at lower temperature and high pressures. A central assumption of theory, which predicts the stability of the bulk oxide under such conditions, was a full thermodynamic equilibrium between surface and gas phase. Therefore this deviation between the experimental and theoretical  $(T, p)$ -phase diagram may be interpreted as a reflection of kinetic limitations to the growth of the bulk oxide under such conditions. Such a limitation is indeed apparent even by taking the experimental data on their own. If the surface was fully equilibrated with the environment, the eval-

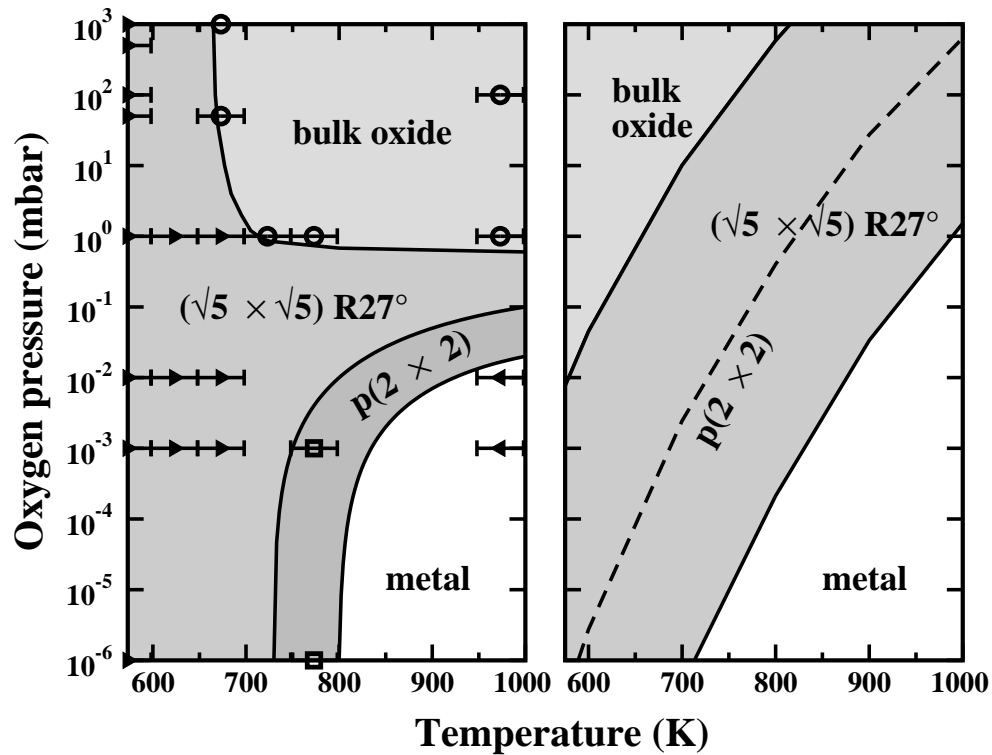


Figure 7.4: Left:  $(T,p)$ -diagram showing the measured phases in the whole range of experimentally accessible conditions from UHV to ambient pressure. The "phase boundaries" (see text) are rough estimates to guide the eye. Right: Corresponding surface phase diagram, as calculated by first-principles atomistic thermodynamics. The dashed line indicates the thermodynamic stability of the  $p(2 \times 2)$  adphase, if formation of the surface oxide was kinetically inhibited.

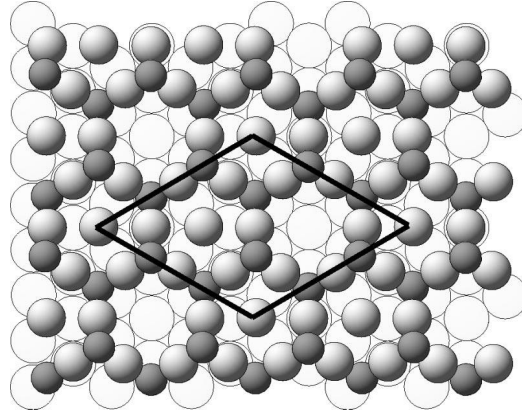


Figure 7.5: Figure taken from Ref. [134]. Shown is the  $p(4 \times 4)$  surface oxide forming on the Ag(111) surface. The unit cell is indicated. Oxygen atoms are represented by small dark circles. Silver atoms of the oxide layer are indicated by grey circles. The white circles represent the Ag(111) substrate.

uated phase boundaries would have to follow lines of constant oxygen chemical potential, which is the single determining quantity if thermodynamics applies. It was pointed out in the preceding discussion, that lines of constant chemical potential are always parallel to the phase boundaries, as shown in the theoretical diagram. For the bulk/surface oxide boundary drawn in Fig. 7.4 (left) (even considering all uncertainties) this is clearly not the case.

Similarly, the observation of the  $p(2 \times 2)$  adsorbate phase in experiment, which according to theory is never a thermodynamically stable phase, might be a sign of kinetic hindrance to the formation of the  $(\sqrt{5} \times \sqrt{5})R27^\circ$  phase. For comparative reasons, the corresponding line has also been marked in the theoretical plot, i.e. dashed line in the right part of Fig. 7.4, denoting the area, where the  $p(2 \times 2)$  would turn out more stable than the clean surface, if the surface oxide can not form.

It would be interesting to compare the results obtained for the stability of various O/Pd phases on the (100) and (111) surfaces of palladium, to the situation on Ag(111). The atomic structure of the surface oxide identified on the Ag(111) surface [5] is shown in Fig. 7.5. The surface oxide is a commensurable  $p(4 \times 4)$  oxide phase. The structure has been termed " $(4 \times 4)$ ", because the area of the  $(\sqrt{3} \times \sqrt{3})R30^\circ$  surface unit cell is practically four times that of clean  $(1 \times 1)$ -Ag(111). The difference in the length of the lattice vectors is 1.2% [134]. Although the (mentioned) *surface unit cells* are commensurable, the positions of the Ag atoms within the  $(\sqrt{3} \times \sqrt{3})R30^\circ$  oxide surface cell are, all except one, incommensurable with those of the Ag(111) surface.

The surface oxide consists of a "O-Ag-O" trilayer and has a ring-like structure.

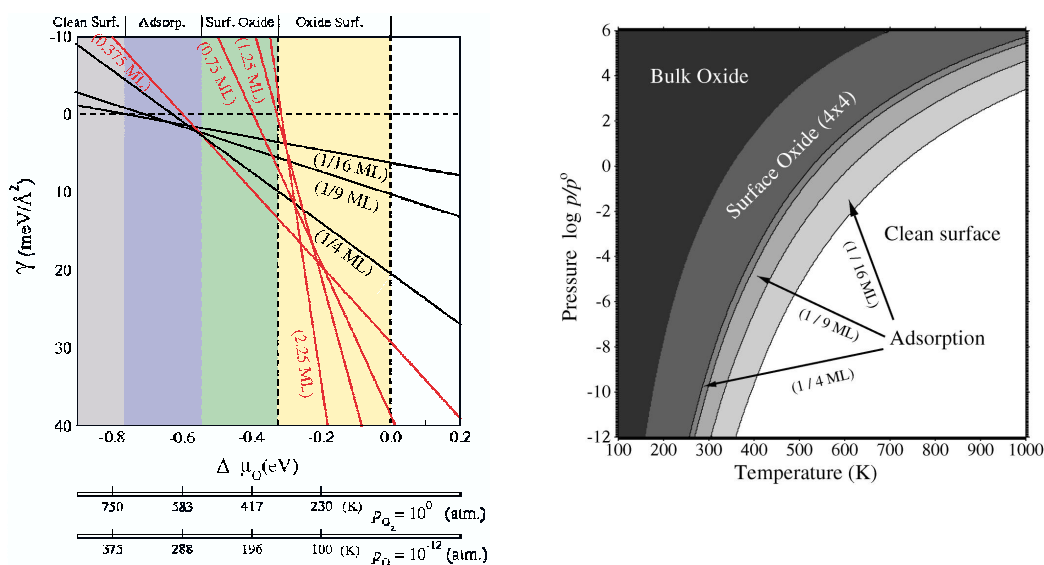


Figure 7.6: Figures taken from Ref. [110]. Left: Gibbs free energy of adsorption for various low energy O/Ag structures on the Ag(111) surface as a function of the O chemical potential. The labels "0.75 ML", "1.25 ML", and "2.25 ML" indicate the O-concentrations in the corresponding oxide-like structures. The  $(4 \times 4)$  structure has the label "0.375" ML. Right: Phase diagram for O at Ag(111) as a function of pressure and temperature, showing the stable structures.

Its structure is very similar to a trilayer of  $\text{Ag}_2\text{O}(111)$  [110], except there is one atom missing in the indicated cell (cf. Fig. 7.5). This missing atom would have been located directly on top of the Ag atom in the (111) surface below.

The stability plot of different O/Ag(111) phases and the corresponding phase diagram, shown in Fig. 7.6, are taken from Ref. [110]. As one would expect from the previously discussed Pd cases, at low oxygen chemical potentials the clean Ag(111) surface is the most stable phase. With increasing  $\mu_{\text{O}}$  eventually a low coverage (1/16 ML) of oxygen on the surface in fcc-hollow sites becomes thermodynamically more stable than the clean surface. It is followed by a  $\theta = 1/9$  ML and a  $\theta = 1/4$  ML structure, before the surface oxide becomes stable. The  $(4 \times 4)$  surface oxide phase is labeled "0.375 ML" (according to its oxygen coverage) and is observed in the range  $-0.54 \text{ eV} \leq \Delta\mu_{\text{O}} \leq -0.325 \text{ eV}$ . One should notice, that the stability range of the surface oxide *exceeds* the one of the bulk oxide, as was also seen for surface oxides on palladium. Interestingly, an investigation of the stability of various intermediate precursors suggested in the oxidation pathway from Ru(0001) to  $\text{RuO}_2(110)$  revealed no range of oxygen chemical potentials for which they might be stable [135]. Therefore one could tentatively expect that surface oxides play a thermodynamic role more for the  $4d$  transition metals towards the right of the periodic table, where the decreasing thermal stability of the

bulk oxides and the lowered bulk modulus of oxide and metal phase enhance the influence of the oxide coupling to the metal substrate. The result is a tendency to form commensurable, though possibly non-bulk like surface oxides.

A transformation of the stability plot for Ag(111) into a  $(T, p)$  phase diagram (cf. Fig. 7.6 (right)), shows that the surface oxide is stable in a temperature range of 350-530 K and atmospheric pressure ( $p = 1$  atm), while the di-silver oxide is stable up to 350 K. Therefore it was concluded [134] that the bulk oxide cannot possibly be the active phase for industrial reaction of ethylene epoxidation, which take place at higher temperatures. The surface oxide on the other hand is stable exactly in such a region, therefore it is suggested that it might be an actuating the reaction.

Similarly, for Pd the stability of the surface oxide on the (100) surface, i.e. the  $(\sqrt{5} \times \sqrt{5})R27^\circ$  structure approaches the region relevant for CO oxidation, in contrast to the bulk phase. Therefore it might be possible, that it is an active phase for this reaction. To draw, however, such a conclusion one has to perform further investigation. The first one of which would be to study the surface oxide stability in a O + CO atmosphere.

In conclusion, it must be stressed that the method of *ab-initio* thermodynamics is a powerful tool, which makes it possible to discern relevant structures and the conditions under which they are accessible. One should, however, always keep in mind that it is based on the assumption of thermodynamic equilibrium between the surface and the surrounding gas phase, the validity of which has to be verified. The assumption of thermodynamic equilibrium can also lead to deviations between experimental findings and theoretical predictions, as has been demonstrated for the  $(T, p)$ -phase diagram of Pd(100).



# Chapter 8

## Conclusions and outlook

At the time when this work started, knowledge about the oxidation behaviour of the late  $4d$  transition metals was quite limited. The focus from metal surfaces towards oxide structures, as being the ones important for CO oxidation catalysis, had just shifted. The result is a number of studies, both experimental and theoretical, devoted to the O adsorption or O + CO co-adsorption on the surfaces of different metals, which have emerged in recent years.

This work aims to give a comprehensive study of the oxygen-palladium interactions and gain insight into the formation of oxides on the Pd (100) and (111) surfaces. It is very fortunate that studies concerning the oxygen behaviour on Ru(0001), Rh(111) and Ag(111) were already available or evolved simultaneously to the work on palladium. The possibility to compare the findings on this four materials is beneficial not only for the understanding of oxide formation on palladium, but also sheds light onto the oxide formation of this sequence of elements. Comparing the relative stability of possible adsorbate structures on the basal plane of palladium, leads to the realisation that oxygen incorporation into palladium, starts already at sub-monolayer coverages. This incorporation goes hand in hand with a significant distortion of the lattice, which is less costly for a relatively soft material like palladium, but much harder for ruthenium. Consequently, O incorporation into the sub-surface region will commence at progressively lower coverages for the late  $4d$  transition metal sequence from Ru to Ag, implying a correlation between the oxidation behaviour and material properties, such as the cohesive energy or bulk modulus. The obtained coverage for each of this elements is very similar to the one, above which the oxide phase becomes thermodynamically more stable than chemisorbed O adlayers. This makes the role of sub-surface O as a metastable precursor during the oxide formation on them cognizant.

This role of the sub-surface oxygen is probably also the reason, why oxide formation on the more open (100) surface of palladium is found to be thermodynamically easier to accomplish compared to the basal surface. The  $(\sqrt{5} \times \sqrt{5})R27^\circ$  surface oxide structure observed on Pd(100) is identified as a strained, but commensurable PdO(101) thin film. It is stabilised by a strong coupling to the

substrate, which makes it comprehensible, that the stability region of the *surface* oxide exceeds the one of *bulk* PdO oxide. Still, it is surprising, that it is thermodynamically even more stable than the O ad-layers. It is interesting to notice that the binding energy of the on-surface oxygens in this structure is quite close to the calculated average O binding energy for it. As both lie in a medium range this might be useful for oxidation catalysis, as stated by the principle of Sabatier. It is therefore interesting to study the adsorption of CO on this surface oxide. Such a study might help to explain the oscillatory CO oxidation behaviour observed on the Pd(100) surface [2]. The observed roughening and smoothening of the surface, are attributed to the oxide and to the clean surface, respectively. That the increase in the CO oxidation rate coincides with the roughening of the surface, and drops as it becomes smooth once more, might indicate that the surface oxide is reduced and oxidised in turn. It may even be that the oxide is formed on one side of the Pd(100) surface and simultaneously reduced on a different side, in agreement with the wave fronts seen in experiment.

The different stability range of surface oxides on Pd(111) and Pd(100) which is the outcome of the thermodynamic study, is another intriguing detail to be considered. These two surfaces form the predominant surface area of Pd nanoparticles [136], which may have far reaching consequences for the oxidation behaviour of the latter. It might well be, that under certain  $(T, p)$ -conditions the active phase for CO oxidation could be on-surface adphases on some facets and surface oxides on others. Such a situation can make the overall kinetic data quite complex and the attempt to model such behaviour very challenging. One will have to go, for sure, at least beyond the thermodynamic approximations, used so far, and employ e.g. kinetic Monte Carlo.



# Appendix A

## Basis set tests

All the calculations in this work are performed using the full-potential linearised augmented plane wave method (FP-LAPW), described in chapter 2, as implemented into the WIEN97 program package. The use of a finite basis set requires careful testing of the different parameters, which determine its quality. Hereby one has to strive for the minimal set, which will give acceptable results, since this makes calculations even of comparatively large systems feasible and, besides, saves computer time.

There are, of course, numerous parameters one can think of, but typically only a few of them have a significant influence on performance and quality. The main parameters which have to be tested are:

- k-point set: the number of irreducible k-points within the Brillouin zone (BZ), needed to describe the dispersion of the bands.
- energy cutoff: In the interstitial region both the wave function and the potential are expanded in a plane wave bases (cf. eq. (2.38) and eq. (2.39)), which should be infinite in the ideal case. Since this is not possible in practice, a reasonable truncation point is determined. Consequently, the convergence of the basis set is dependent on this cutoff parameters -  $E_{\text{wf}}^{\text{max}}$  for the wave function and  $E_{\text{pot}}^{\text{max}}$  for the potential expansion.
- angular momenta: Inside the muffin-tin spheres the wave functions and the potential are expanded in spherical harmonics, which means that angular momenta come into play. These are:
  - $l_{\text{max}}^{\text{wf}}$  - maximum number of angular momenta for the wave functions inside the spheres,
  - $l_{\text{ns}_{\text{max}}}^{\text{wf}}$  - maximum number of angular momenta for off-diagonal matrix elements in the Hamiltonian,
  - $l_{\text{max}}^{\text{pot}}$  - maximum number of angular momenta for the potential inside the spheres.

$E_{\text{pot}}^{\text{max}}$	$l_{\text{max}}^{\text{pot}}$	$l_{\text{max}}^{\text{wf}}$	$l_{\text{nsmax}}^{\text{wf}}$	$E_{\text{wf}}^{\text{max}}$	irred. k-points
100 Ry	4	10	4	13 Ry	20/35/72
100 Ry	6	12	6	13 Ry	20
169 Ry	4	10	4	13 Ry	20
169 Ry	6	12	6	13 Ry/ 13 Ry, 16 Ry	20/72

Table A.1: Combinations of basis set parameters used for the determination of the equilibrium lattice constant, for both GGA and LDA.

For the surface calculation additionally the thickness of the slab and of the vacuum region are of profound importance. Consecutive slabs have to be decoupled, which requires a certain thickness of the vacuum region. On the other hand, this region should not be unproportionally thick, as this will slow down the calculation and influence the size of matrix.

### A.0.1 The bulk calculations

Palladium has a fcc-lattice, which make the usual bulk calculations quite simple and rather fast. Therefore, one can afford to test some of the mentioned parameters extensively.

In a first step the equilibrium lattice constant of palladium is determined. The experimental value for the lattice constant is 3.89 Å. It is expected, that the theoretical lattice constant is not too far away from this value. For this reason, self-consistent calculations for lattice constants, some of which are smaller and other bigger compared to the experimental value, are performed. For the GGA calculation  $a$  is varied from 3.60 Å up to 4.30 Å in 0.05 Å steps. For the LDA calculation the range is 3.50 Å to 4.20 Å, once more using 0.05 Å steps. A muffin-tin radius of  $R_{\text{MT}}(\text{Pd}) = 2.37a_0 = 1.25 \text{ \AA}$  is used.

Several combination of the above described basis set parameters are used, for both LDA and GGA, to determine the equilibrium lattice constant. They are listed in Table A.1. For each case the equilibrium lattice constant and bulk modulus are determined, using the Murnaghan equation of state. For LDA the values varied between 3.836 Å and 3.842 Å, while the bulk modulus was in the range 220 GPa to 228 GPa. For GGA  $a_0$  was in between 3.950 Å and 3.943 Å and the bulk modulus 162 GPa to 167 GPa. For further calculations the values mentioned in Chapter 3, i.e.  $a_0(\text{LDA}) = 3.838 \text{ \AA}$  and  $a_0(\text{LDA}) = 3.944 \text{ \AA}$ , are used.

The value of the lattice constant is influenced mainly by the different k-points and the different cutoffs for the wave function in the interstitial  $E_{\text{wf}}^{\text{max}}$ . The change in angular momenta and of the potential cutoff  $E_{\text{pot}}^{\text{max}}$  hardly play a role. To determine the best values for the wave function cutoff,  $E_{\text{wf}}^{\text{max}}$ , and the number of k-points, self-consistent calculations are performed for either of them. This can be done in two ways. Such calculations can be performed either for two different

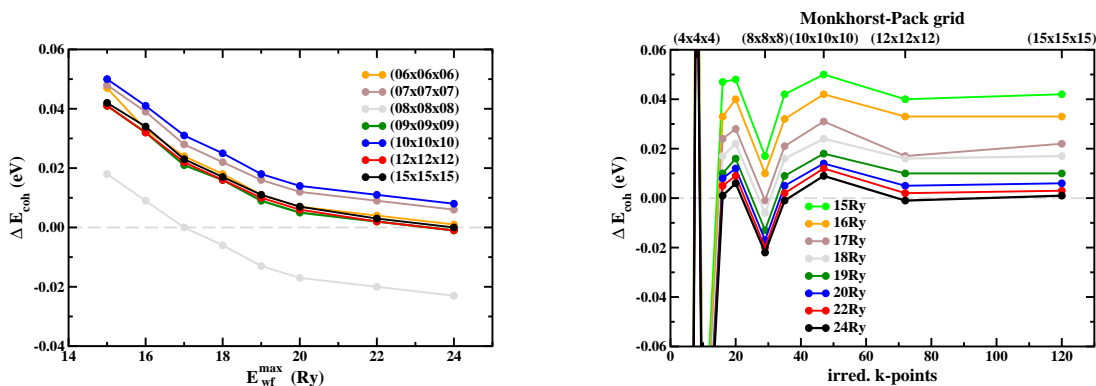


Figure A.1: The cohesive energy of palladium as a function of coverage (left) and of k-points (right). Shown is change with respect to the "overkill" value, i.e. k-points in a  $(15 \times 15 \times 1)$  MP grid and  $E_{\text{max}}^{\text{wf}} = 15\text{Ry}$ ,  $E_c = 3.64\text{eV}$ .

lattice constants and then the difference in total energy as a function of either  $E_{\text{wf}}^{\text{max}}$  or k-points can be plotted to determine the convergence threshold. Typically, the convergence of total energies relative to each other, as seen by such a plot, is much faster, compared to the mere convergence of a total energy alone. The second possibility is to determine the convergence of a physical quantity, e.g. the cohesive energy, with respect to the parameter set. Both ways are employed in the present work.

Calculations for lattice constants  $a_1 = 3.88\text{Å}$  and  $a_2 = 3.89\text{Å}$  are performed. Hereby  $E_{\text{pot}}^{\text{max}} = 169\text{Ry}$ ,  $l_{\text{max}}^{\text{pot}} = 6$ ,  $l_{\text{max}}^{\text{wf}} = 12$  and  $l_{\text{nsmax}}^{\text{wf}} = 6$  are used. The k-points variation is performed for  $E_{\text{wf}}^{\text{max}} = 9.68\text{Ry}$  and the wave function cutoff is tested for a  $(7 \times 7 \times 1)$  MP grid, corresponding to 20 k-points in the irreducible part of the BZ. In such a way it was determined that  $E_{\text{wf}}^{\text{max}} \geq 9.68\text{Ry}$  and  $k_{\text{irr.}} \geq 20$  are sufficient for the change in the total energy difference to be less than 5 meV.

It became necessary to reduce the muffin-tin radius to  $R_{\text{MT}} = 2.25 a_0 = 1.19\text{Å}$ , in order to perform calculations for the Pd(111) surface. For this reason, the same tests are also performed with the latter radius. Thus it is determined, that the wave function cutoff has to be increased, i.e.  $E_{\text{wf}}^{\text{max}} \geq 13.3\text{Ry}$ , to achieve the same accuracy.

The result of the tests performed to determine the convergence of the cohesive energy (for  $R_{\text{MT}} = 2.25 a_0$ ) are shown in Fig. (A.1). To make the plots easier to read, the calculated cohesive energy values are given with respect to the value determined in the best ("overkill") calculation, i.e. 120 k-points in the irreducible part of the BZ and  $E_{\text{max}}^{\text{wf}} = 15\text{Ry}$ , which is  $E_c = 3.64\text{eV}$ . The first thing that is noticeable is that the convergence of the cohesive energy with either wave function cutoff or k-points is worse, compared to the difference in total energies. It is due to the description of the Pd-atom, the energy of which was determined in a box with side length  $(13 \times 14 \times 15) a_0$ , a k-point at  $(1/2; 1/2; 1/2)$  and ROOT

parameter	clean Pd(111) surface and O/Pd(111) system	clean Pd(100) surface and O/Pd(100) system
$R_{MT}(Pd)$	$2.25 a_0$	$1.80 a_0$
$R_{MT}(O)$	$1.30 a_0$	$1.30 a_0$
$l_{\max}^{\text{wf}}$	12	12
$l_{\text{ns}_{\max}}^{\text{wf}}$	6	6
$l_{\max}^{\text{pot}}$	4	4
$E_{\text{wf}}^{\max}$	17 Ry	20 Ry
$E_{\text{pot}}^{\max}$	169 Ry	169 Ry
MP grid; $k_{ir}$ for $(1 \times 1)$ u.c.	$(12 \times 12 \times 1)$ ; 19	$(12 \times 12 \times 1)$ ; 28
MP grid; $k_{ir}$ for $(2 \times 2)$ u.c.	$(6 \times 6 \times 1)$ ; 7	$(6 \times 6 \times 1)$ ; 6
MP grid; $k_{ir}$ for surface oxide	-	$(4 \times 4 \times 1)$ ; 8

Table A.2: The basis set parameters used for calculations of the palladium (111) and (100) surfaces.

sampling, used for the k space integration. To calculate the cohesive energy the value of both the bulk and the "atom in a box" are taken at the same  $E_{\max}^{\text{wf}}$  value. From the dependence of  $E_c$  on the k-points it can be concluded, that either  $E_{\max}^{\text{wf}} = 19$  Ry and  $(9 \times 9 \times 9)$  MP-grid or  $E_{\max}^{\text{wf}} = 17$  Ry and  $(12 \times 12 \times 12)$  MP-grid are sufficient for the cohesive energy to be converged to within 20 meV of the overkill value. On the other hand, that plot of the cutoff dependence shows that either  $E_{\max}^{\text{wf}} = 19$  Ry and  $(10 \times 10 \times 10)$  MP-grid or, once again,  $E_{\max}^{\text{wf}} = 17$  Ry and  $(12 \times 12 \times 12)$  MP-grid, is enough to be within the same range. Therefore, one can conclude that  $E_{\max}^{\text{wf}} = 17$  Ry and  $(12 \times 12 \times 12)$  MP-grid is a good combination to use.

### A.0.2 The surface calculations

The basis set parameters used for the calculations of both the Pd(111) and Pd(100) clean and adsorbate/surface oxide covered surface, are listed in Table A.2. For each the generalised gradient approximation (GGA-PBE) [50] is used for the exchange-correlation functional. The 4s and 4p semi-core states of Pd, as well as the O 2s are described by local orbitals. To improve the convergence a temperature broadening of 70 meV with a Fermi function is used to calculate the Fermi energy,  $E_F$ . The influence of the different "smearing" methods was tested for the bulk calculation, but is found to be of no consequence for the obtained results at all.

The Pd(111) surface is modeled by a 7 layer palladium slab and a 17 Å thick vacuum region. The 7 layer slab ensures, that there are 5 palladium layers in between oxygen atoms in sub-surface positions.

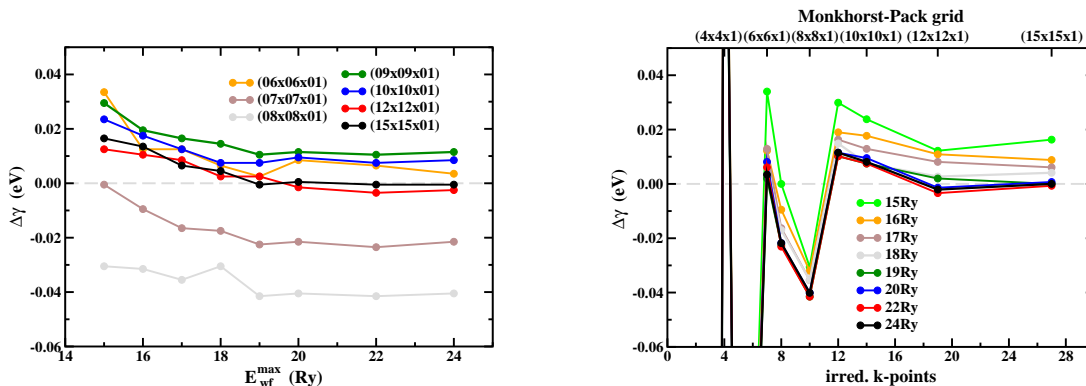


Figure A.2: The surface energy of palladium as a function of coverage (left) and of k-points (right). Shown is change with respect to the "overkill" value,  $E_s = 0.59$  eV.

The Pd(100) surface is modeled by a 5 layer palladium slab and  $\approx 15$  Å vacuum ensure the decoupling of the surfaces of consecutive slabs. For the modeling of the  $\sqrt{5}$  the various PdO layers are added on either side of the five layers Pd(100) slab.

It was already mentioned in Chapter 4 that a central quantity obtained from a DFT calculation is the binding energy. It should be noted, that the calculation of  $E_b$  involves the total energies of the O-metal system,  $E_{O@M}$ , the clean metal slab,  $E_M$ , and of an isolated oxygen molecule. Each of these energies depends on the quality of the basis set. To assess this quality, and judge the extend of the error due to the approximations made during the calculation, one has to carefully test different parameters of the basis set. As the repulsion between the oxygen atoms increase with coverage, the two extremes one is faced with are the clean surface, bereft of any O, and the completely oxygen covered surface, i.e. 1 ML. The convergence of sub-monolayer coverage cases, is expected to lay in between. Therefore, the clean and the 1 ML O covered surface are discussed in the following.

One characteristic feature of the clean surfaces is the surface energy. Consequently, the convergence of  $\gamma$  with coverage and k-points is determined. The results for the surface energy of the Pd(111) surface are shown in Fig.A.2. To make the k-points sampling in reciprocal space comparable, the bulk calculations are performed for a crystal with a (111) orientation. The surface energy in each point is determined by using the total energies of a slab and a bulk, calculated with the same basis set, i.e. same cutoff, k-points, angular parameters etc. For either  $E_{wf}^{max}$  or k-points,  $\gamma \leq 0.02$  eV compared to the best value, is achieved for  $E_{wf}^{max} = 16$  Ry and 12 irreducible k-points, corresponding to a  $(9 \times 9 \times 1)$  MP grid. The error is reduced to  $\gamma \leq 0.01$  eV for  $E_{wf}^{max} = 17$  Ry and  $k_{ir.} = 19$ , i.e. a  $(12 \times 12 \times 1)$  MP grid.

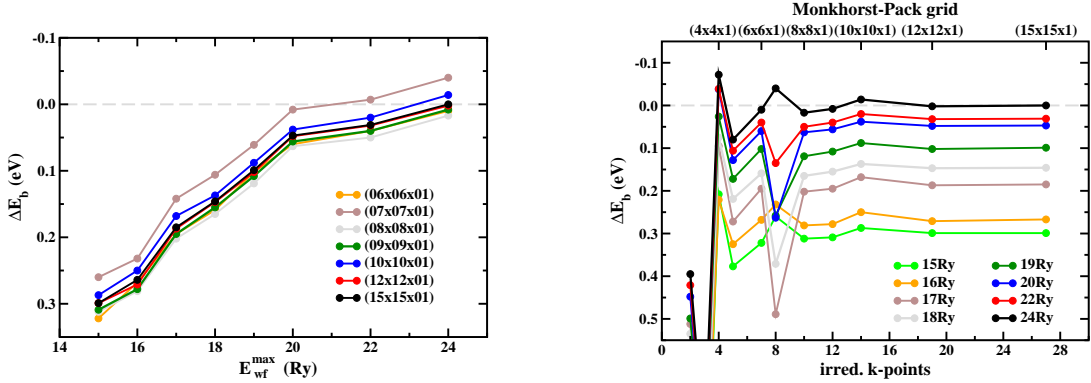


Figure A.3: Binding energy for  $O(1 \times 1)/Pd(111)$  as a function of coverage (left) and of k-points (right). The change in binding energy for 1.0 ML O adsorbed in fcc site is shown with respect to the "overkill" value,  $E_b = 0.16$  eV.

For the surface covered with oxygen atoms, the convergence of the average binding energy as a function of wave function cutoff and k-points sampling is studied, since this is one of the main quantities of interest, after all. The results for the  $(1 \times 1) - O_{fcc}/Pd(111)$  structure are shown in Fig. A.3. The same basis set is used to calculate  $E_b$  in each point. It is seen that the absolute value of the binding energy is  $E_b < 0.2$  eV for  $E_{wf}^{max} = 17$  Ry and  $k_{ir.} = 19$ , i.e. a  $(12 \times 12 \times 1)$  MP grid. This value is, however reduced to  $E_b < 0.02$  eV, if one considers the difference between the binding energy of the  $(1 \times 1) - O/Pd(111)$  structure with the oxygen atom adsorbed once in fcc and once in hcp place, as seen in Fig. A.4. As the main error is introduced by the DFT description of the atomic and molecular oxygen, a possible error cancellation is least effective for the absolute value of the binding energy, as can be seen from the above. Density-functional theory, even within the GGA, is known to poorly describe gas phase oxygen and gives in particular the binding energy for molecular oxygen  $O_2$  wrong by about 0.5 eV per oxygen atom [35].

Due to the small bondlength the energy of the oxygen molecule cannot be calculated directly with a muffin-tin radius of  $R_{MT}^O = 1.3$  bohr, chosen in the surface calculations. Therefore, one makes use of the relationship for  $E_{O_2}$ ,

$$E_{O_2} = 2E_O + D, \quad (A.1)$$

where  $D$  is the dissociation energy of the  $O_2$  molecule. To determine this energy one has to calculate both the energy of an oxygen atom on its own and the dissociation energy of the oxygen molecule.

The energy of the isolated oxygen atom is computed in a cell with sides  $(13 \times 14 \times 15)$  bohr, to avoid spherical averaging of the electron density of the O atom. The k-point at  $(1/2; 1/2; 1/2)$  is used for the sampling of the Brillouin zone. The total energy is computed for  $E_{wf}^{max}$  from 15 Ry to 24 Ry. For the determination of

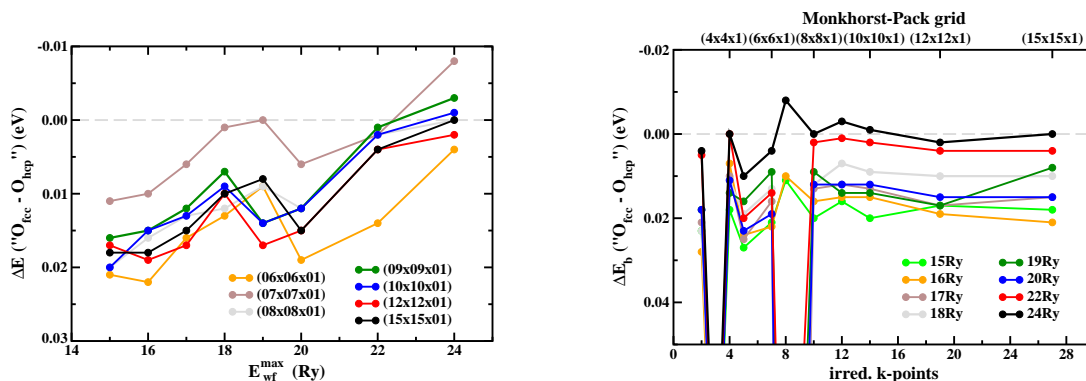


Figure A.4: Dependence of the difference in binding energy between O adsorbed in fcc site and hcp site for the O(1 × 1)/Pd(111) as a function of coverage (left) and of k-points (right). The value of the "overkill" calculation is taken, once again, as reference.

the  $E_b$  the value at the according wave function cutoff is used.

The molecular binding energy  $D$ , on the other hand, is determined employing a smaller  $R_{\text{MT}}^{\text{O}}$  of 1.1 bohr within a (13 × 14 × 18) bohr unit cell (again avoiding spherical averaging) and using  $\Gamma$ -point sampling<sup>1</sup>. Due to the smaller muffin-tin radius the kinetic-energy cutoff for the plane-wave basis needed for the interstitial region has been increased to 34 Ry. Thus the dissociation energy of the oxygen molecule is determined to be  $E_b = 3.101$  eV/O atom.

As the poor description of the oxygen molecule directly affects the binding energies of the various structures investigated in this work, it is interesting to consider if there is a workaround this problem. Following the approach of Li *et al.* [100], it is possible to determine the total energy of molecular oxygen,  $E_{\text{O}_2}^{\text{tot}}$ , not via gas phase calculations, but by employing the approximate equation for the PdO heat of formation,  $\Delta H_f$ , into which only the total energies of bulk PdO and Pd bulk,  $E_{\text{PdO,bulk}}^{\text{tot}}$  and  $E_{\text{Pd,bulk}}^{\text{tot}}$ , enter, i.e.,

$$1/2E_{\text{O}_2}^{\text{tot}} \approx E_{\text{PdO,bulk}}^{\text{tot}} - E_{\text{Pd,bulk}}^{\text{tot}} + \Delta H_f(300\text{K}, 1\text{atm}). \quad (\text{A.2})$$

At the expense of discarding a completely first-principles type description, one can use the experimental  $\Delta H_f(300\text{K}, 1\text{atm})$  and thus arrive at  $E_{\text{O}_2}^{\text{tot}}$  without having to resort to atomic calculations. Throughout the work only the stability of various structures all including the same number of oxygen atoms is compared. This means, that the difference between the standard computation of binding energies, i.e. by using the gas-phase computed  $E_{\text{O}_2}^{\text{tot}}$  and the value obtained from eq. A.2 will result in a constant shift in the calculated  $E_b$ . With  $\Delta H_f^{\text{exp}}(300\text{K}, 1\text{atm}) = 0.88$  eV<sup>2</sup> [132], this shift amounts to 0.43 eV per O atom

<sup>1</sup>The calculation of the molecular binding energy was performed by J. Rogal.

<sup>2</sup>The value determined from DFT [99] is  $\Delta H_f = 0.869$  eV. Therefore, it hardly matters (in this case), which value one uses.

Structure	$k_{\text{ir}} = 8; E_{\text{wf}}^{\text{max}} =$				$k_{\text{ir}} = 18$
	15 Ry	17 Ry	20 Ry	24 Ry	$E_{\text{wf}}^{\text{max}} = 20 \text{ Ry}$
PdO(101)/Pd(100) (a)	0.99	1.53	1.36	1.32	1.37
PdO(101)/Pd(100) (b)	1.12	1.92	1.74	-	-
PdO(100)/Pd(100)	0.53	1.04	0.92	-	0.92
PdO(001)/Pd(100)	-0.16	0.44	0.32	-	-

Table A.3: The average binding energy of the relaxed geometries of different structure models considered for the  $(\sqrt{5} \times \sqrt{5})R27^\circ\text{-O}$  surface oxide on the Pd(100) surface, for various wave function cutoffs,  $E_{\text{wf}}^{\text{max}}$ , and k-points. PdO(101)/Pd(100) (a) corresponds to a 5 Pd layer slab in the middle plus a PdO(101) layer on both sides, while for PdO(101)/Pd(100) (b) 7 Pd layers are sandwiched between the PdO(101) layers on both sides of the slab. For the two other structures 3 Pd layers plus the oxide layer, i.e. PdO(100) or PdO(001), are used.  $k_{\text{ir}} = 8$  corresponds to a  $(4 \times 4 \times 1)$  MP grid, and  $k_{\text{ir}} = 18$  corresponds to a  $(6 \times 6 \times 1)$  MP grid.

with a lower stability of the  $\Delta H_f$ -derived binding energies and not including zero-point vibrations. This indicates the sizable uncertainty in the absolute binding energy values and correspondingly dictates a cautious judgment on the endo- or exothermicity of a structure. The determination of the binding energy is then likely to represent an upper limit to the real stability of the different considered structures.

An increase of the potential expansion up to  $l_{\text{max}}^{\text{pot}} = 6$  was also considered, but it hardly affected the relative binding energies. What remains to be estimated, is the error due to the finite slab size and size of the vacuum region. To this end the vacuum region is increased from 15 eV to 20 eV, but the change in the absolute binding energy is just 0.02 eV. To appraise the thickness of the slab, calculations for slabs with 5 to 11 layers with 1 ML oxygen atoms were performed. Although the absolute binding energies are lowered by up to 65 meV, the obtained  $\Delta E_b$  are within  $\pm 30$  meV.

For the (100) surface of palladium, the above described basis set results in a very good agreement with the structure determination of the  $p(2 \times 2)$  phase reported by a LEED study [111]. As the main concern are the surface oxide structures, several test were performed to assess the convergence of the average binding energy per O atom with respect to the basis set parameters. Of these, the PdO(101)/Pd(100) structure, is the most thorough tested one. The calculated binding energy for various structural models considered for the  $(\sqrt{5} \times \sqrt{5})R27^\circ\text{-O}$  surface oxide on the Pd(100) surface are listed in Table A.3. Each structure is relaxed, so that the forces on the atoms are  $\leq 5 \text{ mRy/a.u.}$ . It can be seen that regardless of the structure, the average binding energy changes by 0.2 eV when the wave function cutoff is increased from 17 Ry to 20 Ry and by only 0.04 eV when it is further



increased to 24 Ry for the PdO(101)/Pd(100) structure. Concerning the k-points, there is almost no a change in  $E_b$  between  $k_{\text{ir}} = 8$  ( $(4 \times 4 \times 1)$  MP grid) and  $k_{\text{ir}} = 18$  corresponds to a  $(6 \times 6 \times 1)$  MP grid.

An increase of the slab thickness has a greater effect on the value of the average binding energy, but does not affect the evolvement with  $E_{\text{wf}}^{\text{max}}$ , nor the relative stability of the different structures with respect to each other. (For the PdO(001)/Pd(100) a thicker slab was also considered, but not relaxed thoroughly).

Accounting for all these tests a conservative estimate of  $\pm 50$  meV for the numerical uncertainty when comparing relative binding energies can be given. The relative energetic stabilities of the various tested overlayer models on the Pd(100) surface are also converged to within  $\pm 50$  meV per O atom. As this error affects neither the evolvement of  $E_b(\theta)$  with coverage nor the energetic sequence among considered structures, it has no influence on the physical conclusions.



# Appendix B

## STM simulations

During the course of this work the necessity arose to perform STM simulations. To be able to do so, some existing programs in the WIEN package had to be modified and an additional, comparatively small program had to be written, to evaluate the electron density using the Tersoff-Hamann approach.

### B.1 LAPW5

So far it was only possible to determine the electron density in one (specified) plane, using the LAPW5 program from the WIEN package. To perform an STM simulation one needs information about the electron density in three dimensions. Therefore the program LAPW5 was modified in such a way, that makes the determination of the electron density in a set of parallel planes (at different height) possible. Thereby one gets information about the electron density in  $x$ -,  $y$ - and  $z$ -directions. In the following the different changes made to parts of LAPW5 are described.

- **param.inc** file  
An additional parameter was added to the param.inc file: **NZDIM**. This is a dimensioning parameter for the number of points in  $z$ -direction, therefore its value should be at least as big as the number of points one would like to consider for the  $z$ -direction.
- **case.in5** file In the case.in5 file (an input file for LAPW5) the extension of the planes and their number is specified. This file needs to have the form shown in Table B.1. The modifications with respect to the input file needed for the original version of the program, are highlighted.

line 1-4: four points in the unit cell (origin,  $x$ -end,  $y$ -end,  $z$ -end), specifying the volume, in which electron density will be calculated. In the original LAPW5 program, only 3 such points were needed (origin,  $x$ -end,  $y$ -end).

0 0 2 3	# x, y, z, divisor of origin
3 0 2 3	# x, y, z, divisor of x-end
0 3 2 3	# x, y, z, divisor of y-end
<b>0 0 3 3</b>	# x, y, z, divisor of z-end
4 3 3	# number of shells
10 10 <b>90</b>	# number of points in x,y and z dir, # (ratio close to lenght ratio)
RHO	# RHO—DIFF—OVER; ADD—SUB or blank
ANG VAL NODEBUG	# ANG—ATU; VAL—TOT; DEBUG—NODEBUG

Table B.1: The new **case.in5** file

line 6 : the number of  $x$ ,  $y$  and  $z$  grid points in the volume are specified. To determine the charge density only in one plane (as in the original LAPW5 program), the coordinates of the points (line 1-4) should have the same  $z$ -coordinate and just **1** point in  $z$ -direction should be considered.

The remaining part of the file, is not changed compared to the original input file. When more than one cell should be plotted, one has to make sure, that the number of  $x$  and  $y$  points in each cell is the same. For example, if one wants to use 9 points per cell and has in total 5 cells, the value, which has to be specified in case.in5 for the number of  $z$ -points is 41 (for each direction in a plane, i.e.  $x$  and  $y$ ). For the images simulated in chapter 6 approximately 1 point per 0.5 Å was used. Furthermore, the distance between the different planes in which the electron density was determined was 0.06Å. It was tested that increasing this values does not change the obtained images.

- **main1.f** file

In this subroutine the axes of the plot and the grid points are determined. Most modifications had to be made here.

In the following the some details about the changes made to this program, together with some explanations about their purpose, are described.

- **The following variables were modified or added:**

- \* VEC(3,4): its dimensions in the original programm were VEC(3,3)
- \* VZ(3):  $z$ -vector for the plot
- \* IZ(3):  $z$ -coordinate (height) of a plane

- **The origin and endpoints of the plot are determined**

So far only three points had to be specified in **case.in5**: for the origin, for the  $x$ -end and for the  $y$ -end of the plot. Now a fourth point must be added to consider the  $z$ -direction.

- **Gridpoints in plot are specified**

In the original program the grid, on which points the charge density was determined, had (**NPX** × **NPY**) points. In the changed version there are (**NPX** × **NPY** × **NPZ**) points.

- **Plot axis**

The plot area was determined just by two vectors in the original program. Now three vectors, defining the three axes of the plot are needed and have to be determined. The calculated vectors are written also to the output file, case.output5, thus one can make sure that the plotting area is indeed what one had in mind. The length of these vectors is also written in the case.output5 file.

- **prtrh.f** file

In this subroutine the charge density is transformed into a form suitable for plotting, i.e. multiplied with spherical harmonics. This subroutine was modified in such a way, that it now also considers the new dimension, when information about the electron density is read/ written from/to the output file **case.rho**. The electron density needed as input for the STM simulation program is contained in this file.

Now the electron density is available for each point on the three dimensional grid in a volume specified by the vectors given in case.in5. This information is then evaluated in the program STM, which reads out the height, at which the density becomes lower, than some threshold value. Therefore, this program enables one to draw a isosurface of constant density.

The receipt one has to follow to perform an STM-Simulation is the following:

- A converged calculation, i.e. a converged density is needed.
- The LAPW2 program has to be run once more to get a case.clmval file. Hereby, one should specify the energy window at the Fermi energy, in which the states should be determined.
- Run LAPW5 to get the electron density on the three dimensional grid.
- Simulate an STM-image by running STM.f  
 Input file: The STM.f program requires a file STM.rho as input, so one has to copy the case.rho file to STM.rho.  
 Output file: The output file is called STM.out and is suitable for plotting with XFarbe. If one wants to use another plotting program, it might be necessary to change the format of the output.



# Bibliography

- [1] H. Over, Y.D. Kim, A.P. Seitsonen, S. Wendt, E. Lundgren, M. Schmid, P. Varga, A. Morgante, and G. Ertl, *Science* **287**, 1474 (2000).
- [2] B.L.M Hendriksen, *Model catalyst in action - high-pressure scanning tunneling microscopy*, Ph.D. thesis, Universiteit Leiden, 2003.
- [3] E. Lundgren, G. Kresse, C. Klein, M. Borg, J.N. Andersen, M. De Santis, Y. Gauthier, C. Konvicka, M. Schmid, and P. Varga, *Phys. Rev. Lett.* **88**, 246103 (2002).
- [4] W.X. Li, C. Stampfl and M. Scheffler, *Phys. Rev. B* **65**, 075407 (2002).
- [5] C.I. Carlisle, D.A. King, M.-L. Bocquet, J. Cerdá, and P. Sautet, *Phys. Rev. Lett.* **84**, 3899 (2000).
- [6] P. Hohnberg and W. Kohn, *Phys. Rev. B* **136**, 846 (1964).
- [7] W. Kohn and L. Sham, *Phys. Rev. A* **140**, 1133 (1965).
- [8] C.M. Weinert and M. Scheffler, In: *Defects in Semiconductors*, H.J. von Bardeleben (Ed.), *Mat. Sci. Forum* **10-12**, 25 (1986).
- [9] M. Scheffler, In: *Physics of Solid Surfaces - 1987*, J. Koukal (Ed.), (Elsevier, Amsterdam 1988); M. Scheffler and J. Dabrowski, *Phil. Mag. A* **58**, 107 (1988).
- [10] E. Kaxiras, Y. Bar-Yam, J.D. Joannopoulos, and K.C. Pandey, *Phys. Rev. B* **35**, 9625 (1987).
- [11] G.-X. Qian, R.M. Martin, and D.J. Chadi, *Phys. Rev. B*, **38** 7649 (1988).
- [12] X.-G. Wang, W. Weiss, Sh.K. Shaikhutdinov, M. Ritter, M. Petersen, F. Wagner, R. Schlögl, and M. Scheffler, *Phys. Rev. Lett.* **81**, 1038 (1998).
- [13] X.-G. Wang, A. Chaka, and M. Scheffler, *Phys. Rev. Lett.* **84**, 3650 (2000).
- [14] K. Reuter and M. Scheffler, *Phys. Rev. B* **65**, 035406 (2002).

- [15] K. Reuter and M. Scheffler, *Phys. Rev. Lett* **90**, 046103 (2003).
- [16] X. Guo, A. Hoffman, and J.T. Yates Jr., *J. Chem. Phys.* **90**, 5787 (1989).
- [17] H. Conrad, G. Ertl, J. Küppers, and E.E. Latta, *Surf. Sci.* **65**, 245 (1977).
- [18] R. Imbihl and J.E. Demuth, *Surf. Sci.* **173**, 395 (1986).
- [19] B.A. Banse and B.E.Koel, *Surf. Sci.* **232**, 275 (1990).
- [20] P. Légaré, L. Hilaire, G. Maire, G. Krill, and A. Amamou, *Surf. Sci.* **107**, 533 (1981).
- [21] E.H. Voogt, A.J.M. Mens, O.L.J. Gijzeman, and J.W. Geus, *Surf. Sci.* **373**, 210 (1997).
- [22] A.P. Seitsonen, Y.D. Kim, S. Schwegmann and H. Over *Surf. Sci.* **468**, 176 (2000).
- [23] D. Loffreda, D. Simon, and P. Sautet, *J. Chem. Phys.* **108**, 6447 (1998).
- [24] J. Roques, C. Lacaze-Dufauer, and C.Mijoule, *Surf. Sci.* **479**, 231 (2001).
- [25] K. Honkala and K. Laasonen, *J. Chem. Phys.* **115**, 2297 (2001).
- [26] G. Zheng and E.I. Altman, *Surf. Sci.* **462**, 151 (2000).
- [27] G. Zheng and E.I. Altman, *Surf. Sci.* **504**, 253 (2002).
- [28] T.W. Orent and S.D. Bader, *Surf. Sci.* **115**, 323 (1982).
- [29] E.M. Stuve, R.J. Madix, and C.R. Brundle, *Surf. Sci.* **146**, 155 (1984).
- [30] S.-L. Chang and P.A. Thiel, *J. Chem. Phys.* **88**, 2071 (1988).
- [31] S.-L. Chang, P.A. Thiel, and J.W. Evans, *Surf. Sci.* **205**, 117 (1988).
- [32] D.T. Vu, K.A.R. Mitchell, O.L. Warren, and P.A. Thiel, *Surf. Sci.* **318**, 129 (1994).
- [33] M. Saily, O.L. Warren, P.A. Thiel, and K.A.R. Mitchell, *Surf. Sci.* **494**, L799 (2001).
- [34] C. Stampfl and M. Scheffler, *Phys. Rev. B* **54**, 2868 (1996).
- [35] M.V. Ganduglia-Pirovano and M. Scheffler, *Phys. Rev. B* **59**, 15533 (1999).
- [36] M. Born and J.R. Oppenheimer, *Ann. Phys.* **84**, 457 (1927).
- [37] A. Gross and M. Scheffler, *Phys. Rev. B* **57**, 2493 (1998).



- [38] D.R. Hartree, Proc. Camb. Philos. Soc. **24**, 328 (1928).
- [39] V.A. Fock, Z. Phys. **15**, 126 (1930).
- [40] A.Groß, *Theoretical surface science/A microscopic perspective*, Springer Verlag, Berlin, Heidelberg (2003).
- [41] W.M.C. Foulkes, L. Mitas, R.J. Needs, and G. Rajagopal, Rev. Mod. Phys. **73**, 33 (2001).
- [42] R.M. Dreizler and E.K.U. Gross, *Density functional theory: an approach to the quantum many-body problem*, Springer Verlag, Berlin (1990).
- [43] R.G. Parr and W. Yang, *Density functional theory*, Oxford University Press, New York (1989).
- [44] L.H. Thomas, Proc. Camb. Phil. Soc. **23**, 542 (1927).
- [45] E. Fermi, Rend. Accad. Lincei **6**, 602 (1927); E. Fermi, Z. Phys. **48**, 73 (1928); E.Fermi, Rend. Accad. Lincei **7**, 342 (1928).
- [46] M. Levy, Phys. Rev. A **26**, 1200 (1982).
- [47] C.-O. Almbladh and U. von Barth, Phys. Rev. B **31**, 3231 (1985).
- [48] J.F. Janak, Phys. Rev. B **18**, 7165 (1978).
- [49] D.M. Ceperley and B.J. Alder, Phys. Rev. Lett. **45**, 566 (1980).
- [50] J. Perdew, K. Burke, and M. Ernzerhof, Phys. Rev. Lett. **77**, 3865 (1996).
- [51] M. Payne, M. Teter, D. Allan, T. Arias, J. Joannopoulos, Rev. Mod. Phys. **64**, 1045 (1992).
- [52] G. Kresse, J. Furthmüller, Phys Rev B **54**, 11169 (1996).
- [53] J. Koringa, Physica **13**, 392 (1947).
- [54] W. Kohn and N. Rostoker, Phys. Rev. **94**, 1111 (1954).
- [55] O. Andersen, Phys. Rev. B, **12**, 3060 (1975).
- [56] H. Skriver, *The LMTO method: Muffin-tin orbitals and electronic structure*, Springer Verlag, Berlin (1984).
- [57] S. Savrasov and D. Savrasov, Phys. Rev. B **46**, 12181 (1992).
- [58] D.J. Singh, *Planewaves, Pseudopotentials and the LAPW method*, Kluwer Academic, Boston (1994).

- [59] J. Slater, Phys. Rev. B **51**, 846 (1937).
- [60] P. Blaha, K. Schwarz, and J. Luitz, **WIEN97**, *A Full Potential Linearized Augmented Plane Wave Package for Calculating Crystal Properties*, Karlheinz Schwarz, Techn. Universität Wien, Austria, (1999). ISBN 3-9501031-0-4.
- [61] J. Neugebauer and M. Scheffler, Phys. Rev. B **46**, 16067 (1992).
- [62] J. Rath and A. Freeman, Phys. Rev. B **11**, 2109 (1975).
- [63] H. Monkhorst and J. Pack, Phys. Rev. B **13**, 5188 (1976).
- [64] M. Scheffler, J.P. Vigneron, and G.B. Bachelet, Phys. Rev. Lett. **49**, 1765 (1982).
- [65] M. Scheffler, J.P. Vigneron, and G.B. Bachelet, Phys. Rev. **31**, 6541 (1985).
- [66] R. Yu, D. Singh, and H. Krakauer, Phys. Rev. B. **43**, 6411 (1991).
- [67] B. Kohler, S. Wilke, M. Scheffler, R. Kouba, and C. Ambrosch-Draxl, Comput. Phys. Commun. **94**, 31 (1996).
- [68] N.W. Ashcroft and N.D. Mermin, *Solid State Physics*, CBS Publishing, Asia Ltd, (1976).
- [69] C. Kittel, *Einführung in die Festkörperphysik*, R. Oldenbourg Verlag München Wien, John Wiley&Sons GmbH Frankfurt am Main (1973), p. 128
- [70] F. Birch, J. Appl. Phys. **9**, 279 (1938).
- [71] F.D. Murnaghan, Proc. Nat. Acad. Sci. **30**, 244 (1944).
- [72] J. da Silva, *The nature and behavior of rare-gas atoms on metal surface*, Dissertation, TU Berlin (2002).
- [73] J. Rogal, *Elektronenstruktur und Stabilität von Pd und PdO (Dichtefunctionaltheorierechnungen)*, Diplomarbeit, FU Berlin (2002).
- [74] R.I. Masel, *Principles of adsorption and reaction on solid surfaces*, John Wiley&Sons, New York (1996).
- [75] T.E. Felter, E.C. Sowa and M.A. Van Hove, Phys. Rev. B **40**, 891 (1989).
- [76] A. Barbieri, M.A. Van Hove and G.A. Somorjai, Surf. Sci. **306**, 261 (1994).
- [77] M.W. Finnis and V. Heine, J. Phys. F **4**, L37 (1974).

- [78] R. Smoluchowski, *Phys. Rev.* **60**, 661 (1941).
- [79] H. Ohtani, M.A. Van Hove and G.A. Somorjai, *Surf. Sci.* **187**, 372 (1997).
- [80] F. Maca, M. Scheffler and W. Berndt, *Surf. Sci.* **160**, 467 (1985).
- [81] K. Christmann, G. Ertl and O. Schober, *Surf. Sci.* **40**, 61 (1973).
- [82] K. Reuter, private communication; Basis set as described in *Phys. Rev. B* **65**, 165403 (2002).
- [83] M. Methfessel, D. Hennig, and M. Scheffler, *Phys. Rev. B* **46**, 4816 (1992).
- [84] N.D. Lang and W. Kohn, *Phys. Rev. B* **3**, 1215 (1971).
- [85] B.E. Nieuwenhuys, R. Bouwman and W.M.H. Sachtler, *Thin Solid Films* **21**, 51 (1974).
- [86] J.E. Demuth, *Chem. Phys. Lett.* **45**, 12 (1977).
- [87] M.C. Dejonquères, D. Spanjaard, *Concepts in Surface Physics*, Springer (1993).
- [88] A. Steltenpohl and N. Memmel, *Surf. Sci.* **443**, 13 (1999).
- [89] K. Reuter, M.V. Ganduglia-Pirovano, C. Stampfl, and M. Scheffler, *Phys. Rev. B* **65**, 165403(2002).
- [90] C. Stampfl, H.J. Kreuzer, S.H. Payen, H. Pfnür, and M. Scheffler, *Phys. Rev. Lett.* **83**, 2993 (1999).
- [91] B. Hammer and J.K. Nørskov, *Theory of adsorption and surface reactions*, in NATO ASI Series **E331**, R. Lambert and G. Pacchioni (Eds.), Kluwer Academic Publishers, Dordrecht (1997).
- [92] M. Scheffler and C. Stampfl, *Theory of adsorption on metal substrates*, Handbook of surface science, volume 2, K. Horn and M. Scheffler (Eds.), Elsevier (2000).
- [93] L.D. Schmidt and R. Gomer, *J. Chem. Phys.* **45**, 1605 (1966).
- [94] L.W. Swanson and R.W. Strayer, *J. Chem. Phys.* **48**, 2421 (1968).
- [95] Z. Sidorski, I. Pelly and R. Gomer, *J. Chem. Phys.* **50**, 2382 (1969).
- [96] L. Pauling, *The nature of the chemical bond*, 3rd ed. (Cornell University Press, Ithaca, NY, 1960; H.O. Pritchard and H.A. Skinner, *Chem. Reviews* **55**, 745 (1955)).

- [97] C.I. Carlisle, T. Fujimoto, W.S. Sim and D.A. King, Surf. Sci. **470**, 15 (2000), and references therein.
- [98] M.E. Grillo, M.V. Ganduglia-Pirovano, and M. Scheffler, (*unpublished results*).
- [99] J. Rogal, K. Reuter, and M. Scheffler, Phys. Rev. B **69**, 075421 (2004).
- [100] W.X. Li, C. Stampfl, and M. Scheffler, Phys. Rev. B **67**, 045408 (2003).
- [101] M. Todorova, E. Lundgren, V. Blum, A. Mikkelsen, S. Gray, J. Gustafson, M. Borg, J. Rogal, K. Reuter, J.N. Andersen, M. Scheffler, Surf. Sci. **541** 101 (2003).
- [102] A. Michaelides, M.-L. Bocquet, P. Sautet, A. Alavi and D. A. King, Chem. Phys. Lett. **367**, 344 (2003).
- [103] M. Todorova, W.X. Li, M.V. Ganduglia-Pirovano, C. Stampfl, K. Reuter, and M. Scheffler, Phys. Rev. Lett. **89**, 096103 (2002).
- [104] M.V. Ganduglia-Pirovano, K. Reuter, and M. Scheffler, Phys. Rev. B **65**, 245426 (2002).
- [105] C. Stampfl, S. Schwegmann, H. Over, M. Scheffler, and G. Ertl, Phys. Rev. Lett. **77** 3371 (1996).
- [106] K.D. Gibson, M. Viste, E.C. Sanchez, and S. J. Sibener, J. Chem. Phys. **110**, 2757 (1999).
- [107] J. Wider, T. Greber, E. Wetli, T.J. Kreuzt, P. Schwaller, and J. Osterwalder, Surf. Sci. **417**, 301 (1998).
- [108] A. Böttcher and H. Niehus, J. Chem. Phys. **110**, 3186 (1999).
- [109] M.V. Ganduglia-Pirovano, private communication.
- [110] W.X. Li, C. Stampfl, and M. Scheffler, Phys. Rev. Lett. **90**, 256102 (2003).
- [111] D. Kolthoff, D. Jürgens, C. Schwennicke, and H. Pfnür, Surf. Sci. **365**, 374 (1996).
- [112] N. Mårtensson and A. Nilsson, *High Resolution Core-Level Photoelectron Spectroscopy of Surfaces and Adsorbates*, Vol. 35 of *Springer Series in Surface Science* (Springer, Berlin, 1994), p. 65.
- [113] D. Spanjaard, C. Guillot, M.C. Desjonqueres, G. Treglia, and J. Lecante, Surf. Sci. Rep. **5**, 1 (1985); W.F. Egelhoff, *ibid.* **6** 253 (1987).

- [114] J.N. Andersen, D. Hennig, E. Lundgren, M. Methfessel, R. Nyholm, and M. Scheffler, Phys. Rev. B **50**, 17525 (1994).
- [115] M. Aldén, H.L. Skriver, and B. Johansson, Phys. Rev. Lett. **71**, 2449 (1993).
- [116] M. Aldén, H.L. Abrikosov, and B. Johansson, N.M. Rosengaard, and H.L. Skriver, Phys. Rev. B **50**, 5131 (1994).
- [117] S. Lizzit, A. Baraldi, A. Groso, K. Reuter, M.V. Ganduglia-Pirovano, C. Stampfl, M. Scheffler, M. Stichler, C. Keller, W. Wurth and D. Menzel, Phys. Rev. B **63**, 205419 (2001).
- [118] M.V. Ganduglia-Pirovano, M. Scheffler, A. Baraldi, S. Lizzit, G. Comelli, G. Paolucci, and R. Rosei, Phys. Rev. B **63**, 205415 (2001).
- [119] G. Binning, H. Rohrer, Ch. Gerber, and E. Weibel, Appl. Phys. Lett. **40**, 178 (1982); G. Binning, H. Rohrer, Ch. Gerber, and E. Weibel, Phys. Rev. Lett. **49**, 57 (1982).
- [120] J. Tersoff and D.R. Hamann, Phys. Rev. B **31**, 805 (1985).
- [121] D. Rogers, R. Shannon, and J. Gillson, J. Solid State Commun. **134**, 314 (1971).
- [122] J. Bardeen, Phys. Rev. Lett. **6**, 57 (1961).
- [123] C.J. Chen, *Introduction to Scanning Tunneling Microscopy*, Oxford series in optical and imaging science, Oxford University Press, New York (1993).
- [124] W.A. Hofer, A.S. Foster, and A.L. Shluger, Rev. Mod. Phys. **75**, 1287 (2003).
- [125] B. Johansson and N. Mårtensson, Phys. Rev. B **21**, 4427 (1980).
- [126] J.P. Perdew and M. Levy, Phys. Rev. B **56**, 16 (1997).
- [127] J. McBride, K. Haas, and W. Weber, Phys. Rev. B **44**, 5016 (1991).
- [128] Y.D. Kim, A.P. Seitsonen, and H. Over, J. Phys. Chem. B **105**, 2205 (2001).
- [129] B.L.M. Hendriksen and J.W.M. Frenken, Phys. Rev. Lett. **89**, 046101 (2002).
- [130] C. Stampfl, M.V. Ganduglia-Pirovano, K. Reuter, and M. Scheffler, Surf. Sci. **500**, 368 (2002).
- [131] K. Reuter and M. Scheffler, Phys. Rev. Lett. **90**, 046103 (2003).

- [132] *CRC Handbook of Chemistry and Physics*, CRC press (Boca Raton, FL, 1995).
- [133] E. Lundgren, J. Gustafson, A. Mikkelsen, J.N. Andersen, A. Stierle, H. Dosch, M. Todorova, J. Rogal, K. Reuter, and M. Scheffler, *Phys. Rev. Lett.* **92**, 046101 (2004).
- [134] W.X. Li, C. Stampfl, and M. Scheffler, *Phys. Rev. B* **68**, 165412 (2003).
- [135] K. Reuter and M. Scheffler, *Appl. Phys. A* **78**, 793 (2004).
- [136] J. Szanyi, W.K. Kuhn, and D.W. Goodman, *J. Vac. Sci. Techn. A* **11(4)**, 1969 (1993).

# Acknowledgments

I would like to thank

Matthias Scheffler for giving me the opportunity to do this work at the Fritz-Haber Institut and for his continuous support.

Kasten Reuter, for always taking the time to answer questions or sort out problems. You are the best supervisor one could have wished for. Besides, I really enjoyed the last few years. I can think of so many things to say that my list would grow out of proportion.

Jörg Behler and Jutta Rogal, for all the laughter we shared and the great time we had (and still have). I am so very grateful, that we share this time in Berlin.

Edvin Lundgren for the nice experiments.

Evgeni Penev, Veronica Pirovano, Caroline Morgan, Sladjana and all other present and former members of the group, who have helped me or made my time at the Fritz-Haber so pleasant.

Uma, for being a friend and the fun I had answering the unexpected questions I was sometimes faced with.

Walter, für all die Kino und Eis Nachmittage. Meiner Familie, dafür dass sie immer so eng zusammenhält.

Meinen Eltern und meiner Schwester für Ihre andauernde Unterstützung und einfach dafür, dass sie da sind. Diese Arbeit ist für euch.